Journal of Applied Research on Science and Technology

INSTITUTE OF RESEARCH AND DEVELOPMENT
RAJAMANGALA UNIVERSITY OF TECHNOLOGY THANYABURI

ISSN Online 2773-9473

Volume 24 Issue 1
January - April 2025

JARST RMUTT

Journal of Applied Research on Science and Technology (JARST)
E-ISSN : 2773-9473
Vol. 24 No. 1 January - April

The Journal of Applied Research on Science and Technology (JARST) aims to disseminate and share knowledge and ideas in the form of high-quality articles to academia, professionals, industrialists, and an important forum for exchanging knowledge between researchers, academics, faculty members and students both national and international, which will bring benefits in building academic cooperation and network that will lead to sustainable use of research. The articles that will be published in this journal must not be ever presented and published or in the evaluation processes in any other journals. Any piracy occurred will be only under the responsibility of the authors. The journal will not be responsible for such consequences.

Aims and Scope

The scope of the journal includes the following areas of research: General Engineering, General Materials Science, General Agricultural and Biological Sciences, General Computer Science, and General Mathematics with particular emphasis on issues that deepen in the basic and applied research. The JARST includes full length original, novel research articles and review articles. Accepted articles are immediately available online and are freely accessible without any restrictions or any other obligations to researchers and scholarly people globally.

Review Process

1. Evaluation by the Editor-in-Chief

The Editor-in-Chief will see whether the topic and theme of the article are appropriate and congruent with the stipulated objectives and format of the Journal. Plagiarism and benefits relating to theory and business contribution will also be investigated. The submitted paper may be returned to the author for preliminary revising or, if the aforesaid criteria are not met, rejected.

2. Evaluation by Review

All submitted manuscripts must be reviewed by at least two expert reviewers in the related fields. Reviewers will evaluate the quality of submitted article for publication via the double-blinded review system.

3. Evaluates the Reviews

The Editor-in-Chief make decision for article publication based on the external readers' evaluation. The said decision is either accepting the article for publication, rejecting it, or resending it back to the author for further elaborating revision.

Period of Issued Journal

The Journal of Applied Research on Science and Technology (JARST) will be 3 issues/year, as follows:

1st issue: January - April
2nd issue: May - August
3rd issue: September - December

Advisory Board

Contact

Institute of Research and Development, Rajamangala University of Technology Thanyaburi (RMUTT)
39 Moo 1, Klong 6, Khlong Luang Pathum Thani 12110 Thailand
Website: https://ph01.tci-thaijo.org/index.php/rmutt-journal/index
Phone: +66 2 5494492, +66 2 5494681
Fax: +66 2 5494680
Email: jarst@rmutt.ac.th

Editorial Note

The Journal of Applied Research on Science and Technology (JARST) is an academic journal prepared by Institute of Research and Development, Rajamangala University of Technology Thanyaburi (RMUTT). The JARST aims to disseminate and share knowledge and ideas in the form of high-quality articles related General Engineering, General Materials Science, General Agricultural and Biological Sciences, General Computer Science, and General Mathematics to researchers, academics, faculty members and students both national and international.

This journal published nine research articles. Each of the research articles presented interesting concepts such as Effectiveness of separated ICR for a wheeled skid-steering robot, Design of a two-seater seaplane wing spar structure with composite materials, Age-dependent mathematical models of ligaments and tendons, Effects of drilling parameters on drill bit wear of ASTM A36 steel, Investigation of propeller configuration effects on the flight stability of unmanned aerial vehicles, Increasing the value of jackfruit cobs as agricultural waste materials for syrup production by enzymatic hydrolysis using pectinase and cellulose, Exploring the design and construction techniques of post-tensioned slabs, Behavioral analysis of two-dimensional difference equations in the third quadrant and Development and optimization of a fresh lotus embryo piercing machine. Therefore, this journal is a channel disseminating the knowledge areas of physical sciences and life sciences which related persons could apply it for further benefits.

Lastly, the editorial team would like to considerably thank you for supporting and pushing forward this journal to occur and well accomplish. We are hopeful of your good cooperation and continuing support in the future.

Editorial Team

Contents

Received: August 14, 2024 | Revised: November 1, 2024 | Accepted: November 4, 2024

JOURNAL OF APPLIED RESEARCH ON SCIENCE AND TECHNOLOGY
JARST
INSTITUTE OF RESEARCH AND DEVELOPMENT
RAJAMANGALA UNIVERSITY OF TECHNOLOGY THANYABURI
ISSN ONLINE: 2773-9473
https://ph01.tci-thaijo.org/index.php/rmutt-journal

Effectiveness of separated ICR for a wheeled skid-steering robot

Ditsakorn Wanichratanagul, Witaya Wannasuphoprasit and Viboon Sangveraphunsiri*

Department of Mechanical Engineering, Faculty of Engineering, Chulalongkorn University, Bangkok 10330, THAILAND
*Corresponding author: viboon.s@chula.ac.th

ABSTRACT

The skid-steering robot has gained popularity due to its mechanical simplicity and robustness, making it a preferred choice in various applications. However, this configuration is prone to slip during turning maneuvers, resulting in inaccurate trajectory prediction using the conventional differential drive kinematic model. The separated instantaneous centers of rotation (ICRs) approach has been proposed to address this issue and mitigate slips experienced during turns. Compared to the computer simulations, this study investigates the trends of the separated ICR approach on the trajectory error using a real-world robot across different terrains in low dynamic conditions. The findings reveal that the effectiveness of the separated ICR approach in compensating for slip varies depending on the turning radius. Specifically, the approach is less effective with smaller turning radii and vice versa. Surprisingly, the terrain type does not significantly impact the effectiveness of the separated ICRs approach, suggesting that its performance is more closely linked to the turning radius than to the terrain conditions. Although the simulation method outlined in this research struggles with precise surface roughness estimation, it demonstrates consistent skid behavior, indicating the potential utility of separated ICRs for skid-steering robots. To enhance the accuracy of computer simulations, a deeper exploration of terrain surface conditions is necessary. Nonetheless, the implementation of separated ICRs on our four-wheel mobile robot shows promising results, underscoring the viability of using separated ICRs to improve the performance of skid-steering robots in various settings.

Keywords: Ground vehicles, Four-wheel mobile robot, Kinematics, Skid-steering, Instantaneous center of rotation

INTRODUCTION

Skid-steering robots have become increasingly popular in outdoor environments due to their mechanical simplicity and robustness, allowing more space within the robot [1, 2]. This type of robot has various applications especially in uneven terrain or dangerous missions, for example, mining robots [3], agricultural robots [4, 5], Planetary exploration robots [6], surveillance robots [7], and security robots [8]. The main focus of this project is to develop an autonomous outdoor mobile robot for transporting objects between buildings on a university campus.

The maneuvering configuration is based on the relative velocity of the left and right-side drive, similar to the unicycle differential-drive configuration. However, slip is inevitable during the turning maneuver due to the configuration involving multiple wheels or a track on both sides [9]. The slip violates the differential drive's no-slip and pure rolling assumption and is the primary challenge of the skid-steering configuration [10, 11].

Kinematic models based on differential drive configuration have been proposed to deal with slip. Among those, the most popular approach is the separated instantaneous center of rotation (ICR), which focuses on the ICRs of each side of the wheels instead of the configuration ICR. The separated ICR uses the length between the ICR of each side, which is obtained from the experiment, instead of the wheel-to-wheel width in the differential drive kinematic model. The previous works experiment with this approach using a thread robot [12] and a 4-wheel skid-steering robot [13], which gives better dead reckoning results than the differential drive kinematic model.

In contrast to the configuration ICR that varies considerably depending on the configuration and ground contact dynamics, the separated ICR remains within bounded regions of each side of the robot at low speed on hard terrain as the inertia force is the main contributor [14, 15]. Thus, the approximately constant position of the wheel ICRs can be assumed for each configuration.

This research aims to discover the trends of the separated ICR approach in terms of trajectory error compared to the typical differential drive kinematic model on a robot with real-time position tracking. The study tests the robot over 4 different terrains and 2 different turning radii, which are the actual applications of this project robot.

DOI: 10.60101/jarst.2024.257672

JOURNAL OF APPLIED RESEARCH ON SCIENCE AND TECHNOLOGY

MATERIALS AND METHODS

The setup of skid-steering in this research is depicted in Figure 1, which consists of two pairs of non-steering wheels at the front and rear of the robot. The linear and angular velocities of the robot (v,ω) is dictated by the velocities of the left and the right-side wheels (v_l, v_r). Each side's front and rear wheels must rotate at the same speed. To investigate the violation of the pure rolling and no-slip assumption, each wheel is defined by four constant parameters as α,β,l,r along with an angular variable $\varphi(t)$, as illustrated in Figure 2. Each wheel's longitudinal and lateral velocity can be expressed in Eq. (1) and (2).

$$\left[-\sin(\alpha+\beta)\ \cos(\alpha+\beta)\ l\cos\beta\right]R(\theta)v + r\dot{\varphi} = 0 \quad (1)$$

$$\left[\cos(\alpha+\beta)\ \sin(\alpha+\beta)\ l\sin\beta\right]R(\theta)v = 0 \quad (2)$$

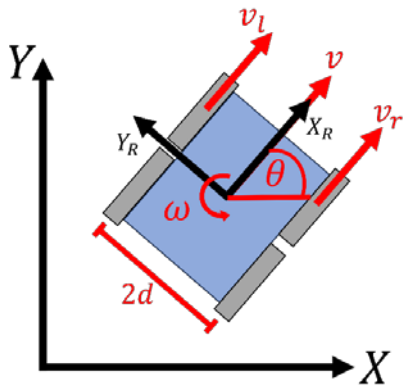

Figure 1 skid steering configuration with two pairs of non-steering wheels at the front and rear of the robot.

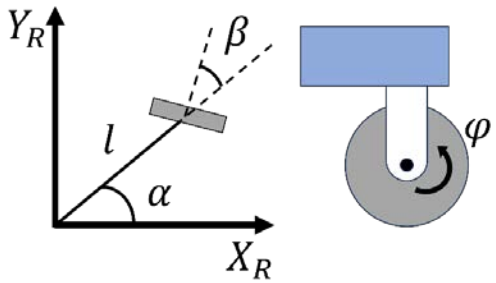

Figure 2 non-steering wheel configuration.

Where $R(\theta)$ represents the configuration rotation matrix, and v represents the configuration velocity vector. The lateral velocity is investigated further since it has to remain zero during the turning maneuver to satisfy the no-slip and pure rolling assumption. The lateral velocity of every wheel in this research configuration is defined in Eq. (3).

$$C_R R(\theta)v = 0 \quad (3)$$

While C_R is a 4x3 matrix containing the wheel configuration term of every wheel. Obviously, for skid configuration, rank $C_R = 2$ due to its two rotation axles parallel to each other. This serves as proof that the skid configuration could not steer without violating the no-slip and pure rolling assumption[9].

Unlike the skid configuration, the differential drive, which has a similar configuration, is steerable without violating any of those assumptions. The inverse kinematics of the differential drive can be expressed as follows[16]:

$$\begin{bmatrix} v_l \\ v_r \end{bmatrix} = \begin{bmatrix} 1 & -d \\ 1 & d \end{bmatrix} \begin{bmatrix} v \\ \omega \end{bmatrix} \quad (4)$$

where d represents the distance from the center line to each side of the mobile robot wheels. However, unlike the differential drive, which does not generate slip, Eq. (4) fails to accurately predict the motion of the skid configuration during turning maneuvers. Separate ICRs are employed to minimize motion errors. By treating each side of the wheels as rigid bodies, there are three ICRs within the configurations:

$ICR_C = (x_c, y_c)$ for overall configuration ICR, $ICR_L = (x_l, y_l)$ for left-side wheels ICR and $ICR_R = (x_r, y_r)$ for right-side wheels ICR as shown in Figure 3 [12, 13].

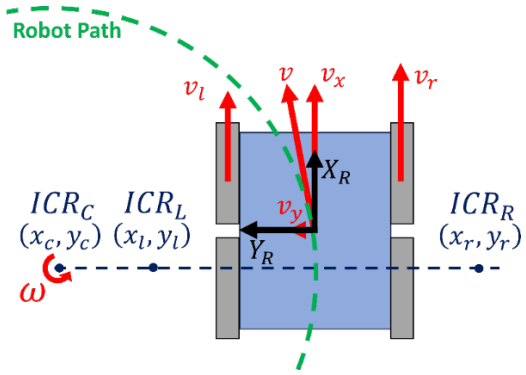

Figure 3 Separated ICRs of both sides of the configuration and ICR of the whole configuration when the configuration turns along the path.

Considering that both sides of the configuration rotate around their respective ICR, the location of each ICR can be shown as follows:

$$y_c = -\frac{v_x}{\omega} \quad (5)$$

$$y_l = \frac{v_l - v_x}{\omega} \quad (6)$$

$$y_r = \frac{v_r - v_x}{\omega} \quad (7)$$

$$x_c = x_l = x_r = \frac{v_y}{\omega} \quad (8)$$

Assume that the configuration is symmetrical, and its center of gravity is placed at the center of the

DOI: 10.60101/jarst.2024.257672

JOURNAL OF APPLIED RESEARCH ON SCIENCE AND TECHNOLOGY

configuration, the longitudinal velocity of the configuration becomes zero:

$$x_c = x_l = x_r = 0 \tag{9}$$

Assume that the mass of the configuration is well distributed over its body, the displacement between the ICR of each side and the configuration in the y-axis should be the same:

$$y_l = -y_r = y_o \tag{10}$$

Where y_0 is the displacement between the wheel ICR of both sides to the center of the configuration in the y-axis. The inverse kinematic model of the skid steering configuration can be expressed as follows:

$$\begin{bmatrix} v_l \\ v_r \end{bmatrix} = \begin{bmatrix} 1 & -y_0 \\ 1 & y_0 \end{bmatrix} \begin{bmatrix} v \\ \omega \end{bmatrix} \tag{11}$$

The value of y_0 can be determined by measuring the steering efficiency of the configuration through experimentation. By performing the zero-radius turning and comparing the actual angle and the angle, the configuration should be based on wheel rotation; the value of y_0 can be shown as follows.

$$y_0 = \frac{\int v_r dt - \int v_l dt}{2\theta} \tag{12}$$

Also, in low speed, y_0 is significantly dependent on the robot configuration parameters. External variables such as terrain type exert negligible influence on its values [14].

Skid steering robot

Figure 4 depicts the skid steering robot employed in this research, which operates as a four-wheel drive system. Its dimensions (W×L×H) are $0.71 \times 0.78 \times 0.54\,m$ and weight approximately $48\,kg$. The robot is powered by electricity stored in onboard batteries, the robot's locomotion is facilitated by four brushless servo motors, each fitted with encoders attached to its respective wheel. The distance between the center of the left and the right-side wheels d is $0.57\,m$. Suspension modules are incorporated at each wheel to mitigate force transmission from the ground to the robot body. This feature enables the robot to navigate uneven terrain smoothly, as illustrated in Figure 5. Additionally, to prove that the robot could overcome the friction generated by the nature of the skid-steering, the robot can perform a 180-degree turn utilizing a kinematic model derived from Eq. (4), using remote control, as demonstrated in Figure 6. The robot has a ZED2 stereo camera with a built-in V-SLAM algorithm (Visual Simultaneous Localization and Mapping). The camera observes the position of the environment feature point based on the parallax distance between each lens. The zalgorithm uses this information with IMU to map the environment and localize the camera to the map simultaneously to record the camera's trajectory. Eq. (4) and (11) are incorporated into the robot's control algorithm to conduct the experimental study.

Figure 4 Skid steering robot in this project.

Figure 5 Snapshot of robot moving on uneven terrain.

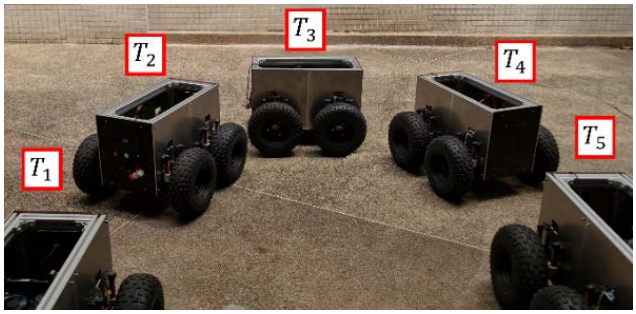

Figure 6 Snapshot of robot performs 180-degree turn indicates that the robot can overcome friction and perform skid-steering behavior.

Experiment methodology

The experiment takes place on four different terrains based on the campus, which are this project's main operation areas: a grass field, a ceramic plate floor, a concrete road, and a gravel passageway, as illustrated in Figure 7. The experiment was conducted in each terrain by letting the skid-steering robot perform 180-degree U-turns with 2 different radii, 1 and 2 meters. On each terrain and each radius, experimented using 2 different control algorithms, Eq. (4) and Eq. (11). The robot has to maintain linear velocity $1\,m/s$ during the experiment. The trajectory of each experiment is collected by a ZED2i stereo camera using its built-in V-SLAM algorithm. Due to the insensitivity over the terrain of the y_0, the experiment to determine y_0 is conducted over a gravel passageway and will use the

DOI: 10.60101/jarst.2024.257672

value on all the 180-degree turning experiments and simulations. Note that the ZED2i stereo camera is factory-calibrated and used as is.

Dynamic simulation

This study uses MATLAB's SimScape to simulate the skid steering trajectory. The SimScape model is shown in Figure 8. The model is constructed from robot configurations mentioned above to simulate joint-to-joint simulation as shown in Figure 8 section 1. The model wheels receive velocity input from Figure 8 section 2 and calculate force interaction, including friction, which generates slip in case fiction is insufficient using the contract force library [17] in Figure 8 section 3. This model has conducted a 180-degree turn using experiment conditions beforehand to investigate the friction coefficient. By varying the friction coefficient, the trajectory results of each experiment do not show any significant difference. Hence, we choose the friction coefficient 0.9 to represent the simulation result in the next topic.

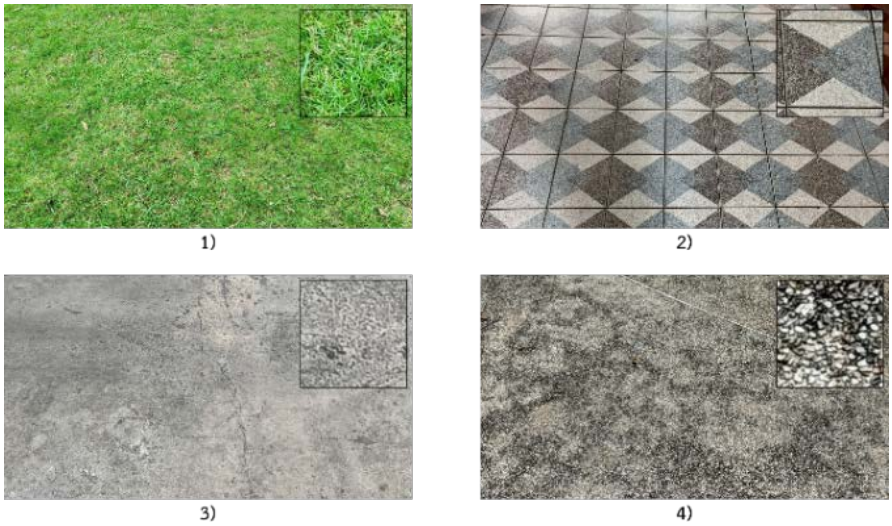

Figure 7 Urban terrain used in experiment 1) grass field 2) ceramic floor 3) concrete road 4) gravel passageway.

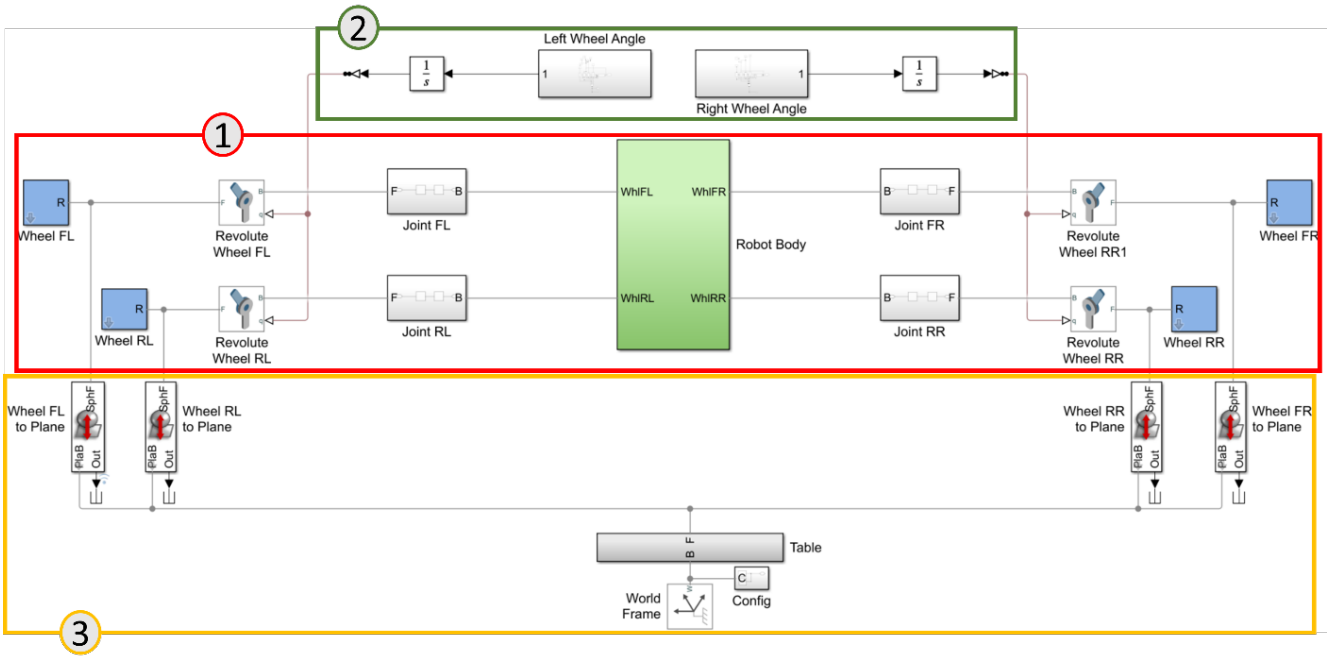

Figure 8 MATLAB's SimScape model for skid steering configuration moving on the floor with adjustable friction coefficient.

RESULTS AND DISCUSSION

By performing the zero-radius turning experiment on the gravel passageway, we obtain $y_o = 0.93\,m$ and use this value in the 180-degree turning experiments. The trajectory of the 180-degree turning experiment on four terrains at a radius of 1 and 2 meters is depicted in Figures 9 and 10, respectively. The continuous lines indicate the trajectory of the robot using Eq. (4) (using a constant d) as the robot algorithm, and the dashed lines indicate the trajectory of the robot using Eq. (11)

DOI: 10.60101/jarst.2024.257672

JOURNAL OF APPLIED RESEARCH ON SCIENCE AND TECHNOLOGY

(using a constant y_0) as the robot algorithm. The green line indicates the reference trajectory, the blue line denotes the simulation trajectory, and the other colors show the robot's trajectories on different terrains.

The trajectories of the robot using Eq. (11) converge to the reference trajectory more than the trajectories using Eq. (4) in both turning radii and the trajectories that use the same algorithm seem to converge with each other, which will be investigated further. All the experiment trajectories are shorter than the reference trajectory in which the 2 meters radius trajectories are closer to the reference than the other, which indicates that all the experiment trajectories are slip. However, the larger radius generates a smaller slip, and the Eq. (11) algorithm can reduce the trajectory error but cannot reduce the slip.

The simulation can simulate skid-steering behavior with Eq. (11) trajectories that converge more to the reference than the other in both turning radii, as found in the experiment trajectories. The simulation trajectories fail to simulate accurate slip, as evidenced by the longer distance between the simulation trajectories and the experiment. The friction model of the simulation is the main suspect of the inaccurate slip in the simulation as the model does not consider the wheel deformation.

To investigate furthermore about error comparison between both turning radii, the normalized error of each trajectory can be analyzed by calculating the distance between the experimental trajectory and the reference trajectory at the corresponding time, then normalizing it by dividing by the radius of the turning curve, as stated in Eq. (13). The errors of the trajectory depicted in Figure 9 and Figure 10 are presented in Figure 11 and Figure 12 respectively. Note that simulation results are excluded due to their accuracy.

$$error_t = \frac{\sqrt{\left(x_{ref,t} - x_{actual,t}\right)^2 + \left(y_{ref,t} - y_{actual,t}\right)^2}}{radius} \qquad (13)$$

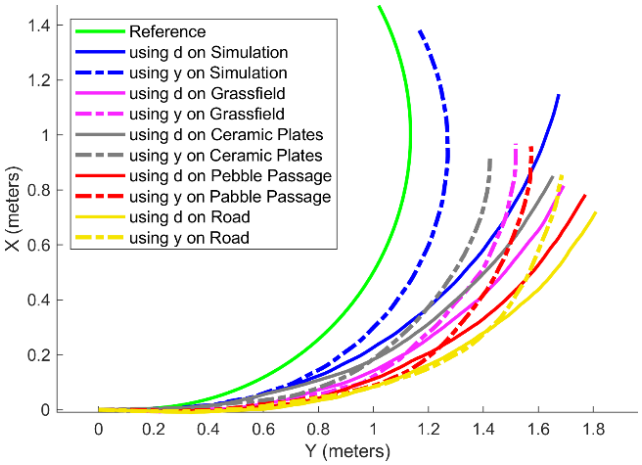

Figure 7 Trajectory results of the experiment on different terrain at a radius of 1 meter.

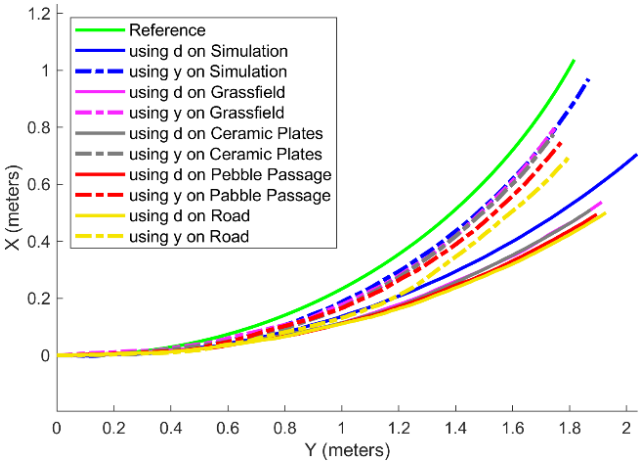

Figure 10 Trajectory results of the experiment on different terrain at a radius of 2 meters.

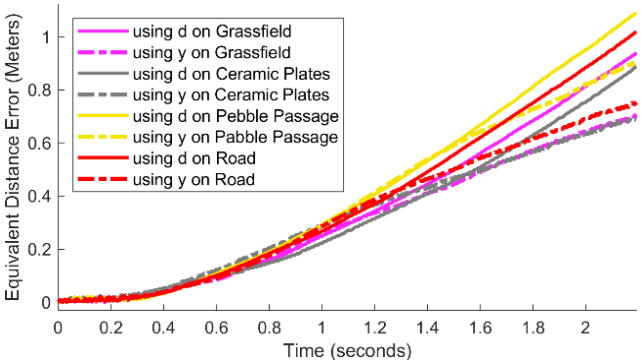

Figure 11 Equivalent trajectory error of the experiment on different terrain at a radius of 1 meter.

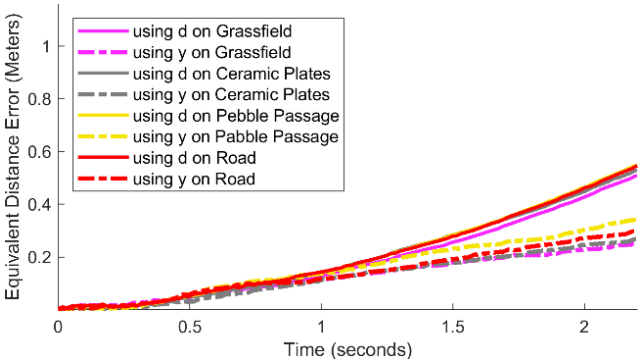

Figure 12 Equivalent trajectory error of the experiment on different terrain at a radius of 2 meters.

From Figures 11 and 12, the yellow dashed line in Figure 11 shows the trajectories using Eq. (11) have less error than the trajectories using Eq. (4) in both turning radii as the slopes are lower and the final errors are also more minor which indicates that the. The equivalent errors of the experiment with a larger radius are smaller than those with a smaller radius, which also supports that turning with a larger radius generates a smaller slip. In each turning radii, the trajectory errors of each algorithm are adhering together, which indicates that the terrain types are insignificant to slip behavior in this project setup as the parameter y_0 is mainly influenced by the robot configuration at low speed,

DOI: 10.60101/jarst.2024.257672

which can apply to the other robot in low dynamic operation.

The dashed lines and continuous lines between 0 - 0.8 second in Figure 11 and between 0 - 0.5 seconds in Figure 12 are aligned to indicate the angular acceleration period. The yellow dash line in Figure 11 has a more extended acceleration period. The gravel passageway is suspected to be the most friction terrain, which makes the robot more influenced by the dynamic conditions, and so is the y_0.

Compared to the robot size, the separated ICR approach significantly reduces trajectory error in low dynamic conditions such as large turning radius. The compensated control strategy, increasing the trajectory duration to match the reference, is recommended to reduce the trajectory error further. Also, a more accurate wheel-ground interaction model is recommended to simulate behavior precisely.

CONCLUSIONS

This study demonstrates the efficacy of the separated ICR approach on the actual condition that the robot in this research has to operate. Skid behavior trends have less impact when the robot turns at a larger radius. The trajectory error is also smaller when using a separate ICR approach, but the approach does not reduce the slip at each wheel. The experiment is done over 4 terrains with different friction coefficients and characteristics. The result shows that the terrain type is insignificant to the skid behavior in low dynamic. The simulation proposed in this research can replicate the skid behavior but fails to predict the trajectories accurately. The interaction between the wheel and the ground is the leading cause of the inaccuracy of the simulation. Despite the trajectory errors, the separated ICR approach is recommended to compensate for slip in low dynamic conditions. More sophisticated control strategies for trajectory timing adjustment and travel length compensation can also be considered in the future.

REFERENCES

1. Wang T, Wu Y, Liang J, Han C, Chen J, Zhao Q. Analysis and Experimental Kinematics of a Skid-Steering Wheeled Robot Based on a Laser Scanner Sensor. Sensors [Internet]. 2015;15(5):9681-702. Available from: https://doi.org/10.3390/s150509681.
2. Maclaurin B. Comparing the steering performances of skid- and Ackermann-steered vehicles. Proceedings of the Institution of Mechanical Engineers Part D Journal of Automobile Engineering. 2008;222:739-56.
3. Huh S, Lee U, Shim H, Park JB, Noh JH, editors. Development of an unmanned coal mining robot and a tele-operation system. 2011 11th International Conference on Control, Automation and Systems; 2011 Oct 26-29.
4. Fernandez B, Herrera PJ, Cerrada JA. A Simplified optimal path following controller for an agricultural skid-steering robot. IEEE Access. 2019;7:95932-40.
5. Cheein FAA, Carelli R. Agricultural robotics: Unmanned robotic service units in agricultural tasks. IEEE Industrial Electronics Magazine. 2013; 7(3):48-58.
6. Liu G, Liu Y, Zhang H, Gao X, Yuan J, Zheng W. The kapvik robotic mast: An innovative onboard robotic arm for planetary exploration rovers. IEEE Robotics & Automation Magazine. 2015;22(1): 34-44.
7. Zhang C, Zhan Q, Wang Q, Wu H, He T, An Y. Autonomous dam surveillance robot system based on multi-sensor fusion. Sensors [Internet]. 2020; 20(4):1097. Available from: https://doi.org/10.3390/s20041097.
8. Mandow A, Serón J, Pastor F, García-Cerezo A. Experimental Validation of a Robotic Stretcher for Casualty Evacuation in a Man-Made Disaster Exercise. In: 2020 IEEE International Symposium on Safety, Security, and Rescue Robotics (SSRR); 2020 Nov 4-6. Abu Dhabi, UAE. p. 241-5.
9. Campion G, Bastin G, Dandrea-Novel B. Structural properties and classification of kinematic and dynamic models of wheeled mobile robots. IEEE Transactions on Robotics and Automation. 1996; 12(1):47-62.
10. Yi J, Wang H, Zhang J, Song D, Jayasuriya S, Liu J. Kinematic modeling and analysis of skid-steered mobile robots with applications to low-cost inertial-measurement-unit-based motion estimation. IEEE Transactions on Robotics. 2009;25(5):1087-97.
11. Burke M. Path-following control of a velocity constrained tracked vehicle incorporating adaptive slip estimation. In: 2012 IEEE International Conference on Robotics and Automation; 2012 May 14-18. Minnesota, USA. p. 97-102.
12. Martínez J, Mandow A, Morales J, Pedraza S, Garcia A. Approximating kinematics for tracked mobile robots. The International Journal of Robotics Research. 2005;24:867-78.
13. Mandow A, Martinez JL, Morales J, Blanco JL, Garcia-Cerezo A, Gonzalez J. Experimental kinematics for wheeled skid-steer mobile robots. In: Proceedings of the 2007 IEEE/RSJ International Conference on Intelligent Robots and Systems. 2007 Oct 29 - Nov 2; San Diego, CA, USA. p. 1222-7.

DOI: 10.60101/jarst.2024.257672

JOURNAL OF APPLIED RESEARCH ON SCIENCE AND TECHNOLOGY

14. Góra K, Kujawinski M, Wroński D, Granosik G. Comparison of energy prediction algorithms for differential and skid-steer drive mobile robots on different ground surfaces. Energies. 2021;14(20): 6722.

15. Martínez JL, Morales J, García JM, García-Cerezo A. Analysis of tread ICRs for wheeled skid-steer vehicles on inclined terrain. IEEE Access. 2023; 11:547-55.

16. Eiammanussakul T. Design and Development of a Wall Climbing Robot with Magnetic Wheels: Chulalongkorn University; 2013.

17. Miller S. Simscape Multibody Contact Forces Library [Internet]. San Francisco: GitHub; 2014 [updated 2023 Dec 07; cited 2024 Jul 17]. Availability from: https://github.com/mathworks/Simscape-Multibody-Contact-Forces-Library.

DOI: 10.60101/jarst.2024.257672

Received: August 27, 2024 | Revised: November 2, 2024 | Accepted: November 5, 2024

JOURNAL OF APPLIED RESEARCH ON SCIENCE AND TECHNOLOGY
JARST
INSTITUTE OF RESEARCH AND DEVELOPMENT
RAJAMANGALA UNIVERSITY OF TECHNOLOGY THANYABURI
ISSN ONLINE: 2773-9473
https://ph01.tci-thaijo.org/index.php/rmutt-journal

Design of a two-seater seaplane wing spar structure with composite materials

Phacharaporn Bunyawanichakul, Monchai Suraratchai and Narongkorn Krajangsawasdi*

Department of Aerospace Engineering, Faculty of Engineering, Kasetsart University, Bangkok 10900, THAILAND
*Corresponding author: narongkorn.kra@live.ku.th

ABSTRACT

A two-seater, mono-wing seaplane was initially developed for survey and rescue operations, with an empty weight of 470 kg and a maximum takeoff weight of 650 kg. Fiber-reinforced composite materials, consisting of fiber reinforcement and thermosetting polymer, were used in this airframe to reduce weight because the structural properties can be customized by adjusting the orientation of the fiber fabric layup and removing redundant material, which is impossible with metal. This paper presents a comprehensive overview of the design process for the aircraft's primary I-beam wing spar, employing composite material. Before conducting design calculations, it is critical to consider the variability of characteristics of composite materials caused by fabrication conditions such as temperature, humidity, and defects. As a result, it is imperative to conduct thorough testing of carbon fiber-reinforced composites following many different testing requirements. The coupon tests capture critical characteristics such as strength, stiffness, and Poisson's ratio across several orientations. The wing spar I-beam structure was subsequently developed with three primary considerations: stiffness (maximum deflection), strength, and stability (structural buckling). Following preliminary sizing of the I-beam wing spar, a simple initial layup was recommended, with primary loading in each component. The initial design was then subjected to a more detailed calculation using classical lamination theory, which took into account distributed load along the wing, spar taper, ply-drops along the span, and composite layup guidelines in order to reduce structural weight while ensuring the main spar's ability to withstand operational loads effectively. The calculating results show that the spar with an optimized composite design has a lighter weight than the original design by around 43%, while it can withstand the same loads with no analytical failure.

Keywords: Aircraft structural design, Seaplane, Composite material, Classical lamination theory, Mechanical properties

INTRODUCTION

Polymer composites are crucial in the aerospace industry, primarily attributable to their reduced mass and exceptional mechanical characteristics. [1]. These materials are thoroughly integrated into structural frameworks such as wings, fuselage, and tail regions, where their exceptional strength-to-weight ratio greatly elevates structural integrity and total performance [2-7]. Furthermore, carbon fiber/epoxy composites have attained notable prominence in commercial aviation, signifying progressive advancements in composite materials since the mid-20th century. Weight reduction represents another critical application, as aircraft with diminished mass contribute to enhanced fuel efficiency and lower operational expenditures, which is essential for promoting sustainability within the aviation sector. In addition, the resistance of polymer composites to corrosion is quite impressive, helping to enhance the longevity of aircraft components while cutting down on maintenance expenditures [4, 8]. In flight-control mechanisms, polymer-based composites are employed in bearings, whose tribological characteristics are paramount across diverse operational scenarios. In summary, incorporating polymer composites within the aerospace sector improves performance metrics and contributes to sustainability objectives by curtailing carbon emissions through optimized design and manufacturing methodologies. Additionally, the evolution of fabrication processes, including additive techniques, is streamlining the production of sophisticated forms and personalized elements, boosting the effectiveness of polymer composites in aircraft design [9].

Generally, for aircraft wings, the main component that carries most of the load produced from the aerodynamics is the wing spar [10]. A two-seater, mono-wing seaplane with an empty weight of 470 kg and a maximum takeoff weight of 650 kg was designed with composite material to reduce the weight and ease of manufacturing. The wing is connected to a wing strut at a distance from the mid-plane of 2.588 m. The strut shares the load from the wing spar and reduces the tip deflection. Figure 1 (a)

DOI: 10.60101/jarst.2024.257706

JOURNAL OF APPLIED RESEARCH ON SCIENCE AND TECHNOLOGY

shows the half-wing planform, wing component (spar, rib, control surfaces), and the strut connecting position. The aircraft wing spar was designed as an I-beam, as the section shown in Figure 1(b).

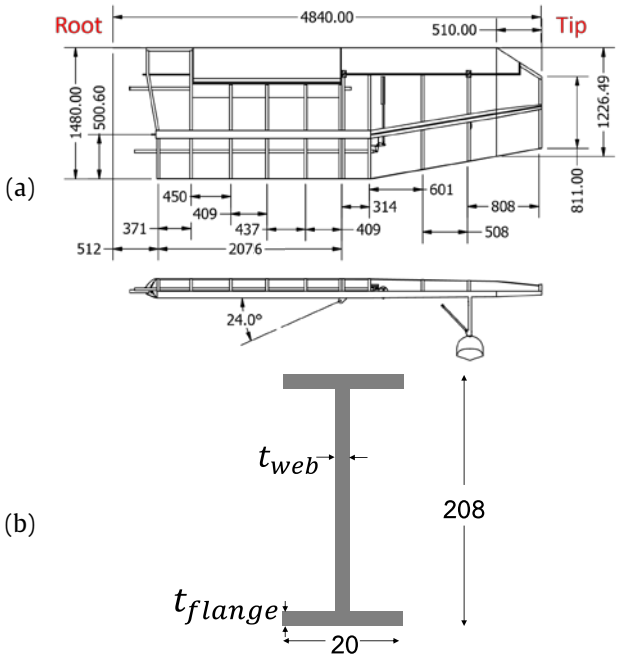

Figure 1 (a) Drawing of the wing (top and front view); (b) spar I-beam cross section at the root (all units in mm).

This work begins by reporting the mechanical properties of the materials utilized in this structure, particularly carbon fiber-epoxy (CF) and glass fiber-epoxy (GF), based on results obtained by material testing according to ASTM standards for composite material. The structural design of composite materials is then provided by an analytical method based on classical lamination theory, which considers three factors: stiffness, strength, and stability (plate buckling) [11]. This method applies the structural calculation of the isotropic material. However, it needs an additional consideration to the material orientation as the composite material is an orthotropic material that can design the ply orientation to counter such load in such direction.

The most appropriate design for the wing spar is finally proposed using the analytical calculation based on Classical lamination theory [11]. Its physical (weight and thickness) and structural safety under the maximum load are compared to the original design.

MATERIALS AND METHODS

Materials

Two materials were used in this study: carbon fiber-epoxy (CF) and glass fiber-epoxy (GF). Carbon fiber is Neotech EC3C60 - carbon 3k plain weave [12], Glass fiber is Fiberglass Cloth EW200 [13], and epoxy is Epotec YDL579 with TH8377M hardener [14]. CF and GF were fabricated with the hand layup method, laying the fiber fabric on a flat aluminum mold and applying epoxy resin ply-by-ply until reaching eight plies (an estimated thickness of 2.5 mm). The hand-laid composite was then covered with vacuum bag and applied with a vacuum pressure. It was left for curing at 44°C for 8 hours. The cured laminates were cut to the recommended size according to ASTM D3039 for tensile testing and ASTM D3518 for in-plane shear properties testing. There are five specimens per testing group. The cut specimens were measured for their width and thickness using a vernier caliper and micrometers, respectively, to report the cross-section size of the specimen for stress calculation. The specimens were tested with a universal testing machine attached to a bi-axial extensometer (Epsilon model 3560-BIA). The force and extension of the specimens were recorded and analyzed for the stiffness, strength, and Poisson's ratio of the materials. The average material properties of both materials are shown in Table 1.

Table 1 CF and GF mechanical properties.

Mechanical properties	CF	GF
Ply thickness (mm)	0.28	0.21
Density (g/cm^3)	1.37	1.61
Fiber volume ratio (%)	41	39.5
Tensile modulus, E_1=E_2 (GPa)	44.81	14.23
Tensile Strength, σ^*_{1T}=σ^*_{2T} (MPa)	467.46	329.78
In-plane shear modulus, G_{12} (GPa)	3.14	2.50
In-plane shear strength, τ_{12} (MPa)	65.71	66.87

Calculation sequence

The composite structure calculation is based on materials' mechanics, *e.g.,* axial, bending, shear stress, and buckling. However, it is slightly different from isotropic material, *i.e.,* aluminum or steel, as composite materials are anisotropic materials that generally have different properties in each direction. The composite wing spar structure is calculated following classical lamination theory, as shown in the diagram in Figure 2. The calculation sequences are:

- Load calculations: The calculation starts from the load calculation, which consists of loads from aerodynamic, structure weight, and attachment on the wing (strut in this case). The ultimate load is identified according to light sport aircraft standard ASTM F2245 [15].
- Initial plies calculation: The initial layup is computed by simplifying the problem to a single load case assuming the equivalent and separately estimating the material required for flange and web by neglecting any interaction between the two components.
- Construct layup: The initial plies requirement will be the initiation of building a laminate for the flange and web. The composite laminate guidance [16] will be considered in this lamination.

DOI: 10.60101/jarst.2024.257706

- Refine calculation: After the laminate with the layup guidelines is constructed, the detailed (refined) calculation, including tip deflection, stress on flange and web, and the buckling, will be calculated for the overall section at the highest load position. The reserve factor (RF) will then be calculated for any possible failure, stress using maximum stress criteria, stability using critical buckling load, and tip deflection limit.
- If the failure occurs in a ply (RF<1), the layup will redesigned by adding plies of materials to avoid a failure.
- If no failure occurs (RF>1): this refers to overdesign and a redundant weight. This leads to removing plies until the lowest RF value among all conditions is just above 1. This laminate will be called an "Optimized layup".

To make the analytical calculation possible, some details of the preliminary design spar were suppressed to simplify the analysis, and there are general assumptions made for the calculation following:

- Straight spar from the root to tip, no bent shape.
- A small off-center of the load from the centroid of the spar leads to negligible torsional load and twist angle.
- Separately calculate the components: top flange, bottom flange, and web, no bonding, curves, or bent joint to be considered.
- The thin wall assumption was applied to all calculations.
- A strut hinge is a point load acting in the strut fixture direction. It can cause some downward load for the deflection calculation.

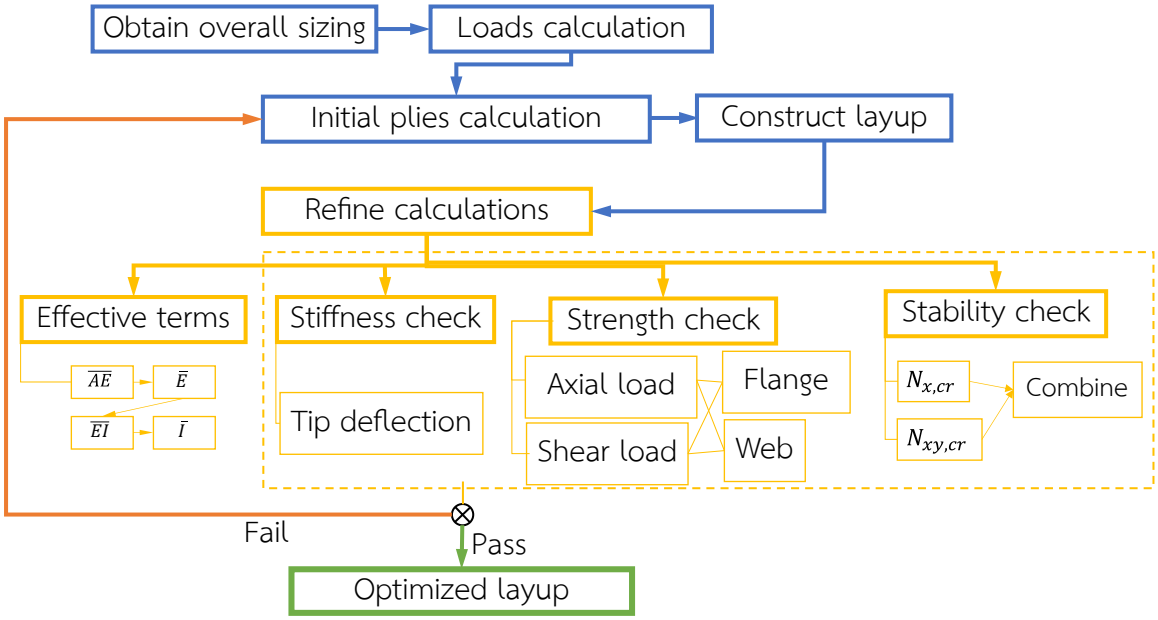

Figure 2 Calculation step for optimized composite laminate design.

Wing loading

The airload (aerodynamic load) along the spanwise was initially calculated according to trapezoid lift distribution [17]. The total lift equals the maximum takeoff weight of the aircraft (650 kg). The dead weight of the wing (50 kg) distributed along the spanwise corresponding to the chord of the section (Figure 1(a)) was deducted from the airload for the total distributed load. The equilibrium force equation calculated the reaction force at the strut hinge point. The distributed load and strut hinge force on the wing are shown in Figure 3(a).

The axial load, shear load, and bending moment diagram were then developed on the wing spar. The critical position of the diagram, located at the strut fixing point (X = 2.588 m), allowed for determining the maximum axial force, shear force, and bending moment. As shown in Figure 3(b), (c), and (d), the maximum axial load (F), shear force (V), and bending moment (M) are, respectively, 5350 N, 1231 N, and 1186 N-m. The ASTM F2245 [15] light sport aircraft load factor (n_{max}=+4) and the safety factor 1.5 at the maximum load were multiplied by the maximum loads from the diagrams.

Initial calculation

Every component (flange and web) had its original estimate of the necessary plies considered. A single-ply orientation-0° plies to counteract axial load on the flange and 45° plies to counteract shear loading in the web-was used to support the load. The basic diagram utilized in the initial computation, the axial stress and shear stress, is shown in Figure 4, where n_x denotes the number of piles in x direction and t_x is the thickness of each pile in the x direction.

DOI: 10.60101/jarst.2024.257706

JOURNAL OF APPLIED RESEARCH ON SCIENCE AND TECHNOLOGY

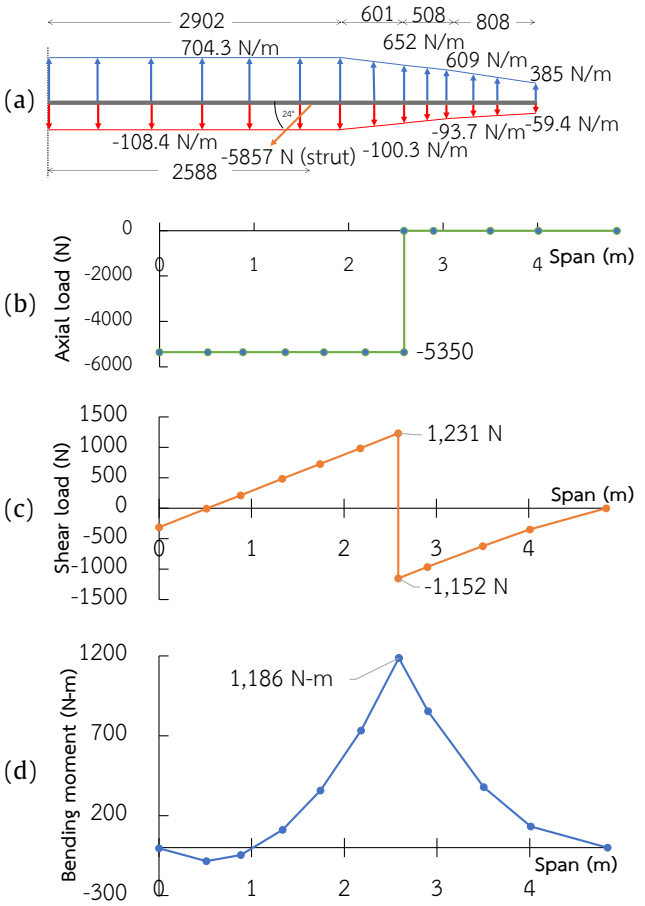

Figure 3 Diagram of (a) wing load distribution, (b) shear, (c) axial force (d) bending moment along the spanwise.

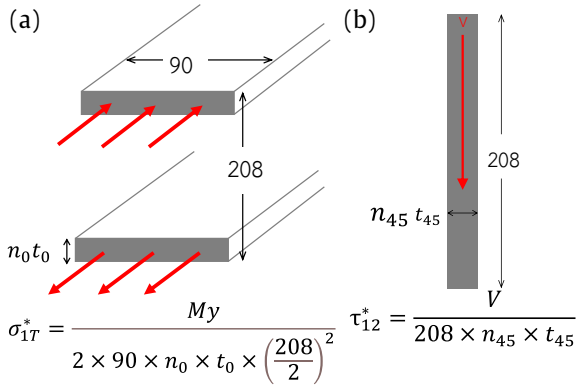

Figure 4 Initial calculation for (a) spar flange 0° plies thickness to counter axial load; (b) spar web 0° plies 45° plies thickness to counter shear load.

Design of the laminate

The laminate will be constructed based on the composite layup guidelines [16]:

- Keep the orientation simple: strict with 0°, 45°, and 90° for the ease of ply cutting.
- Every laminate should have a minimum of 10% of fibers in each direction [0°/±45°/90°] to counter the unpredicted loads.
- Avoid grouping more than 4 plies of the same orientation to minimize the delamination and protect the main load carrying 0° plies.
- The plies drop from the flange to the web needs to be reasonable and possible for manufacturing.

Refine check

There are three checks in the refined calculation: tip deflection (based on composite stiffness), strength, and stability (based on plate bucking). Three of them are based on effective section stiffnesses ($\overline{AE}, \overline{EI}$) and equivalent isotropic section properties ($\bar{E}, \bar{I}$), following equations (1)-(4). The laminate longitudinal stiffness (E_{x_i}) is calculated on each component (flanges and web) separately using ElamX software based on classical lamination theory [18]. A_i and I_i is the area and second moment of inertia of each component (flange and web).

Due to the classical lamination theory, it is restated that only symmetry and balanced laminates, with no extension-bending coupling, are eligible to be used with these computations. Unsymmetric laminate calculation results will be inaccurate but might provide a conceivable structural safety trend.

$$\overline{AE} = \sum (A_i E_{x_i}) \tag{1}$$

$$\bar{E} = \frac{\overline{AE}}{\sum (A_i)} \tag{2}$$

$$\overline{EI} = \sum (I_i E_{x_i}) \tag{3}$$

$$\bar{I} = \frac{\overline{EI}}{\bar{E}} \tag{4}$$

Stiffness refine-check

The tip deflection is usually computed using the superposition method of the point load gathered from the distributed load using beam theory. This is referred to as the beam's stiffness.

$$v = \sum \left(\frac{P_i l_i^3}{3\overline{EI}_i} + \frac{P_i l_i^2}{2\overline{EI}_i} (L - l_i) \right) \tag{5}$$

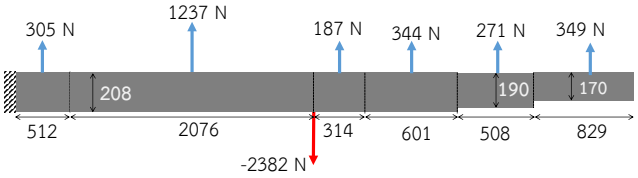

Figure 5 Load case and dimension for tip deflection calculation.

The effect of the spar web taper was simplified to the different section web heights (approximately 208, 190, and 170 mm). Figure 5 displays the theoretical dimension combined with the load case. Equation (5) can be used to calculate the tip deflection (v), which is the result of adding the end load's deflection and the

DOI: 10.60101/jarst.2024.257706

beam's angle after the loading position. P_i is the load at each position, l_i is the length from the root to the load position and L is the total spar length.

Strength check

The stress calculation in this section emphasizes the strut hinge point, X=2.588 m from the wing root, which is the location experiencing the highest load in this situation. Table 2 displays the maximum axial load (F), shear force (V), and bending moment (M) that were derived from Wing loading. In order to get the ultimate load case, these loads were multiplied by 4 and 1.5. The axial and shear stresses were estimated independently.

Table2 Maximum load at X = 2.588 m.

Axial, F (N)	Bending, M (N-mm)	Shear, V (N)
5350	1186 x 10^3	1230

Each component's maximum axial stress ($\sigma_{i,max}$) is calculated by superposing the axial (compression) stress, compression force (F), and the bending stress, bending moment (M), using equation (6), where y_i is the component's highest point of the spar to the centroid of the I-beam cross-section (104 mm). For thin wall shear flow, equation (7) was used to calculate the maximum shear stress ($\tau_{i,max}$). Then the laminate strength determined by applying the 10% rule was compared to the values of laminate strength, σ_T^* and τ_{xy}^*, found in equations (8) and (9).

60% of the tensile strength is a rule of thumb for compressive strength [19]. Since compressive strength is typically lower than tensile strength, the reserve factor (RF), which illustrates the degree of safety of the structure, was finally evaluated for axial (RF_A) and shear loads (RF_{Sh}) using equations (10) and (11). A structure is safe for the maximum load condition if its RF value is greater than 1.

$$\sigma_{i,max} = \left(\frac{My_i}{\bar{I}} + \frac{F}{\Sigma A}\right)\frac{E_{x_i}}{\bar{E}} \tag{6}$$

$$\tau_{i,max} = \frac{q_{max}}{t_i} = \frac{V}{t_i\bar{I}}\left(\int_0^{s_{max}} t_i y ds\right)\frac{E_{x_i}}{\bar{E}} \tag{7}$$

$$\sigma_T^* = \left(1 \times \frac{t_0}{t} + 0.55\frac{t_{45}}{t}\right)\sigma_{1T}^* \tag{8}$$

$$\tau_{xy}^* = \left(0.1 \times \frac{t_0}{t} + 0.55\frac{t_{45}}{t}\right)\frac{\sigma_{1T}^*}{2} \tag{9}$$

$$RF_A = \frac{0.6\sigma_T^*}{\sigma_{i,max}} \tag{10}$$

$$RF_{Sh} = \frac{\tau_{xy}^*}{\tau_{i,max}} \tag{11}$$

Stability check

The stability check compares the critical buckling stress on the laminate, which depends on its flexural stiffness. ElamX software was utilized to compute the critical buckling load intensity for axial ($N_{x,cr}$) and shear ($N_{xy,cr}$) of each laminate component, based on the ESDU chart [20].

The flange and web support were classified as shown in Figure 6. The flange was regarded as half breadth (45 mm) with three sides of simple support and one side free (no support) as it was an I-beam. The dimension of the plate shown in Figure 6 accounted for the critical load position, X = 2.075 to 2.389 m.

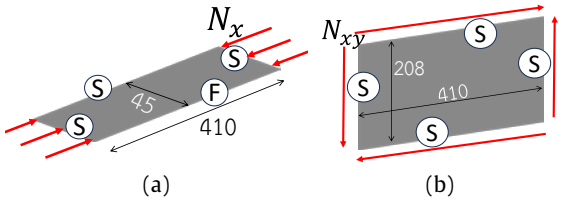

Figure 6 Calculated cases of the (a) buckling on flange; (b) buckling on web (unit in mm).

The stress determined from Section 0 for this section was compared to the critical buckling stress. Equations (12) and (13) were used to determine the RF of each component utilizing the combined loading case of the axial and shear on each component, flange, and web, where t_i is the thickness of the laminate.

$$FI_i = \left(\frac{\tau_{i,max}}{\frac{N_{xy,cr}}{t_i}}\right)^2 + \frac{\sigma_{i,max}}{\frac{N_{x,cr}}{t_i}} \tag{12}$$

$$RF_i = \frac{1}{\sqrt{FI_i}} \tag{13}$$

RESULTS AND DISCUSSION

Initial design

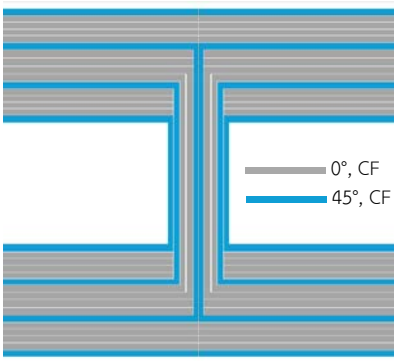

Figure 7 Optimized layup sequence diagram of the design I-beam.

According to the initial calculation in section 0, the initial 0° and 45° plies are 8 and 1 plies, respectively. These make the first layup to $[45, 0_4, \underline{45}]_s$ on the flange and $[45_2, 0_2, 45]_s$ on the web. However, the design results in a low critical buckling load due to the lack of 0° plies on the flanges ($N_{x,cr}$=208 N/mm), which can cause the buckling in the flange due to the axial load.

DOI: 10.60101/jarst.2024.257706

JOURNAL OF APPLIED RESEARCH ON SCIENCE AND TECHNOLOGY

The second design adds a block of four 0° plies to the flanges, which become $[45, 0_4, 45, 0_2]_s$.

As the layup diagram shown in Figure 7, this is referred to as the ply drop from the flange to the web and is considered an optimal design.

Refine calculation

The original design from a publication [21] was compared to the optimal design. It was made from para-beam (P, 4 mm thick) and CF. While the parameters of carbon fiber epoxy in this calculation were based on the available properties in Table 1, the mechanical properties of the para-beam are also obtained from [21]. The layup sequence of the original and optimal designs is shown in Table 3. The spar was designed to be manufactured as a layup of two C-shape beams, followed by an adhesive bonding of the two C-beams back-to-back in the assembly stage with some patching of layers to complete an I-beam with the mentioned laminate. The layup sequence of the two designs was then calculated for their weight by the summation of the spar area and the component thickness multiplied by the density of the composite material. The strength of the laminate was estimated by equations (8) and (9). The practical section stiffnesses and equivalent isotropic section properties were also computed and shown in Table 3. The refined calculation results with the RF for each case of the two designs are shown in Table 4.

Table 3 Refine calculation: layup sequence, dimension, and laminate parameters.

Design	Component	Layup	Thick (mm)	Weight (kg)	E_x (GPa)	Tensile strength (MPa)	Shear strength (MPa)	$\bar{E}$ (GPa)
Optimal (CF only)	Flange	$[45, 0_4, 45, 0_2]_s$	4.48	7.80	39.29	414.8	49.6	35.00
	Web	$[45_2, 0_2, 45]_s$	2.8		28.79	289.8	86.5	
Original (CF + Parabeam)	Top flange	$[0_{12}]_s$	6.72	13.84	45.06	467.5	23.4	28.36
	Web	$[(45,0)_6, \underline{P}]_s$	10.72		21.22	227.1	47.6	
	Btm. flange	$[0_6]_s$	3.36		45.06	467.5	23.4	

Table 4 Refine calculation: stiffness, strength and stability check result.

Design	Component	Stiffness	Stress				Stability		
		Tip Deflection (mm)	Axial stress (MPa)	Shear stress (MPa)	RF axial	RF shear	$N_{x,cr}$ (N/mm)	$N_{xy,cr}$ (N/mm)	$RF_{buckling}$ Combine load
Optimal (CF only)	Flange	213.02	112.27	2.91	2.22	17.08	449.15	858.29	1.09
	Web		50.38	15.44	5.72	5.60	101.40	62.70	1.41
Original (CF + Parabeam)	Top flange	153.74	72.39	2.59	3.87	9.01	562.78	1886.07	1.08
	Web		36.94	4.54	3.69	10.48	3320.22	5393.62	3.82
	Btm. flange		82.54	3.07	5.66	7.62	70.34	235.76	1.11

Comparative discussion

It can be seen that the weight of the optimal design is almost half of the original design, as seen in Table 3. According to the refined calculation check in Table 4, the optimal design has the RF value of flange buckling just above 1 (for both flange-1.09 and web-1.41), indicating the highly optimized design because one case is just at the boundary of the criteria. The original and optimal RF values are more significant than 1, meaning the spars are safe for the ultimate load case. Although both original and optimal designs can pass the refined check with the lowest RF values in similar ranges (1.09 for optimal and 1.08 for the original in the top flange buckling), the original design shows a high stiffness by resulting in a low tip deflection and high strength by showing higher RFs in all strength checks. However, the more robust structure is at the expense of the almost double weight of the spar, which can result in the structure load that can reduce the allowable payload of the aircraft. Moreover, some redundant layers, *e.g.,* 12 plies of 0° in the original web, resulting in a robust structure, *i.e.,* $RF_{buckling,\ web}$ up to 3.82, can be removed to reduce the overall structural weight.

Discussion

The calculation procedure in Figure 2 can provide a reasonable result as the total weight of the design spar is in the same magnitude as the available spar. This implies that the calculation sequence proposed here can be used to design a monolithic structure using composite material with the mentioned assumptions.

DOI: 10.60101/jarst.2024.257706

Although the current method cannot automatically optimize the structure weight, and the designer has to add or remove the ply to obtain the optimal design with the safety criteria, the sequence can be developed further for an automated optimization tool for composite structure design. The tool will not only be limited to the design of aircraft structures, but it can also expand to other lightweight composite structure fields such as automotive parts or civil structures.

According to the assumptions above, the proposed simplified calculation method has some limitations, *e.g.,* the negligible torsional load from the bent shape and off-axis load, which can cause the twisting angle and some additional shear load on the spar. This can change the aerodynamic shape and affect the aerodynamic design. However, the reserve factor for shear load is still high, meaning that the structure should be able to carry the additional shear load without any failure.

Another significant limitation of the calculation method is the assumption of independent component calculation. This was made to calculate the structural stress without any interaction. As a composite material in which the structure was fabricated during manufacturing, the spar structure may have some imperfect bonding, especially at the corners, which can build up a resin pocket or other manufacturing defects, *e.g.,* interlaminar bonding, ply drop or edge ply end, *etc.* These defects can diminish structural strength but cannot be included in the analytical calculation method. Hence, those defect effects were embedded in the safety factor (x1.5) provided before the initial load calculation. The actual spar test must be performed to verify the structural strength and ensure structural safety before entering the line production.

CONCLUSIONS

This article presents an analytical approach for the simplified I-beam wing spar design. It employs orthotropic materials-such as composites-whose computations differ slightly from those of isotropic materials. In order to give the structure the ability to support a particular load in specific directions, it is necessary to consider the ply orientation. It needs consideration of the ply orientation which can assign a specific ply orientation to the structure to carry a specific load in such a direction. Some of the key findings can be concluded as below:

- The calculation for this study was constructed following the classical lamination theory using the mentioned sequence. This can be a guideline for any composite structure design.
- Once the first layup design met the requirements, a layup design aligned with the guidelines was established. The layup was then calculated to determine the ability to withstand the loads and maintain the safety and performance limit. The laminate was then optimized to the minimal requirement of the structure.
- It was found from the calculation sequence that the optimal layup obtained from the calculation sequence is $[45, 0_4, 45, 0_2]_s$ on the flange and $[45_2, 0_2, \underline{45}]_s$ on the web.
- Compared with the original design, this layup is lighter, about 43%, and it complies with basic safety requirements for the mentioned load circumstances. Note that the weight shown in the calculation is only the composite material weight based on the density of composite materials; the actual weight should be slightly more than these figures due to the bonding joint and manufacturing imperfections.

It should be considered that there are some limitations of the suggested method, such as the assumptions of the spar taking a whole load of the aircraft, a perfect bonding of the materials, and a negligible bending spar structure, which could lead to a twisting load. Hence, there should be some potential future work to complete the work as suggested below:

- The twisting of the spar should be included in the detailed torsional load calculation.
- A more detailed calculation should consider the joints of the component, and other components on the wing, including wing ribs and skin, should be included in future calculations.
- Full structural analysis using the finite element method through software should be conducted with a validation of the presented result. This can confirm the overall design of the aircraft.
- Finally, the designed spar and actual full wing, a combination of wing components, must be tested according to the load limit stated in ASTM F2245.

ACKNOWLEDGEMENT

The authors would like to thank Panus Aviation Services Co., Ltd. for assisting with the specimen preparation and providing the aircraft design information.

REFERENCES

1. Awad ZK, Aravinthan T, Zhuge Y, Gonzalez F. A review of optimization techniques used in the design of fibre composite structures for civil engineering applications. Mater Design. 2012;33:534-44.
2. Khames M, Embaby A, Agha A. Comparison between the Use of Aluminum and Composites in the Design of a Wing-Spar of an Airplane. MSF [Internet]. 2019; 953:95-100. Availability from: https://doi.org/10.4028/www.scientific.net/msf.953.95.
3. Kennedy G, Martins JR, editors. A comparison of metallic and composite aircraft wings using

DOI: 10.60101/jarst.2024.257706

aerostructural design optimization. 12th AIAA Aviation Technology, Integration, and Operations (ATIO) Conference and 14th AIAA/ISSMO Multidisciplinary Analysis and Optimization Conference; 2012.

4. Beukers A, Bersee H, Koussios S. Future aircraft structures: From metal to composite structures. In: Nicolais L, Meo M, Milella E, editor. Composite Materials. London: Springer; 2011. p. 1-50.
5. Kesarwani S. Polymer composites in aviation sector. Int J Eng Res. 2017;6(10):518-25.
6. Williams TS. Multifunctional polymers and composites for aerospace applications [Internet]. National Aeronautics and Space Administration; 2019 [cited 2024 Jun 15]. Availability from: https://ntrs.nasa.gov/api/citations/20190026444/downloads/20190026444.pdf
7. Naidu CG, Ramana CV, Rao YS, Rao KVP, Vasudha D, Anusha G, et al. A Concise Review on Carbon Fiber-Reinforced Polymer (CFRP) and Their Mechanical Significance Including Industrial Applications. In: Rahman MM, Asiri AM, Chowdhury MA, editor. Carbon Nanotubes-Recent Advances, New Perspectives and Potential Applications. 2023.
8. Rathod VT, Kumar JS, Jain A. Polymer and ceramic nanocomposites for aerospace applications. Applied Nanoscience. 2017;7:519-48.
9. McIlhagger A, Archer E. Polymer Composites in the Aerospace Industry. 3 Manufacturing processes for composite materials and components for aerospace applications. Woodhead Publishing; 2014. p. 53.
10. Fleuret C, Andreani AS, Lainé É, Grandidier JC, L'héritier S, Gorge AL. Complex wing spar design in carbon fiber reinforced composite for a light aerobatic aircraft. Mech Ind. 2016;17(6):614.
11. Daniel IM, Ishai O, Daniel IM, Daniel I. Engineering mechanics of composite materials. New York: Oxford university press; 1994.
12. Neotech Composites. Carbon plain [Internet]. 2023 [cited 2024 Apr 24]. Availability from: https://neo.co.th/en/products/item/Carbon-plain/carbon-plain.
13. RIGHT Composite. Fiberglass Cloth EW200 [Internet]. 2023 [cited 2024 Apr 24]. Availability from: https://www.rightcomposite.com/EW200-fiberglass-cloth.com.
14. Aditya Birla Chemicals. Epotec Epoxy Systems [Internet]. 2024 [cited 2024 Apr 24]. Availability from: https://www.adityabirlachemicals.com/pdf/Composite.pdf.
15. ASTM International. Standard Specification for Design and Performance of a Light Sport Airplane. ASTM F2245-20 [Internet]. 2020 [updated: 2023 Aug 08; cited 2024 Jan 25]. Availability from: https://cdn.standards.iteh.ai/ samples/107349/078af7bc9da34bc1a892c35efed2c727/ASTM-F2245-20.pdf
16. Abbott R. Analysis and design of composite and metallic flight vehicle structures. 2nd ed. Collingwood: Abbott Aerospace SEZC Ltd; 2016.
17. Corke TC. Design of Aircraft. 1st ed. Pearson; 2003.
18. Hauffe A. ELAMX² [Internet]. Technische Universität Dresden; 2023 [cited 2023 Nov 30]. Availability from: https://tu-dresden.de/ing/maschinenwesen/ilr/lft/elamx2/elamx?set_language=en.
19. Latifi M. Engineered Polymeric Fibrous Materials. Woodhead Publishing; 2021.
20. Markit IHS. ESDU Catalogue 2017 Validated Engineering Design Methods. 2017.
21. Chinvorarat S, Watjatrakul B, Nimdum P, Sangpet T, Soontornpasatch T, Vallikul P. Static testing for composite wing of a two-seater seaplane. IOP Conf Ser: Mater Sci Eng. 2019; 501(1):012026.

DOI: 10.60101/jarst.2024.257706

Received: August 6, 2024 | Revised: October 7, 2024 | Accepted: October 15, 2024

JOURNAL OF APPLIED RESEARCH ON SCIENCE AND TECHNOLOGY
JARST
INSTITUTE OF RESEARCH AND DEVELOPMENT
RAJAMANGALA UNIVERSITY OF TECHNOLOGY THANYABURI
ISSN ONLINE: 2773-9473
https://ph01.tci-thaijo.org/index.php/rmutt-journal

Age-dependent mathematical models of ligaments and tendons

Ratchada Sopakayang* **and Somya Poonaya**

Department of Mechanical Engineering, Faculty of Engineering, Ubon Ratchathani University, Ubon Ratchathani 34190, THAILAND

*Corresponding author: ratchada.s@ubu.ac.th

ABSTRACT

Understanding the internal structure and the underlying physical mechanisms governing the mechanical properties of ligaments and tendons, particularly the elastic modulus, across different stages of life is critical for enhancing tissue strength during growth, maturation, and aging. This knowledge is essential not only for preventing tissue failure in older adults but also for advancing the development of biomaterials that can substitute or augment ligament and tendon function across all age groups. Despite the significance of this area, a comprehensive, mechanistic understanding of the relationship between structural changes and mechanical properties over time remains largely unexplored. To date, there is a lack of detailed studies that elucidate the physical mechanisms involved in these age-related changes. The absence of such mechanistic insights highlights a significant gap in the literature, necessitating further investigation. Therefore, this research delves into the age-dependent structural and mechanical property changes in ligaments and tendons, emphasizing both growth and mature phases. Utilizing a comprehensive approach, we have developed new mathematical models that directly correlate the growth of collagen in fibrils with the increasing elastic modulus in the fibers of ligaments and tendons over time. By integrating experimental data from mouse tail tendons in published work and conducting simulations, we have observed that the cross-sectional area of collagen in fibrils and the elastic modulus of a collagen fiber increase rapidly during the growth phase and stabilize during the mature phase. Our proposed models effectively describe the trends in collagen growth and the elastic modulus of fibers in ligaments and tendons over different ages, exhibiting consistency with experimental data. Through detailed analysis, we elucidate the mechanistic relationship between collagen growth and the elastic modulus of fibers as they age. This comprehensive approach significantly enhances our understanding of the age-related structural and mechanical property changes in connective tissues, providing a robust framework for future investigations.

Keywords: Age-dependent, Mathematical models, Structural changes, Ligaments, Tendons

INTRODUCTION

The mechanical properties of ligaments and tendons, particularly their elastic modulus, play a crucial role in maintaining tissue integrity and function across the human lifespan. These properties are intricately linked to the internal structure and the underlying physical mechanisms that govern them, which evolve significantly with age. Understanding these age-related structural and mechanical changes is essential not only for improving tissue strength during periods of growth and maturation but also for mitigating the risk of tissue degeneration and failure in aging populations.

Research on improving the quality of ligament and tendon substitutes has been extensively published and continues to attract significant interest [1, 2]. To create age-appropriate and effective scaffolds, it is crucial to understand the age-related structural and mechanical property changes in connective tissues.

One critical age-related mechanical property affecting the behavior of ligaments and tendons is the elastic modulus. Understanding the structural origins that influence the elastic modulus over time is essential for describing mechanical or viscoelastic behaviors, such as tensile strength, creep, relaxation, and hysteresis, which are vital for design and prediction. This study focuses on the structural changes related to variations in the elastic modulus of fibers in ligaments and tendons over different ages.

Despite various age-related modeling and experimental approaches to understanding the physiological and mechanical changes in tissue structures over a lifetime, many issues remain unresolved [3-8]. Current research lacks a comprehensive analysis of the physical mechanisms that drive the age-dependent variations in the mechanical properties of ligaments and tendons. The literature is particularly deficient in detailed studies that investigate the mechanistic

DOI: 10.60101/jarst.2024.257688

JOURNAL OF APPLIED RESEARCH ON SCIENCE AND TECHNOLOGY

relationships between structural changes and mechanical behavior over time. This gap in knowledge underscores the need for more rigorous and targeted research to elucidate the fundamental processes underlying these changes, which could significantly advance both clinical and material science applications.

Previous studies have shown that both the structure and the elastic modulus of tissues change with aging [6, 7, 9-13]. However, the relationship between tissue growth and mechanical properties is still unclear. Some researchers believe that cross-links between collagen fibrils in ligaments and tendons increase with age [8, 14], while others report that collagen cross-linking [15] and tissue stiffness decrease in older ages [9, 15, 16]. Experimental evidence suggests that the cross-sectional area of collagen fibrils increases with age and is directly related to the stiffness of the tissues [11, 12, 17].

To clarify these relationships, this research investigates the changes in mechanical properties and structural integrity of collagenous tissues, specifically ligaments and tendons, as they age using a modeling approach. The work develops innovative constitutive models that account for both mechanical and structural shifts during growth and maturation. The study identifies two distinct phases in the lifetime of these tissues: the growth phase, characterized by a rapid increase in the cross-sectional area of fibrils and the elastic modulus of fibers, and the mature phase, where these parameters stabilize.

The proposed models effectively illustrate the relationship between the increase in the cross-sectional area of fibrils, structural changes, and the elastic modulus of fibers over time. These models accurately characterize age-dependent tissues, covering both growth and mature phases. The parameters in the models have been validated with experimental data published by Goh KL et al. in 2018 [17]. The model calculations have shown good agreement with the results from these experiments.

This research provides a significant advancement in understanding the physical mechanisms governing the mechanical properties of ligaments and tendons by focusing on the role of collagen within fibrils. Through the development of novel mathematical models, we have established a direct correlation between collagen growth within fibrils and the increase in the elastic modulus of ligament and tendon fibers over time. These models reveal that the increase in the fraction of the cross-sectional area occupied by collagen within fibrils, as well as the overall expansion of the fiber's cross-sectional area, is linearly related to the enhancement of the elastic modulus. This new insight offers a deeper characterization of the structural-mechanical relationship within ligaments and tendons, providing a foundational framework for future research into tissue mechanics and the development of biomaterials.

Building on this foundation, the next section details the development of two key models: the collagen growth model, which tracks changes in the fraction of collagen within fibrils and the fiber's cross-sectional area, and the elastic modulus model, which describes the evolution of the fibers' elastic modulus over time. These models explicitly illustrate the relationship between collagen growth and mechanical properties. In the results and discussion section, model parameters are estimated through curve fitting with experimental data from [17], and their variations are analyzed to understand their roles. The relationship between collagen growth and elastic modulus is validated through this analysis. In the conclusions, we summarize our contributions and suggest directions for future research, emphasizing further model refinement and broader applications.

MATERIALS AND METHODS

Model formulation

In this study, the growth of ligaments and tendons is characterized by the function $\rho(t)$, which describes the increase of collagen in the tissues over time. This function represents the cross-sectional area of collagen in the fibrils assembled within a collagen fiber and the total cross-sectional area of the collagen fiber. A schematic of collagen growth within a collagen fiber is shown in Figure 1, where r denotes the radius of the collagen cross-sectional area increasing over time, while r_t and L represent the radius of the total cross-sectional area and the length of the fiber, respectively.

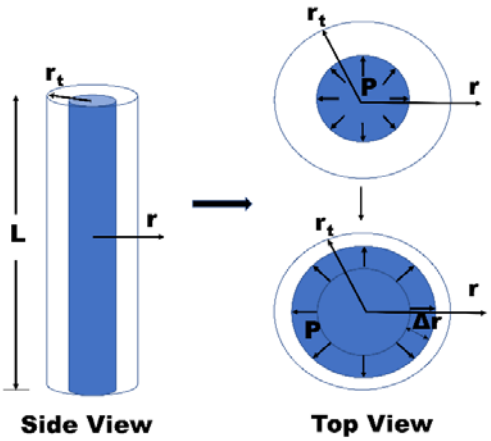

Figure 1 Structural illustration of collagen growth within a collagen fiber.

According to experimental data from a published study [17], $\rho(t)$ and the elastic modulus of the tissues, $E(t)$, increase rapidly during early ages and stabilize at the beginning of the mature ages. At this stage, $\rho(t)$ and $E(t)$ are denoted as ρ_m and E_m, respectively, and are considered constant. Therefore, in this study, ρ_m and E_m are treated as constants, while the variations of $\rho(t)$ and $E(t)$ are assumed to depend solely on the age of the tissues, t (measured in months). The detailed

DOI: 10.60101/jarst.2024.257688

JOURNAL OF APPLIED RESEARCH ON SCIENCE AND TECHNOLOGY

model formulation for $\rho(t)$ and $E(t)$ is described in the following section.

The growth model ($\rho(t)$)

We model the increase in collagen in the fibers over time using a rate equation. Therefore, the rate of change of $\rho(t)$ can be expressed as:

$$\frac{d\rho}{dt} = \frac{\rho_m - \rho}{\tau} \quad (1)$$

where τ is the constant relaxation time of tissues.

By rearranging equation (1) and integrating both sides, we can derive the expression for the growth function as follows:

$$\int_{\rho_0}^{\rho} \frac{d\rho}{\rho_m - \rho} = \int_{t_0}^{t} \frac{dt}{\tau} \quad (2)$$

$$\rho(t) = \rho_m - (\rho_m - \rho_0)e^{-\frac{(t-t_0)}{\tau}} \quad (3)$$

where ρ_0 and t_0 are the initial values of the collagen growth and the age of the tissues, respectively.

The elastic modulus model ($E(t)$)

Referring to the constitutive law of elastic materials in equation (4), where σ and ε represent the stress and strain in the collagen within the tissues, respectively, we can formulate a mathematical model for the elastic modulus of a collagen fiber in ligaments and tendons over time as follows:

$$\sigma = E(t)\varepsilon \quad (4)$$

Based on previous studies [17, 18], collagen in a collagen fiber is generated over time. To maintain a constant collagen density within the fiber, the increase in the cross-sectional area is attributed to the exerted force P distributed along the circumference of the collagen surface, causing an increase in the radius Δr in the r-direction, as shown in Figure 1. Consequently, the stress and strain due to this increase in the cross-sectional area of the collagen can be expressed as $\sigma = P/2\pi rL$ and as $\varepsilon = \Delta r/r$, respectively. Substituting these into equation (4), we obtain:

$$\frac{P}{2\pi rL} = E(t)\frac{\Delta r}{r} \quad (5)$$

Assuming that, for small deformations, the tissues behave as a linear elastic material obeying Hooke's Law (equation (4)), we can state that:

$$P = kr \quad (6)$$

where k is the stiffness constant of the collagen within the fiber.

By substituting equation (6) into equation (5) and rearranging, we obtain:

$$E(t) = \frac{kr}{2\pi rL} \times \frac{r}{\Delta r} \quad (7)$$

To express equation (7) as a function of $\rho(t)$, we multiply r/r to the right-hand side of equation (7) as follow:

$$E(t) = \frac{k}{2\pi L} \times \frac{r.r}{r.\Delta r} \quad (8)$$

For small deformations, we can approximate that $r.\Delta r \approx \int_0^{r_t} r dr = \frac{r_t^2}{2}$. Substituting this into equation (8), we obtain:

$$E(t) = \alpha\left(\frac{r^2}{r_t^2}\right) \quad (9)$$

where $\alpha = k/\pi L$ is a constant parameter of the model.

Recalling that $\rho = \frac{A}{A_t} = \frac{r^2}{r_t^2}$ and substituting it into equation (9), we obtain:

$$E(t) = \alpha\rho(t) \quad (10)$$

By substituting $\rho(t)$ from equation (3) into equation (10), we can finally derive the elastic modulus model of the tissues as:

$$E(t) = E_m - (E_m - E_0)e^{-\frac{(t-t_0)}{\tau}} \quad (11)$$

where $E_m = \alpha\rho_m$ and $E_0 = \alpha\rho_0$.

The relationship between elastic modulus (E) *and collagen fraction* (ρ) *in fibrils and the total fiber cross-sectional area*

The relationship between E and ρ can be expressed as follows:

By referencing the elastic modulus model presented in equation (11) and the growth model in equation (3), we derive Equations (12) and (13), respectively.

$$E(t) - E_m = -(E_m - E_0)e^{-\frac{(t-t_0)}{\tau}} \quad (12)$$

$$\rho(t) - \rho_m = -(\rho_m - \rho_0)e^{-\frac{(t-t_0)}{\tau}} \quad (13)$$

By dividing equation (12) by equation (13), we derive the following expression.

$$\frac{E - E_m}{\rho - \rho_m} = \frac{E_m - E_0}{\rho_m - \rho_0} \quad (14)$$

$$\frac{(E - E_0) + (E_0 - E_m)}{(\rho - \rho_0) + (\rho_0 - \rho_m)} = \frac{E_m - E_0}{\rho_m - \rho_0} \quad (15)$$

$$(E - E_0) = \left(\frac{E_m - E_0}{\rho_m - \rho_0}\right)[(\rho - \rho_0) + (\rho_0 - \rho_m)] - (E_0 - E_m) \quad (16)$$

By dividing equation (16) by $\rho - \rho_0$, the following expression is obtained.

$$\frac{E - E_0}{\rho - \rho_0} = \left(\frac{E_m - E_0}{\rho_m - \rho_0}\right)\left[1 + \frac{\rho_0 - \rho_m}{\rho - \rho_0}\right] - \left(\frac{E_0 - E_m}{\rho - \rho_0}\right) \quad (17)$$

DOI: 10.60101/jarst.2024.257688

Thus, the relationship between E and ρ can be represented by the formula for the slope of the E - ρ curve, as follows:

$$\frac{dE}{d\rho} = \frac{\Delta E}{\Delta \rho} = \frac{E-E_0}{\rho-\rho_0} = \left(\frac{E_m-E_0}{\rho_m-\rho_0}\right) \quad (18)$$

Given that E_m, E_0, ρ_m and ρ_0 are constants, the slope of the E - ρ curve remains constant. This indicates a linear relationship between E and ρ.

By assuming the initial conditions, $E_0 = 0$ and $\rho_0 = 0$, we derive the following equation, which is consistent with Equation (10).

$$\frac{E}{\rho} = \left(\frac{E_m}{\rho_m}\right) = \alpha \quad (19)$$

Based on the model formulation presented above, the overall structure of the model system is illustrated in Figure 2.

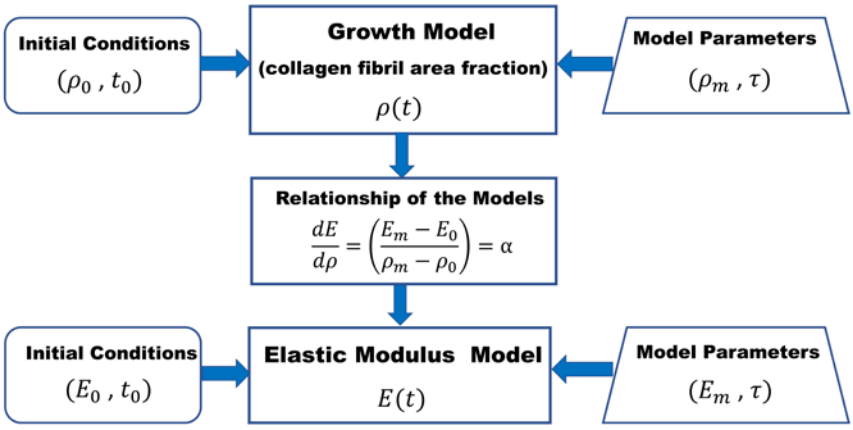

Figure 2 Schematic representation of the overall model system.

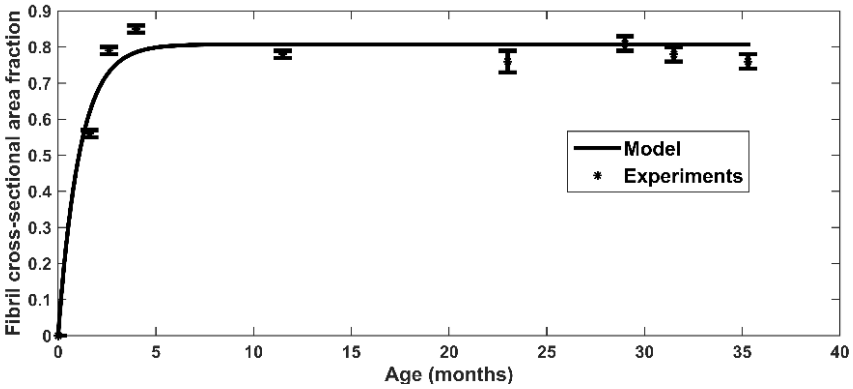

Figure 3 Experimental data showing the fraction of the cross-sectional area of collagen in fibrils and the total cross-sectional area of a fiber versus the ages of mouse tail tendons [17], along with the model fitting parameters $\rho_m = 0.8075$ and $\tau = 1.106$ months ($R^2 \approx 0.9744$).

RESULTS AND DISCUSSION

Parameter estimation of the growth model ($\rho(t)$)

To describe the growth and maturation behaviors of ligaments and tendons, the parameters (ρ_m, τ) in Equation (3) of the growth model need to be estimated. This study employed curve fitting between the mathematical model and experimental data from [17] to determine the appropriate values for these parameters.

The initial conditions for the model were set to $\rho_0 = 0$ and $t_0 = 0$. The model was then fitted to the experimental data, which included the fraction of the cross-sectional area of collagen in fibrils and the total cross-sectional area of a fiber plotted against the ages (in months) of mouse tail tendons, as reported in [17]. The curve fitting was performed using the Levenberg-Marquardt nonlinear least squares algorithm, implemented in Matlab (The MathWorks, Inc.). The parameter estimation results were found to be $\rho_m = 0.8075$ and $\tau = 1.106$ months, with a coefficient of determination $R^2 \approx 0.9744$.

As shown in Figure 3, the model fits well with the experimental data, accurately describing the characteristics of the growth and maturation behaviors of the tissues. According to the growth model (equation (3)), as $t \to \infty$, ρ approaches $\rho_m = 0.8075$, indicating that collagen growth eventually stabilizes at mature ages and becomes constant.

Parameter estimation of the elastic modulus model ($E(t)$)

The elastic modulus model (Equation 11) includes two parameters, E_m and τ. Given that τ was previously estimated as 1.106, we only need to estimate E_m to

DOI: 10.60101/jarst.2024.257688

JOURNAL OF APPLIED RESEARCH ON SCIENCE AND TECHNOLOGY

describe the stiffness behavior of ligaments and tendons over time. Therefore, we performed curve fitting between the mathematical model and the experimental results from the published study [17] to determine the appropriate value for E_m.

Assuming the initial conditions of $E_0 = 0$ and $t_0 = 0$, the model was fitted to the experimental data, which measured the elastic modulus of fibers against the ages (in months) of mouse tail tendons, as reported in [17]. Using the Levenberg-Marquardt nonlinear least squares algorithm in Matlab (The MathWorks, Inc.), we estimated E_m to be 580.8 MPa, with a coefficient of determination $R^2 \approx 0.9161$.

As illustrated in Figure 4, the model fits the experimental data well, accurately capturing the mechanical behavior of the tissues during both growth and mature ages. According to the elastic modulus model (Equation 11), as $t \to \infty$, E approaches $E_m = 580.8$ MPa, indicating that the elastic modulus of a collagen fiber stabilizes at mature ages.

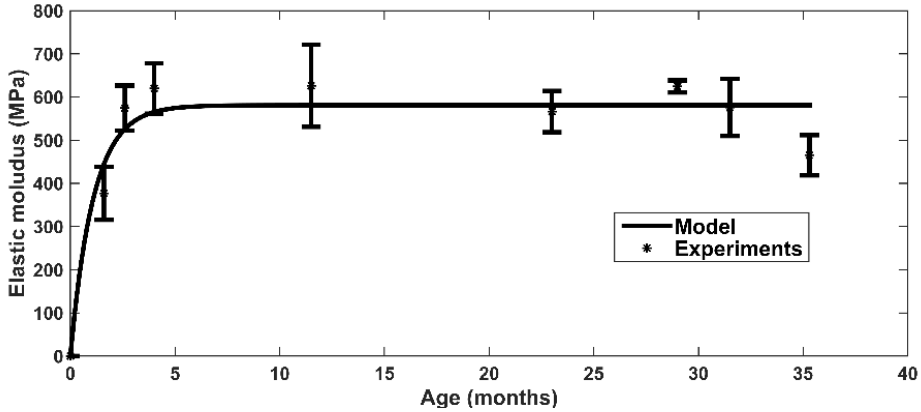

Figure 4 Experimental data showing the elastic modulus of a fiber versus the ages of mouse tail tendons [17], along with the model fitting parameters $E_m = 580.8$ MPa and $\tau = 1.106$ months ($R^2 \approx 0.9161$).

The curve fitting of the proposed models to the experimental data yielded $R^2 \approx 0.9744$ ($\pm 2.6\%$) for collagen growth and $R^2 \approx 0.9161$ ($\pm 8.4\%$) for elastic modulus, as shown in Figures 3 and 4, respectively. In biomechanics research, it is common to encounter significant data scatter, which can be influenced by factors such as the subject's age, tendon conditions, and specimen preparation processes [19]. For instance, a recent study [20] reported up to $\pm 30\%$ scatter in the values of the elastic modulus of human ligaments with aging. Similarly, another study [6] showed a polynomial function fitting to the experimental data of human tendon elastic modulus across all ages, with an R^2 of only 0.47 ($\pm 53\%$).

Given this context, the observed scatter in our model and experimental data, particularly the last data points in Figures 3 and 4 that deviate from the model calculations, falls within the expected range of experimental errors. However, further experimental data is necessary to validate these models fully. Additional data will also enable the extension of the models, potentially aiding in the development of age-appropriate interventions and treatments in fields such as orthopedics, rehabilitation, and sports medicine.

Estimation of the parameter relating the growth model to the elastic modulus model

According to Equation (10), the parameter α, which relates the growth of collagen in fibrils (growth model) to the variation in the elastic modulus of a fiber (elastic modulus model) over time, is a constant. From Equation (11), $E_m = \alpha \rho_m$, and using the previously estimated values of $\rho_m = 0.8075$ and $E_m = 580.8$ MPa, we can determine that $\alpha = 719.3$ MPa. This constant parameter α links the structural growth to the mechanical properties of collagen fibers, providing a unified framework for understanding the age-dependent behavior of ligaments and tendons.

Variation of the parameter, α, influencing the elastic modulus model

The variation of the constant parameter α, which represents the stiffness of the collagen in fibrils, influences the elastic modulus of fibers in ligaments and tendons. This relationship is illustrated in Figure 5.

As shown, when α increases, the elastic modulus in the mature region (E_m) also increases, while the time for the elastic modulus to stabilize (τ) remains unchanged.

Due to the linear relationship described by Equations (10) and (11), the behavior of α is consistent with the variations of the parameters E_m and ρ_m, which influence the elastic modulus and growth models, respectively. This implies that the primary factor affecting the elastic modulus of ligaments and tendons is the stiffness of the collagen in the fibrils.

As animals age, the amount of collagen in the fibrils increases. To maintain the same density of collagen, the cross-sectional area of the collagen fibrils must also increase. Therefore, the preserved density of collagen in the fibrils is a key property of the internal structure of ligaments and tendons, significantly influencing their elastic modulus.

DOI: 10.60101/jarst.2024.257688

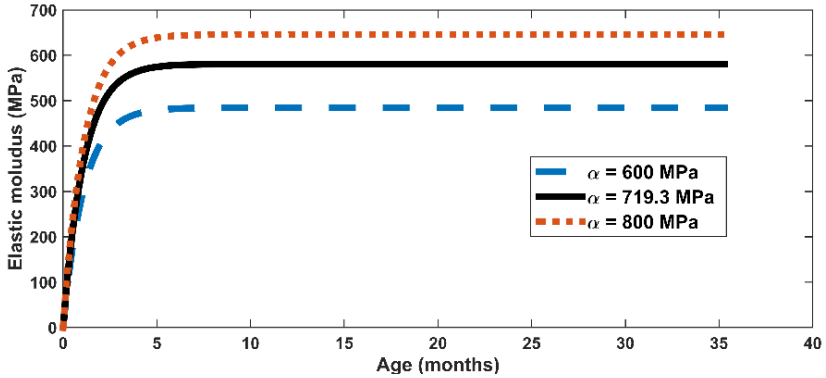

Figure 5 Impact of varying parameter α on the elastic modulus values of a fiber.

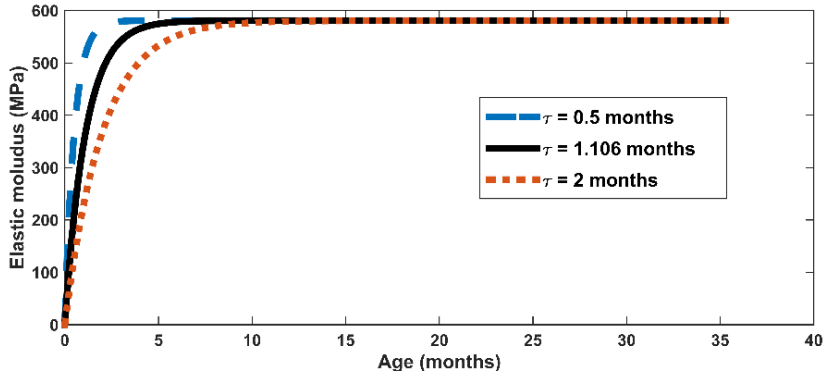

Figure 6 Impact of varying parameter τ on the elastic modulus values of a fiber.

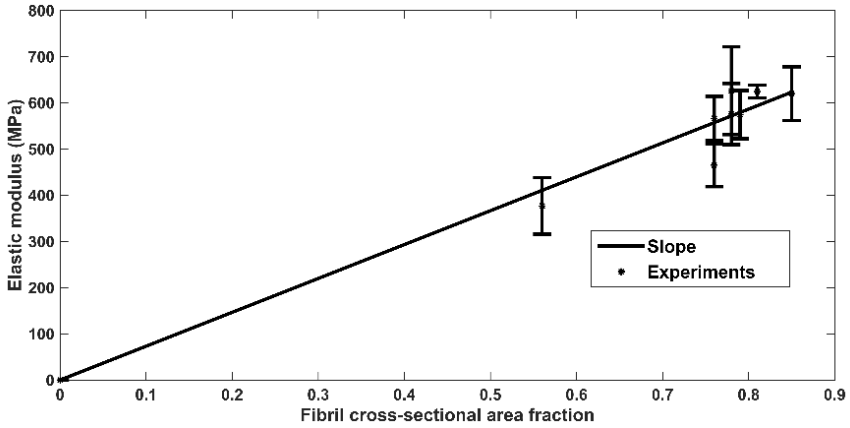

Figure 7 Experimental data depicting the relationship between elastic modulus and the collagen fraction in fibrils and the total fiber cross-sectional area [17], with the fitted slope parameter $\left(\frac{E_m - E_0}{\rho_m - \rho_0}\right) = 733.1$ MPa ($R^2 \approx 0.9554$).

Variation of the parameter, τ, influencing the elastic modulus model

The variation of the constant parameter τ, which represents the time required for the elastic modulus of fiber or the cross-sectional area of the collagen in fibrils to stabilize, impacts the elastic modulus values of fibers in ligaments and tendons. This relationship is illustrated in Figure 6.

As depicted, when τ increases, the age at which the elastic modulus stabilizes also increases, while the stable elastic modulus in the mature region (E_m) remains unchanged.

Since τ is the same in both Equations (3) and (11), the behavior of this parameter is consistent across both the growth and elastic modulus models. This indicates that the primary factor influencing the time it takes for E or ρ to stabilize in the mature region is the amount of collagen in the fibrils. As animals age, the collagen content in fibrils increases. To maintain a constant collagen density, the cross-sectional area of the collagen in the fibrils must also increase. Consequently, if the collagen growth is higher, it will take longer for the cross-sectional area of the collagen or the elastic modulus to stabilize. Therefore, the amount of growth collagen is likely a key factor in determining the relaxation time or the age at which tissues become mature.

DOI: 10.60101/jarst.2024.257688

JOURNAL OF APPLIED RESEARCH ON SCIENCE AND TECHNOLOGY

Estimation of the parameter governing the relationship between elastic modulus (E) and collagen fraction (ρ) in fibrils and the total fiber cross-sectional area

Based on Equation (18), the analysis reveals a linear relationship between E and ρ. The proportionality constant between these two parameters can be determined by the slope of the linear regression curve of E versus ρ, as demonstrated in Figure 7.

As illustrated in Figure 7, a linear relationship between E and ρ was established. The slope of the linear function was determined through curve fitting to the experimental data, incorporating the initial conditions, $E_0 = 0$ and $\rho_0 = 0$. The resulting slope was 733.1 MPa, which is in close agreement with the previously determined constant parameter $\alpha = 719.3$ MPa, indicating consistency with equation (19). This congruence between the two methods for estimating the constant parameter α offers valuable insights for the design of age-dependent experimental models in future research.

In Figures 3, 4, and 7, we present the experimental data with error bars representing the standard error of the mean (SEM). The values for the parameters ρ and E at each age were derived from the average measurements of 3-4 mouse specimens. As evidenced by the figures, the curves generated through our curve-fitting procedure closely align with the experimental data, consistently falling within the range of the error bars. This alignment underscores the robustness and reliability of the proposed models in accurately capturing the observed mechanical behavior. However, it is important to note that the goodness of fit, as reflected by the R^2 values, may improve with an increased sample size. A larger number of specimens would likely reduce variability and refine the precision of the parameter estimates, potentially yielding even stronger correlations between the models and the experimental data.

CONCLUSIONS

The experimental data [17] indicate that aging significantly affects the material composition and mechanical behavior of ligaments and tendons. Specifically, in these tissues, the fraction of the cross-sectional area of collagen fibrils and the total cross-sectional area of a collagen fiber-referred to as collagen growth-along with the elastic modulus of collagen fibers, increase rapidly during early ages (growth ages) and stabilize during middle and old ages (mature ages).

In this study, we presented mathematical models to describe these age-related changes in collagen growth and the elastic modulus of collagen fibers in ligaments and tendons. The parameters for these models were estimated using published data on mouse tail tendons [17]. Our model formulation, which assumes a constant stiffness of collagen, demonstrates that collagen growth (structural changes) is linearly related to the elastic modulus (mechanical property changes) of collagen fibers over time. Both models exhibit trends consistent with experimental data, including distinct growth and mature regions, as shown in Figures 3 and 4. The proposed elastic modulus model effectively captures the age-related trends of collagen fiber elasticity and explains the underlying mechanism of collagen growth influencing these mechanical changes.

Thus, our models provide a clear understanding of the growth mechanisms related to the mechanical properties of tissues as they age. This knowledge is crucial for comprehending the physiological origins of age-related changes in tissue components. A deeper understanding of these mechanisms can aid in addressing aging and developing preventive measures. Furthermore, the proposed models have potential applications in various aspects of age-dependent research.

Our findings indicate a linear, time-independent relationship between E (elastic modulus) and ρ (collagen fraction), highlighting the critical role of collagen quantity in tissue mechanics. This relationship, observed in mouse tail tendons, suggests that collagen's influence on mechanical behavior remains consistent over time. Future research should focus on extending this analysis to other species and tissue types to confirm the generalizability of this finding and provide a more comprehensive understanding of tissue mechanics across biological systems. Expanding experimental data in this way will enhance our ability to develop more robust, species-specific models with broader clinical and biomaterial applications. Additionally, future work will focus on extending these models to capture the declining elastic modulus in the aging phase and describe the mechanical characteristics of ligaments and tendons across different ages, reflecting the dynamic evolution observed in experimental data. This will enhance our understanding of the fundamental changes in connective tissues with age, paving the way for improved therapeutic interventions.

REFERENCES

1. Ning C, Li P, Gao C, Fu L, Liao Z, Tian G, et al. Recent advances in tendon tissue engineering strategy. Front Bioeng Biotechnol. 2023;11:1115312.
2. Burgio V, Casari S, Milizia M, Sanna F, Spezia G, Civera M, et al. Mechanical properties of animal ligaments: a review and comparative study for the identification of the most suitable human ligament surrogates. Biomech Model Mechanobiol. 2023;22(5):1645-83.
3. Fang F, Lake SP. Modelling approaches for evaluating multiscale tendon mechanics. Interface Focus. 2016;6(1):1-13.

DOI: 10.60101/jarst.2024.257688

4. Theodossiou SK, Schiele NR. Models of tendon development and injury. BMC Biomed Eng 2019; 1(32):1-24.

5. Thompson MS, Bajuri MN, Khayyeri H, Isaksson H. Mechanobiological modelling of tendons: Review and future opportunities. Proc Inst Mech Eng H. 2017;231(5):369-77.

6. Korcari A, Przybelski SJ, Gingery A, Loiselle AE. Impact of aging on tendon homeostasis, tendinopathy development, and impaired healing. Connect Tissue Res. 2023;64(1):1-13.

7. Freedman BR, Knecht RS, Tinguely Y, Eskibozkurt GE, Wang CS, Mooney D. Aging and matrix viscoelasticity affect multiscale tendon properties and tendon derived cell behavior. Acta Biomater. 2022;143:63-71.

8. Ellingson AJ, Pancheri NM, Schiele, NR. Regulators of collagen crosslinking in developing and adult tendons. Eur Cell Mater. 2022;43:130-52.

9. Thornton GM, Lemmex DB, Ono Y, Beach CJ, Reno CR, Hart DA, et al. Aging affects mechanical properties and lubricin/PRG4 gene expression in normal ligaments. J Biomech. 2015;48(12):3306-11.

10. Vafek EC, Plate JF, Friedman E, Mannava S, Scott AT, Danelson KA. The effect of strain and age on the mechanical properties of rat Achilles tendons. Muscles Ligaments Tendons J. 2018;7(3):548-53.

11. Waugh CM, Blazevich AJ, Fath F, Korff T. Age-related changes in mechanical properties of Achilles tendon. J Anat. 2012;220(2):144-55.

12. Gulick LV, Saby C, Jaisson S, Okwieka A, Gillery P, Dervin E, et al. An integrated approach to investigate age-related modifications of morphological, mechanical and structural properties of type I collagen. Acta Biomater. 2022;137:64-78.

13. Karathanasopoulos N, Ganghoffer JF. Investigating the effect of aging on the viscosity of tendon fascicles and fibers. Front Bioeng Biotechnol. 2019; 7:107.

14. Hudson DM, Archer M, Rai J, Weis MA, Fernandes RJ, Eyre DR. Age-related type I collagen modifications reveal tissue-defining differences between ligament and tendon. Matrix Biol Plus. 2021;12:1-14.

15. Magnusson SP, Beyer N, Abrahamsen H, Aagaard P, Neergaard K, Kjaer M. Increased cross-sectional area and reduced tensile stress of the Achilles tendon in elderly compared with young woman. J Gerontol A Biol Sci Med Sci. 2003;58(2):123-7.

16. Delabastita T, Bogaerts S, Vanwanseele B. Age-related changes in Achilles tendon stiffness and impact on functional activities: A systematic review and meta-analysis. J Aging Phys Act. 2018;27(1): 1-40.

17. Goh KL, Holmes DF, Lu YH, Kadler KE, Purslow PP. Age-related dataset on the mechanical properties and collagen fibril structure of tendons from a murine model. Sci Data. 2018;5(1):180140.

18. Stammers M, Ivanova IM, Niewczas IS, Segonds-Pichon A, Streeter M, Spiegel DA, et al. Age-related changes in the physical properties, cross-linking, and glycation of collagen from mouse tail tendon. J Biol Chem. 2020;295(31):10562-71.

19. Kwan KYC, Ng KWK, Rao Y, Zhu C, Qi S, Tuan RS, et al. Effect of aging on tendon biology, biomechanics and implications for treatment approaches. Int J Mol Sci. 2023;24(20):15183.

20. Peters AE, Geraghty B, Bates KT, Akhtar R, Readioff R, Comerford E. Ligament mechanics of aging and osteoarthritic human knees. Front Bioeng Biotechnol. 2022;10:954837.

DOI: 10.60101/jarst.2024.257688

Received: September 18, 2024 | Revised: November 6, 2024 | Accepted: November 8, 2024

JOURNAL OF APPLIED RESEARCH ON SCIENCE AND TECHNOLOGY
JARST
INSTITUTE OF RESEARCH AND DEVELOPMENT
RAJAMANGALA UNIVERSITY OF TECHNOLOGY THANYABURI
ISSN ONLINE: 2773-9473
https://ph01.tci-thaijo.org/index.php/rmutt-journal

Effects of drilling parameters on drill bit wear of ASTM A36 steel

Chutimon Makee, Usanee Kitkamthorn, Pusit Mitsomwang and Rattana Borrisutthekul*
School of Metallurgical Engineering, Suranaree University of Technology, Nakhon Ratchasima 30000, THAILAND
*Corresponding Author: rattana@g.sut.ac.th

ABSTRACT

Drilling is a crucial process in metal manufacturing, with drill bits being key tools for creating holes in workpieces. During drilling, wear of the drill bits occurs inevitably. Several factors affect the wear of drill bits, such as materials, workpieces, and drilling parameters. The impact of these parameters on wear is investigated to understand the effects of drilling parameters on drill bit wear. This study used a diameter of 6 mm of uncoated high-speed steel drill bits to create the hole with 30 mm depth on ASTM A36 steel. The drilling was performed utilizing the DMG Mori DMU-50 5-axis drilling machine at three different levels of spindle speed (800, 1100, and 1400 rev/min) and feed rate (120, 135, and 150 mm/min). The sensor force dynamometer measured the thrust force and the cutting torque during drilling. However, many types of wear occur on drill bits during drilling. This research investigates only flank wear on the cutting edge of drill bits. The flank wear on the drill bits was measured with the overlap image technique using an Olympus SZ61 stereo microscope with a C-P3 OPTIKA digital camera. The results showed that adjusting drill parameters to increase the feed per revolution may result in a higher drill bit flank wear rate. Additionally, to quantify the wear of the drill bit based on the number of holes drilled, both the feed per revolution and the cutting distance per hole must be considered.

Keywords: Drill bits, Drilling parameters, Flank wear, Thrust force, Cutting torque

INTRODUCTION

Drilling is an important machining process for creating holes, with the drill bit being the main tool. However, wear of drill bits during drilling is inevitable. This wear can manifest in various forms, such as crater, margin, chisel, and flank. The most critical criterion for tool life in drilling is flank wear [1-3]. The wear of a drill bit due to usage limits its lifespan and negatively affects the quality of the holes. To address these problems, the wear resistance of drill bits has been improved by focusing on the drill bit material and coatings. Proper drilling parameters can also help reduce drill bit wear. Many research studies have been conducted to understand the effects of drilling parameters on Z that drill bit wear increases with an increase in feed rate, while low feed rates and cutting speeds result in longer tool life. Turgay Kivak et al. [5], Muksin R. Harahap et al. [6], M. Balaji et al. [7], and Nur Munirah Binti Meera Mydin et al. [8] showed that drill bit wear increases with increasing cutting speed. However, previous studies have not fully clarified the effects of drilling parameters on drill bit wear. To improve understanding, some research has considered how drilling parameters influence the forces exerted on the drill bit during drilling, as explored by A. Mohan kumar et al. [9] and Ferit Ficici [10]. They showed that the feed rate affects thrust force more than cutting speed. However, they did not examine the effects of thrust forces on drill bit wear. Consequently, to further clarify the effects of drilling parameters on drill bit wear, we investigated the influence of drilling parameters on drill bit wear and combined the results of both thrust force and cutting torque to enhance our understanding.

MATERIALS AND METHODS

The high-speed steel drill bits manufactured by Nachi Technology Co., Ltd. were used in this work. The characteristics of the drill bits - surface hardness, drill bit diameter, helix angle, point angle per tooth, relief angle, flute width, runout, and radius of the point angle - are shown in Table 1. Surface hardness was assessed using the Future-Tech FM-800 micro-Vickers hardness tester. The drill bit was employed to create the hole on the ASTM A36 steel, each with a depth of 30 mm, utilizing the DMG Mori DMU-50 5-axis drilling machine. The drilling process involved two groups of parameters: the first group operated at three different levels of spindle speed (800, 1100, and 1400 rev/min) with a constant feed rate of 135 mm/min, while the second group operated at three different levels of feed rate (120, 135, and 150 mm/min) with a constant spindle speed of 1100 rev/min, as outlined in Table 2. A control

DOI: 10.60101/jarst.2024.258209

experimental condition was chosen for both groups based on the manufacturer's recommendations. The selected rotation speeds and feed rates were intentionally set below and above the manufacturer's recommended values to observe the trends and changes in the performance of the drill bits. The thrust force and torque were measured during drilling using the Kistler 4-component dynamometer (model: 9272). The schematic of the dynamometer and the workpiece setup for drilling is shown in Figure 1. After every 10 holes, the drill bits were visually inspected, and images of the drill bit surfaces were captured using an Olympus SZ61 stereo microscope with a C-P3 OPTIKA digital camera. The captured images were used to measure flank wear by the overlap technique, as shown in Figure 2. Additionally, the flank wear on the cutting edge of the drill was measured at 1 mm from the edge of the drill, following the method used in the works of V. Z. Mehrabad et al. [11].

Table 1 Characteristics of the drill bit.

Surface hardness (HV0.1)	Diameter (mm)	Helix angle (degree)	Point angle per Teeth (degree)	Relief angle (degree)	Flute width (front), (mm)	Flute width (back), (mm)	Run Out (mm)	R -Point angle (mm)
722.33	6.08	31.5	59.2	15	3.83	3.59	0.04	4.66

Table 2 Drilling parameters.

Group	Rotation speed (rev/min)	Feed rate (mm/min)
1	800, 1100, 1400	135
2	1100	120, 135, 150

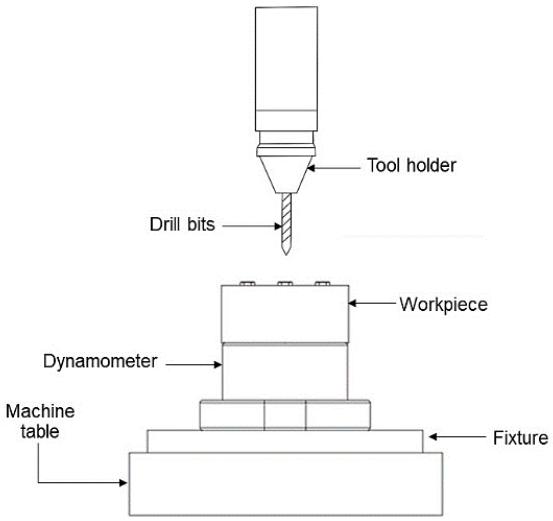

Figure 1 The schematic of dynamometer and workpiece setting for drilling.

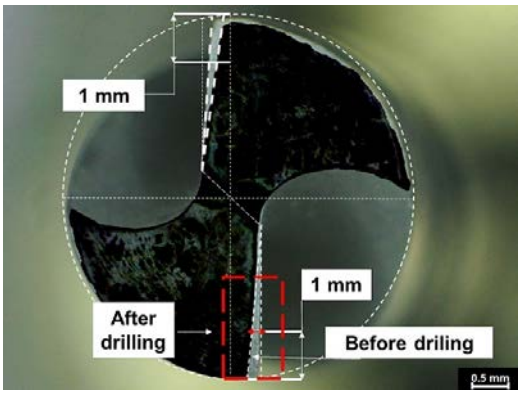

(a) The overview of measurement flank wear.

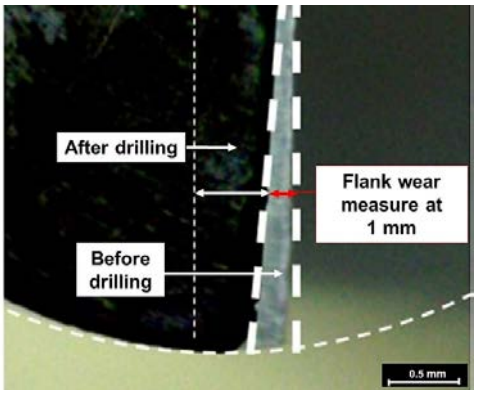

(b) Magnification image of measurement flank wear at the cutting edge.

Figure 2 The front view of the wear drill bits was measured by comparing the worn image before and after drilling the drill bits with the image overlap technique.

DOI: 10.60101/jarst.2024.258209

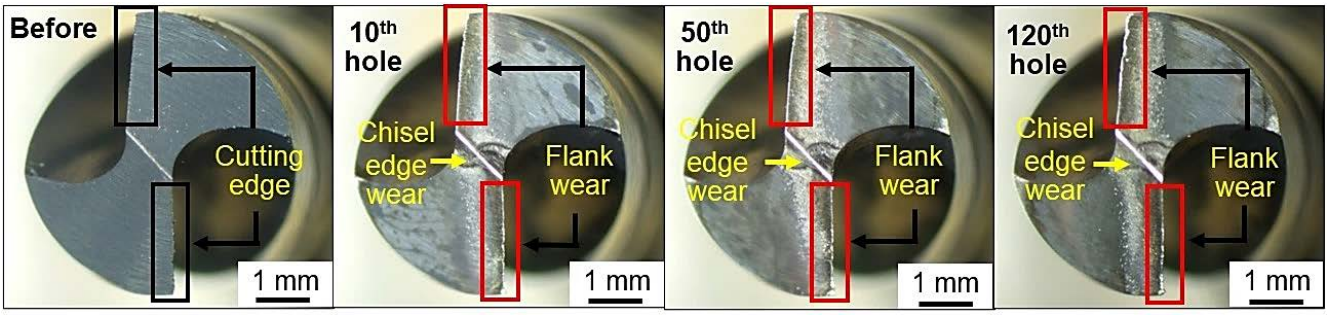

Figure 3 The front view of drill bits before and after use at 10, 50 and 120 holes. Drilling was performed under a feed rate of 135 mm/min and rotation speeds of 1100 rpm.

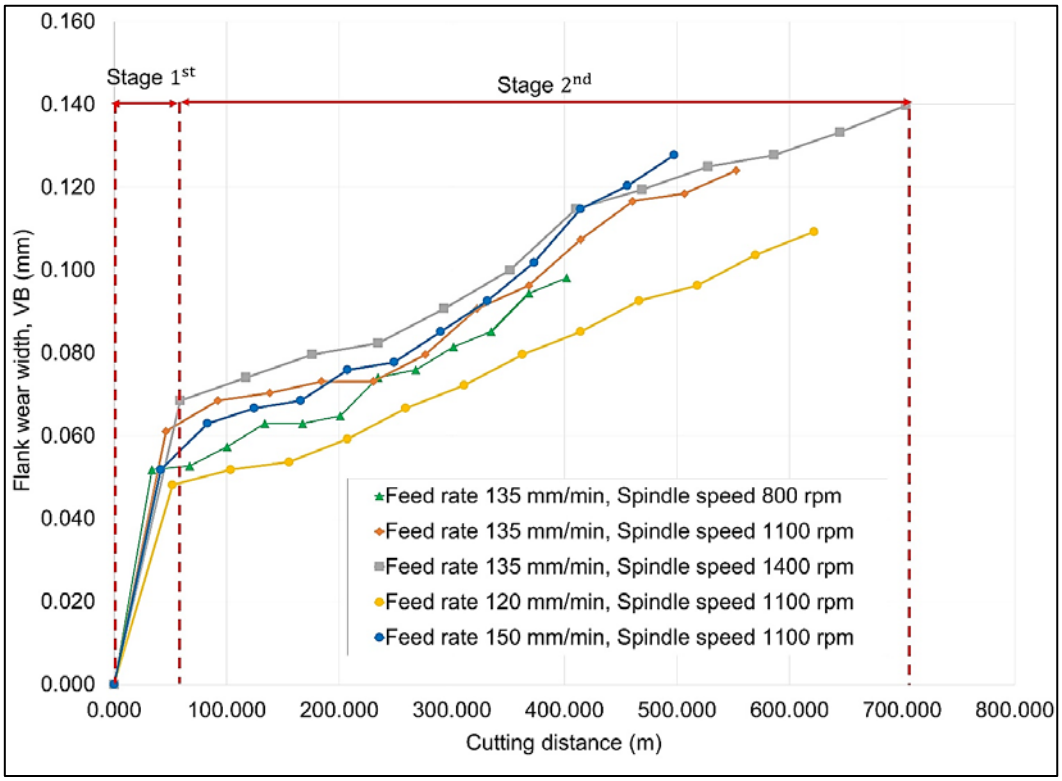

Figure 4 The flank wear of the drill bits at cutting distances with three rotation speeds and feed rates.

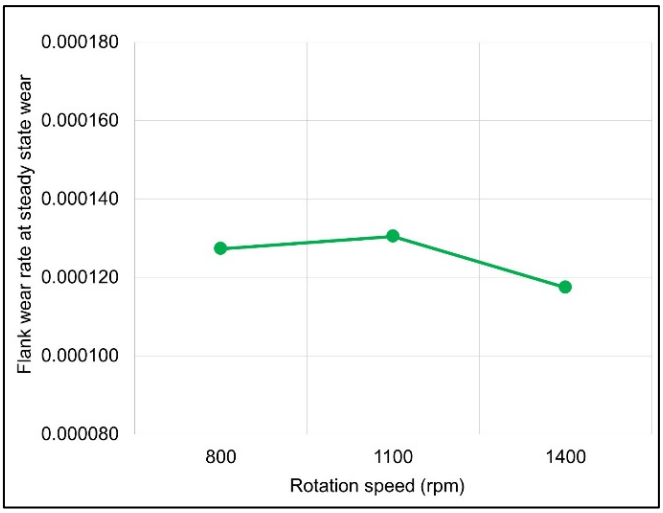

(a) Flank wear rate during drilling with difference rotation speed at constant feed rate 135 mm/min.

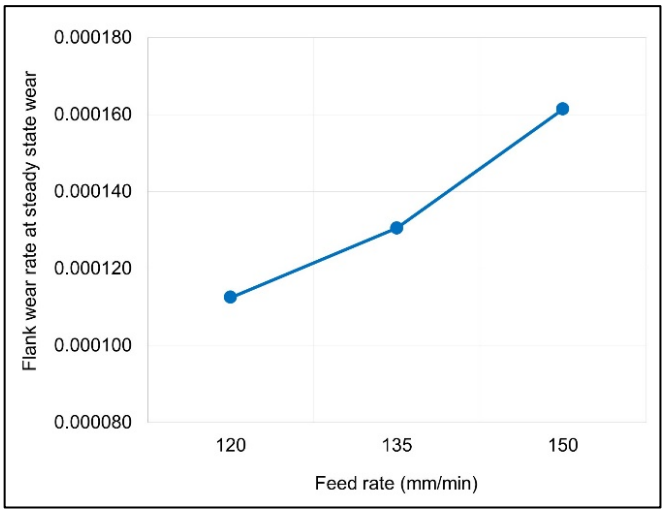

(b) Flank wear rate during drilling with difference feed rate at constant rotation speed 1100 rpm.

Figure 5 The flank wear rate of the drill bits varies with (a) three rotation speeds and (b) three feed rates.

DOI: 10.60101/jarst.2024.258209

RESULTS AND DISCUSSION

Drill bits observation

After drilling every 10 holes, wear on the drill bits was observed visually and measured using an imaging technique with the Olympus SZ61 stereo microscope equipped with a C-P3 OPTIKA digital camera. Figure 3 displays front views of the drill bits captured before and after drilling 10, 50, and 120 holes at the rotation speed of 1100 rpm and the feed rate of 135 mm/min. It was observed that initially, the cutting edge of the drill remained a straight line, but gradually transformed into a jagged line with increased drilling, indicating an increase in metal loss termed as flank wear. Notably, after drilling 50 holes, significant metal loss was evident at the cutting edge of the drill bits. Additionally, streaky scratches on the front surface of the drill indicated abrasive wear on the cutting edge. The observed changes in the cutting edge were consistent across all drilling parameters. However, the wear width of the drill was not visually discernible, making it challenging to determine which drilling parameters affected drill bit wear more significantly. Therefore, the numerical values of drill bit wear are measured and are presented in section wear of drill bits of the results.

Wear of drill bits

The wear of the drill bits was measured using an image overlap technique after every 10 holes drilled. To understand the effects of the drilling parameters on the wear of the drill bits, the flank wear is presented in correlation with the accumulated cutting distance, which is defined by the length of the moving cutting edge relative to the cut materials. The flank wear of the drill bit at accumulated cutting distances under various drilling conditions is shown in Figure 4. From Figure 4, we can observe that increasing the accumulated cutting distance increases flank wear. However, when we investigate the slope of the flank wear curve, we can divide the curve into stages with different slopes. This indicates that the flank wear of the drill bit during drilling occurs in two stages. In the initial stage, from the start of drilling to the first 10 holes, the flank wear of the drill bits occurs at a higher rate than in the second stage.

This is because the drill bit is acclimating to the workpiece, causing the cutting edge of the drill bits to be a jagged line, as shown in Figure 3. Later, the drill bits enter the second stage, where the wear increases only slightly despite the increasing accumulated cutting length. This stage is known as steady-state wear. To understand the effects of drilling parameters on the wear of the drill bit, the wear rate, determined by the slope of the wear curve in the second stage in Figure 4, was analyzed. It was found that the wear rates in the second stage under different drilling conditions were not similar. Figures 5(a) and 5(b) show the flank wear rate of a drill bit at three different rotation speeds and three different feed rates, respectively. From Figure 5(a), it can be observed that increasing the rotation speed is likely to decrease the wear rate. In contrast, Figure 5(b) shows that a higher feed rate clearly increases the flank wear rate. Because the drilling parameters used in this study are not the physical parameters needed to understand their effects on the flank wear rate, the flank wear rate was plotted against the feed per revolution, which is the physical parameter that reflects the amount of metal removed per revolution, as shown in Figure 6. It can be seen that increasing the feed per r

Thrust force and cutting torque during drilling

In order to more deeply understand the effects of drilling parameters on the wear of the drill bit, thrust force and cutting torque were investigated. Figure 7 shows examples of thrust force and cutting torque during drilling at a rotation speed of 1100 rpm and a feed rate of 135 mm/min. Figure 7 indicates that the characteristics of the thrust force and cutting torque of the drill bits during drilling can be divided into four main stages. In stage A, the thrust force and cutting torque increase rapidly to a peak. These occurred when the drill bit touched the surface of the workpiece until the tip of the drill bit is fully embedded in the workpiece, causing a gradual increase in thrust force, and cutting torque. Subsequently, the thrust force and cutting torque enter stage B as the drill bit tip is thoroughly drilled into the workpiece. Stage B's thrust force and cutting torque decrease towards a steady state, stage C. In stage C, the thrust force and cutting torque remain constant until the drill bit reaches the predetermined depth. Finally, in stage D, the thrust force and cutting torque sharply decrease as the drill bit moves out of the workpiece. From the thrust force and cutting torque characteristics during drilling, it can be recognized that the thrust force and cutting torque in stage C represent the forces involved in cutting ASTM A36 steel under various drilling conditions. Figure 8 shows the effects of rotation speed and feed rate on the thrust force and cutting torque, respectively. Figure 8 shows that the thrust force and cutting torque during drilling decrease with increasing rotation speed and decreasing feed rate.

To understand the results of drill bit wear and force during drilling, the relationships between forces at steady state wear and flank wear rate and the relationship between feed per revolution and forces at steady state wear were plotted and analyzed as shown in Figures 9 and 10. Figure 9 shows the relationship between thrust force and cutting torque, which affects the flank wear rate. As demonstrated in Figure 9, an increase in both thrust force and cutting torque increases the flank wear rate.

DOI: 10.60101/jarst.2024.258209

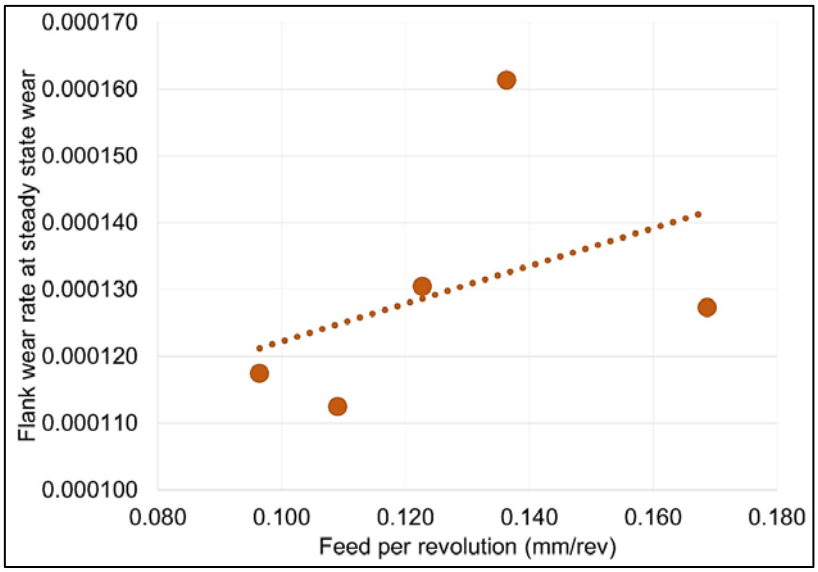

Figure 6 Flank wear rate at steady state wear various feed per revolution .

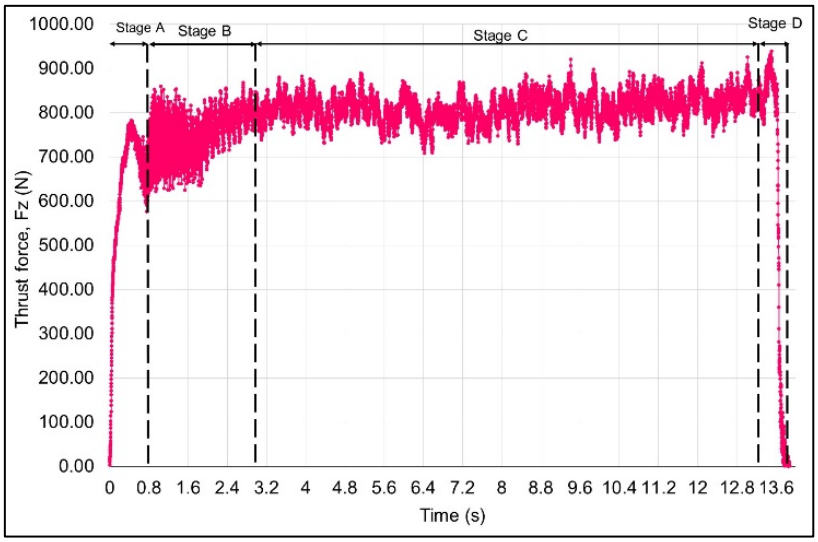

(a) Thrust force

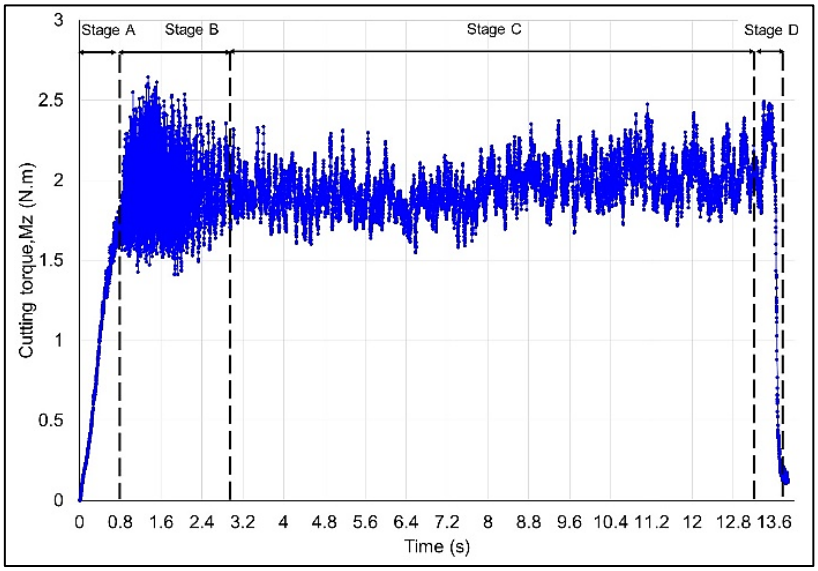

(b) Cutting torque

Figure 7 The example of (a) thrust force and (b) cutting torque during drilling as 1 hole with 1100 rpm of rotation speed and 135 mm/min of feed rate.

1

DOI: 10.60101/jarst.2024.258209

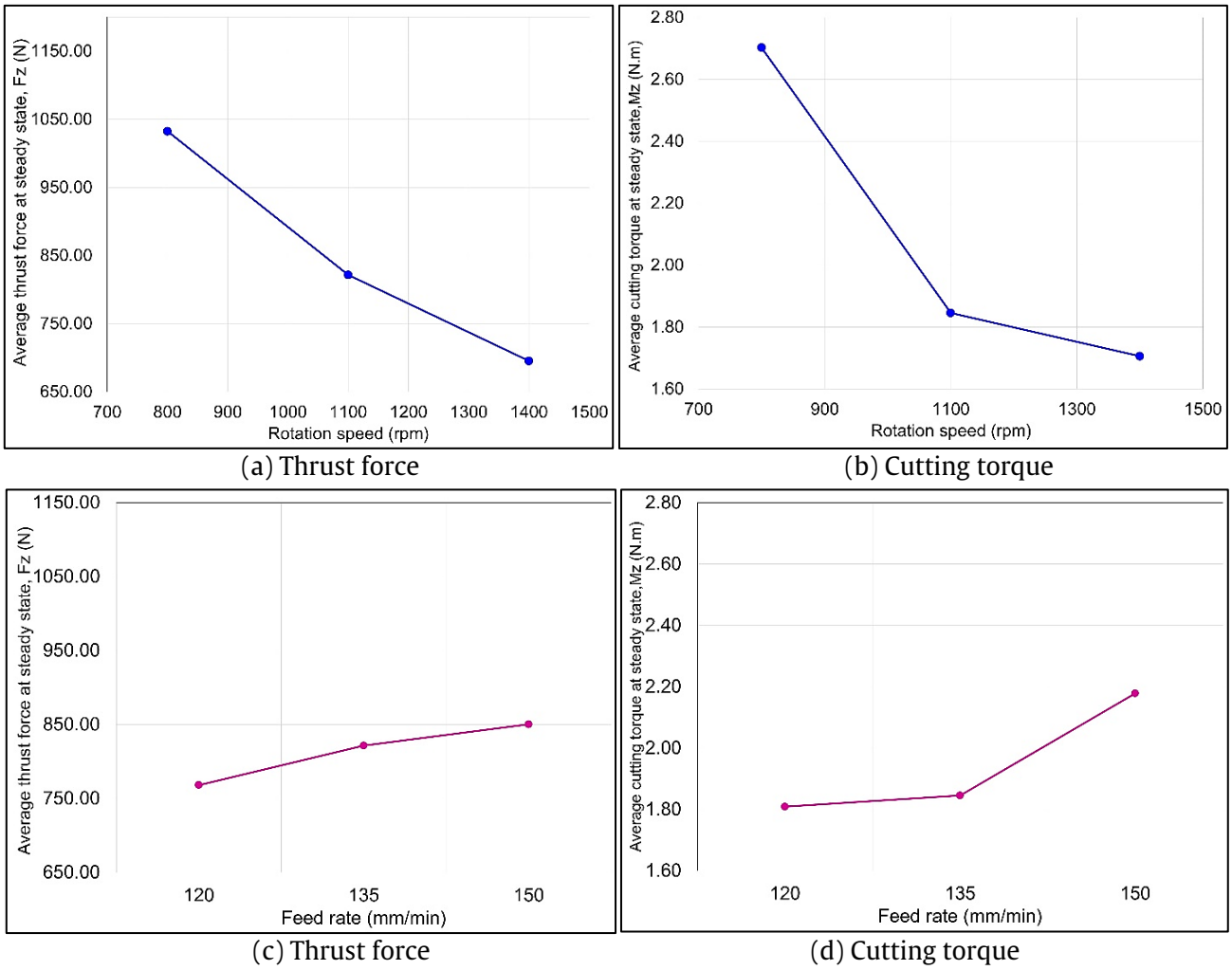

(a) Thrust force (b) Cutting torque

(c) Thrust force (d) Cutting torque

Figure 8 The average of (a,c) thrust force and (b,d) cutting torque of drill bits drilling at 3-13.3 seconds with three rotation speeds and feed rates.

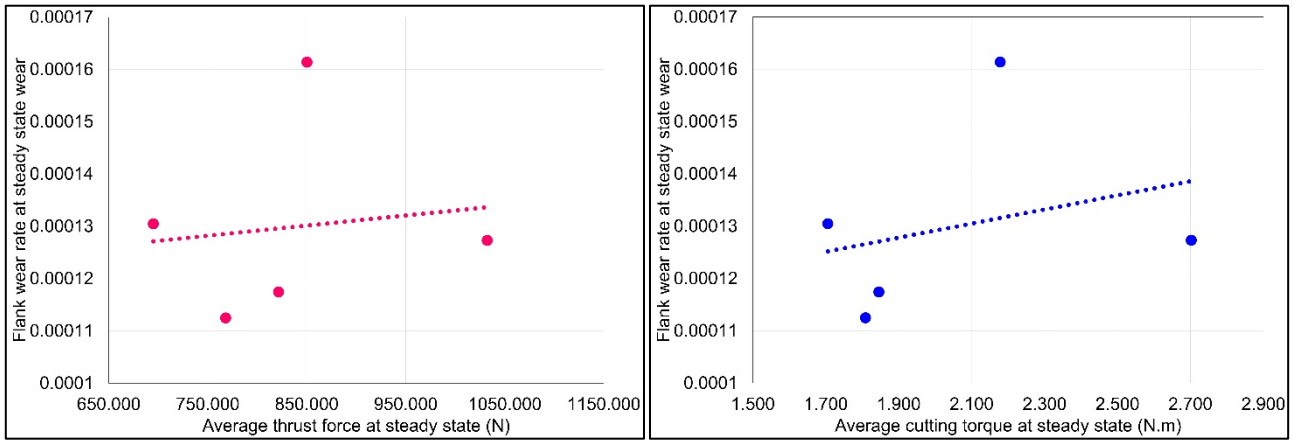

(a) Thrust force (b) Cutting torque

Figure 9 The average (a) thrust force and (b) cutting torque on flank wear rate at steady state wear.

This is because the flank wear of the drill bit is a type of abrasive wear that generally increases with the force exerted between the cutting tool and the workpiece. Figure 10 shows that a higher feed per revolution results in higher thrust force and cutting torque. Therefore, it can be recognized that adjusting drill parameters to increase the feed per revolution may result in a higher flank wear rate of the drill bit. Additionally, if we want to quantify the wear of the drill bit by the number of holes created, both the feed per revolution used and the cutting distance per hole must be considered.

DOI: 10.60101/jarst.2024.258209

JOURNAL OF APPLIED RESEARCH ON SCIENCE AND TECHNOLOGY

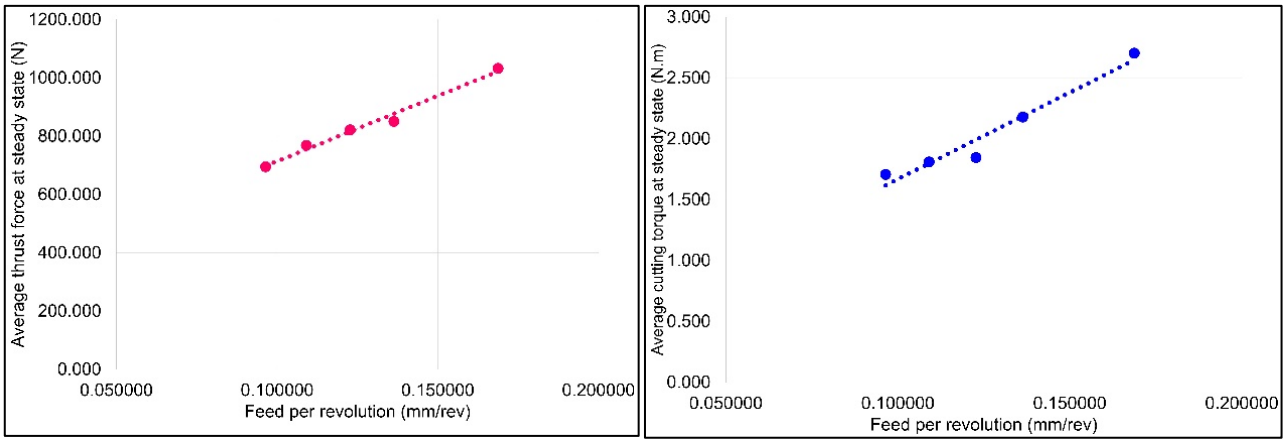

(a) Thrust force (b) Cutting torque

Figure 10 Effect feed per revolution on (a) thrust force and (b) cutting torque.

CONCLUSIONS

This study investigated the influence of feed rates and rotation speeds on drill bit wear. Thrust force and cutting torque during drilling were recorded, and their relationships with steady-state flank wear rate were analyzed to explain the wear of the drill bit. It can be recognized that adjusting drill parameters to increase the feed per revolution may result in a higher drill bit flank wear rate. Additionally, to quantify the drill bit's wear by the number of holes created, both the feed per revolution used and the cutting distance per hole must be considered.

ACKNOWLEDGEMENT

The authors would like to express their sincere gratitude to Nihon Techno Heat Treatment Co., Ltd. for their support in providing the materials used in this study.

REFERENCES

1. Sandvik Coromant. Drilling formulas and definitions [Internet]. US - Mebane, NC: Sandvik Coromant; Available from: https://www.sandvik.coromant.com/en-us/knowledge/machining-formulas-definitions/drilling-formulas-definitions.
2. Mohammed T, Hayajneh M. Prediction of cutting tool life in drilling reinforced aluminum alloy composite using a fuzzy method. Int J Mater Metallurgical Eng. 2016;10(4):431-7.
3. ISO (International Organization for Standardization). Tool-life testing with single-point turning tools (ISO 3685). 2nd ed. Geneva: ISO; 1993.
4. Sultana AZ, Sharif S, Kurniawan D. Effect of machining parameters on tool wear and hole quality of AISI 316L stainless steel in conventional drilling. In: 2nd International Materials, Industrial, and Manufacturing Engineering Conference, MIMEC2015; 2015 Feb 4-6; Bali, Indonesia: Elsevier B.V; 2015. p. 202-7.
5. Kivak T, Habali K, Seker U. The effect of cutting parameters on the hole quality and tool wear during the drilling of Inconel 718. G U J Sci. 2012; 25(2):533-40.
6. Harahap MR, Nasution AH, Napid S. The effect of cutting speed on the wear and tear of Dormer A100 Brazil drill bit applied to gray cast iron. Int J Res Rev. 2022;9(12):586-91.
7. Balaji M, Venkata Rao K, Mohan Rao N, Murthy BSN. Optimization of drilling parameters for drilling of Ti-6Al-4V based on surface roughness, flank wear and drill vibration. Meas. 2018;114: 382-9.
8. Mydin NMBM, Dahnel ANB, Raof NA, MK NK, Mokhtar S. The effect of cutting parameters on tool wear in drilling aluminium 7075. Mattingley Publishing Co Inc. 2022;83:1274-80.
9. Mohan Kumar A, Parameshwaran R, Rajasekar R, Harissh Ragavendra VC, Praveenraj N. Effect of thrust force, torque, and induced temperature on Kevlar reinforced composites during drilling process. Mater Today Proc. 2021;45:522-8. Available from: https://doi.org/10.1016/j.matpr.2020.02.162.
10. Ficici F. Investigation of thrust force in drilling polyphthalamide (PPA) composites. Meas. 2021; 182.
11. Zakeri Mehrabad V, Pourmostaghimi V. Tool wear modeling in drilling process of AISI1020 and AISI8620 using genetic programming. Adv Des Manuf Technol. 2017;10(1):93-100.

DOI: 10.60101/jarst.2024.258209

Received: September 27, 2024 | Revised: November 11, 2024 | Accepted: November 15, 2024

JOURNAL OF APPLIED RESEARCH ON SCIENCE AND TECHNOLOGY
JARST
INSTITUTE OF RESEARCH AND DEVELOPMENT
RAJAMANGALA UNIVERSITY OF TECHNOLOGY THANYABURI
ISSN ONLINE: 2773-9473
https://ph01.tci-thaijo.org/index.php/rmutt-journal

Investigation of propeller configuration effects on the flight stability of unmanned aerial vehicles

Nutdanai Chompoosri*

Satit Prasarnmit Demonstration School, Bangkok 10110, THAILAND
*Corresponding author: nutdanaiboss08@gmail.com

ABSTRACT

This study investigates the flight stability of unmanned aerial vehicles (UAVs) by comparing two-, three-, and six-blade propellers. The experiment uses a self-made drone with a 3D-printed polylactic acid (PLA) frame and an Arduino-based flight control system to create an efficient UAV prototype. The flight tests are conducted in a controlled environment, eliminating flight confounders such as wind and temperature, and the three types of propellers are of similar size. Stability was assessed by measuring deviations in the drone's X and Y axes while hovering within ±30 degrees, and standard deviation (SD) was calculated to quantify variability. The tests revealed that propeller count significantly impacts stability and overall performance. The three-blade propeller provided the best stability, with the smallest SD in the X-axis at 10.85 and Y-axis at 11.85, and showed the least deviation over ±30 degrees during take-off and flight. While the 2-blade propeller has the least stability in flight, with a value of 15.08 in the X-axis and 16.3 in the Y-axis, showing a deviation exceeding ±30 degrees several times throughout the test, the 6-blade propeller demonstrates intermediate performance, with a value of 12.71 in the X-axis and 15.57 in the Y-axis, which is more stable than the 2-blade propeller but still less stable than the 3-blade propeller. The results of this study provide UAV design data by studying the factors in selecting propellers with different numbers of blades for drones, presenting information on the importance of propeller selection for drone flight performance and stability. The results of this study can be applied to various drone applications, such as aerial photography, agriculture, or industry. Finally, in the future, other factors are expected to affect the differences in the number of blades regarding energy efficiency and flight duration.

Keywords: Drone stability, Arduino control system, Unmanned aerial vehicles (UAV)

INTRODUCTION

The most dramatic evolution of some improvements due to recent advances in information technology and artificial intelligence already shapes many aspects of autonomous systems, especially UAVs. The systems cover every detail, from specifically non-piloted aircraft to piloted flying robots that can fly without a person on board [1]. Fixed-wing, hybrid vertical take-off, and landing (VTOL) hybrids comprise the three core UAV types, representing rotorcraft and tiltrotor models. Rotorcraft series: subcategorizing into single-rotor (helicopter style) and multi-rotor variants [2]. Drones bring many advantages over traditional vehicles in the same context, and one of the areas where we can see this transformation taking place is logistics. These benefits are as follows: high-speed operation at a constant speed; it handles no road infrastructure requirement; public navigation to a direct path with traffic wouldn't be an issue [3]. Industry leaders have anecdotally documented drone use across various applications, such as Shell for oil platform flare stack inspection, Zipline for medical supplies delivery in Africa, and IKEA for real-time warehouse inventory management [4]. Figure 1 highlights the core engineering fields responsible for the design of UAVs tailored to different missions. In the design of UAVs, primary emphasis has been placed on mechanical systems, which have been analyzed, and visualization tools have been used way ahead of the process. The chosen had to offer both in how light it was (most of the work that was done for these materials was aimed at ensuring they could hold up to the weight they needed to support while also allowing for the craft to fly as long as possible given necessarily limited battery life). This is particularly clear in the case of commercial UAV models and flying saucers, where the weight should be optimized to have enough efficiency on take-off and long-range autonomy [5]. Although UAV use is becoming more common, cost remains a major barrier to broad research adoption because of high primary acquisition, maintenance, and training costs. Low-cost prototyping appears to be a valid strategy in this context to grant local actors more

DOI: 10.60101/jarst.2024.258251

agency, may they be biodiversity conservation managers [6].

The evolution of UAV materials has allowed manufacturing savings and has been the core approach to reducing UAV costs. Modern-day UAVs depend largely upon high-strength, low-weight carbon fiber composites to replace the earlier aerospace aluminum of manned aircraft [7]. In this context, additive manufacturing and 3D printing technology have become game changers in empowering the evolution of UAVs. It is a layer-wise process in which materials are deposited following digital models, providing flexibility and economic viability for small-batch production of parts with intricate geometries [8]. The fast development of 3D printing has dramatically changed prototyping, offering rapid and accurate facets in UAV production [9]. Polylactic acid (PLA), which is derived from starch like corn and sugar cane, has become one of the most common 3D printing materials. Its medium cost, biodegradability, and versatility make it a proper material for many fields of application (such as food packaging or medical devices) [10]. PLA provides a viable solution for using chassis fabrication in UAV construction. Though not as strong (good stiffness to weight) for lightweight applications, the lightweight nature of PLA is a large contributor to the weight savings achievable, consequently increasing fuel efficiency and payload capability for UAVs [11].

Control systems operated by microcontrollers underpin modern UAV operations. As a breakthrough technology in UAV technology, these purpose-built embedded systems are revolutionizing how specific device functions can be more efficiently handled and have correspondingly begun to find use within new drone designs and in wide-ranging environments like our homes and research laboratories. While general-purpose processors are too flexible, microcontrollers are designed for specific tasks that allow handling details across a range of devices and make them popular in modern technology [12]. Arduino is a general-purpose, open-source microcontroller platform that is widely used in the industrial sector. It is used in embedded systems and the Internet of Things (IoT). The advantages of this ecosystem, a combination of hardware, software, and developer communities for IoT, include cheaper, cost-effective system design, flexibility across platforms, and ease in interfacing with a wide range of input/output devices [13-14]. Arduino has achieved widespread appeal because of its easy-to-setup and easy-programming environment, leveraging C++-derived language as well as the Integrated Development Environment (IDE) to develop and execute code. Developers at any level of competency are afforded ease-of-use courtesy of this simple syntax and IDE. Its open-source architecture, versatility, and cost-effectiveness have since made it the platform of choice for many different applications within academia or at an industrial level [15].

The incorporation of private Arduino autopilot components in the flying versions of UAVs can control some activities and maneuvering actions throughout flight [16]. Rotary Wing UAVs, like quadcopters, have been the main driving factor for application development requiring vertical take-off, landing, and hovering. With best-in-class stability and control, they are a perfect choice for breaking the ice across various industries, and their compact body and lightweight ensure fluid deployment. The current research inclines toward performance enhancement via vibration and noise reduction, rotor efficiency optimization, as well as advanced stability systems [17]. Those drones employ four multi-bladed propellers that transform mechanical energy into aerodynamic thrust. Propeller designs vary from fixed-pitch to variable-pitch, and blade geometry, rotational speed, and airspeed are critical for the overall performance of a propeller [18]. Flow fields are considerably affected by distributed propellers in distributed propulsion systems, which lead to a non-linear aerodynamic performance. Off-axis freestream/axial directions incoming to the propeller cause oblique inflows, creating off-primary thrust and moment forces. The combined multi-directional effects can detriment flight stability, and therefore, it is necessary to have information pertaining to the propeller dynamics as soon as possible in the design process [19].

Zheng et al. (2020) studied flight stability and developed a fully tilt-controlled drone platform that can move in different directions and angles. During testing, the platform can tilt up to 30 degrees while hovering, and the drone remains stable at this angle. An important technical reason for maintaining the tilt angle of no more than 30 degrees is that exceeding this point can cause the thrust adjustment mechanism to lose its efficiency, resulting in instability and possibly preventing rotation. Therefore, it is necessary to maintain a tilt angle of no more than 30 degrees to maintain stability while hovering and precisely control the direction of movement [20].

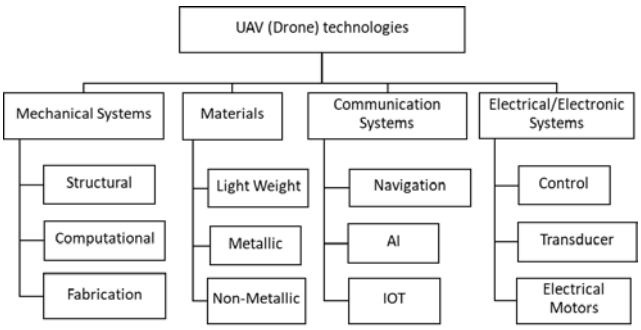

Figure 1 Key Technological Components of UAV (Drone) Systems.

This study presents the design and construction of a UAV using a PLA-printed frame controlled by an Arduino board. This UAV is made of PLA via a 3D printing process, which is low-cost and easy to customize. The

DOI: 10.60101/jarst.2024.258251

JOURNAL OF APPLIED RESEARCH ON SCIENCE AND TECHNOLOGY

main objective of the study is to analyze flight stability by comparing three types of propellers, 2-blade, 3-blade, and 6-blade propellers, to obtain information on the effects of different numbers of propellers on flight stability and controllability. Such studies are very important in designing UAVs that require stability for specific applications, such as aerial photography, precision agriculture, and infrastructure inspection. Therefore, this research provides information to understand the factors of the number of propellers on flight and can be used as a guideline for developing efficient UAV systems for practical applications in industry and further research. The experimental results can also be applied to develop propellers that can change the number of blades during flight, allowing the UAV to have higher flexibility and efficiency in various situations.

MATERIALS AND METHODS

A. Drone construction and materials

This study analyzes the flight stability of a drone by examining the effects of different propeller blade numbers. The drone is a 4-arm model, made from PLA material using 3D printing. Its structural frame supports the equipment and secures the arms. The drone's dimensions are 5.9 cm in width, 19.8 cm in length, and 12.8 cm in height. Each arm measures 2.3 cm in width, 14.3 cm in length, and 1.6 cm in height. The total weight of the drone, excluding the propellers, is 1.2 kilograms after all equipment is installed, as shown in Figure 2.

From Figure 3. The tested drone is equipped with an Arduino-based flight control system, a receiver for remote control operations, and a gyroscope sensor to monitor tilt angles during flight. The key components of the drone are as follows:

1. Components:
   - o Lower base body: 1 part.
   - o Upper base body: 1 part.
   - o Drone arms: 4 parts.
   - o 2-blade propellers: 4 parts.
   - o 3-blade propellers: 4 parts.
   - o 6-blade propellers: 4 parts.
2. Control System:
   - o Microcontroller ESP32: 1 part.
   - o Arduino UNO R3: 1 part.
   - o Remote control Flysky FS I6X: 1 part.
3. Electrical Components:
   - o Gyroscope sensor MPU6050: 2 parts.
   - o Receiver FS IA6B: 1 part.
   - o Battery lipo 3 cell 11.1 V: 1 part.
   - o Brushless motors A2212/6T 2200KV: 4 parts.
   - o Electronic Speed Controller (ESC) 30A 5V/2A: 4 parts.

The necessary software for the operation includes Arduino IDE for programming the drone's flight control and data collection via ESP32, which the ability to access Wi-Fi and Bluetooth. It uses the advantage of accessing Wi-Fi of the ESP32 to send data to the Blynk IoT platform to collect data during flight, which is used to design the drone's components and structure for 3D printing and Blynk IoT, an IoT platform for creating a dashboard to monitor real-time data and control devices over the internet.

Figure 2 UAV (Drone) from PLA material.

Figure 3 Materials and equipment for UAV installation.

B. Circuit diagram

Figure 4 presents the circuit diagram of the drone, comprising various components, each with distinct functions and operational roles. The specific details of each component are as follows:

Receiver FS IA6B: receives control signals from the remote control and transmits them to the Arduino board through Channels 1-4, connecting to the digital ports of the Arduino.

1. Arduino UNO R3: acts as an input, receiving signals from the receiver through Channels 1-4 to the digital ports of the Arduino and then controlling the operation of the brushless motors on all four arms via the speed controller.
2. Electronic Speed Controller (ESC): Adjusts the frequency of the electrical signals to control the speed and rotation of the brushless motors, providing a means for making propellers spin at a higher or slower rate. To maintain the speed of brushless motors,

DOI: 10.60101/jarst.2024.258251

take control signals from Arduino in brushless motors. Furthermore, it also regulates power delivery for optimal motor performance via the ESC.

3. Duplicate both the gyro sensor MPU6050 (SDA and SCL port to Arduino). It measures rotation or tilt in multiple axes of the drone. The gyroscope then sends this information to the Arduino so that the drone can be balanced to steer through the air consistently.

4. Tercell 11.1 VDC: rated at 11.1 VDC, is the power provider to other parts on the PCB. Components that run with higher requirements (up to 12 VDC) like the ESC and the Arduino are powered right through it, while others, such as the gyroscope or ESP32, are powered. Full System Wiring Diagram This diagram also shows where every component is wired to.

5. The data collection methodology used is illustrated in the circuit diagram in Figure 5, where we collect the data from a gyroscope sensor measuring the axis. The measured values are sent to the ESP32 by the sensor, which collects the flight data in this way. This data is then sent to the Blynk IoT app for real-time recording and viewing, allowing us to analyze flight stability. The details are as follows:

5.1 The Gyroscope MPU6050 module connects to the ESP32 via the ports of SDA (GPIO21) and SCL (GPIO22). The sensor detects rotational and tilt movements across all axes, transmitting angular values or rotation rates to the ESP32 microcontroller.

5.2 ESP32 is a microcontroller and integrated Wi-Fi/Bluetooth solution that has been designed for long-distance data transmission applications. This time around, the ESP32 gets axis measurements from the Gyroscope MPU6050 sensor and sends that data to display in the Blynk IoT dashboard.

5.3 What is the Blynk IoT platform? In this case, it's used to show the axis data collected from the drone in real-time during flight. The results will then be analyzed to determine the flight stability of a drone in future studies.

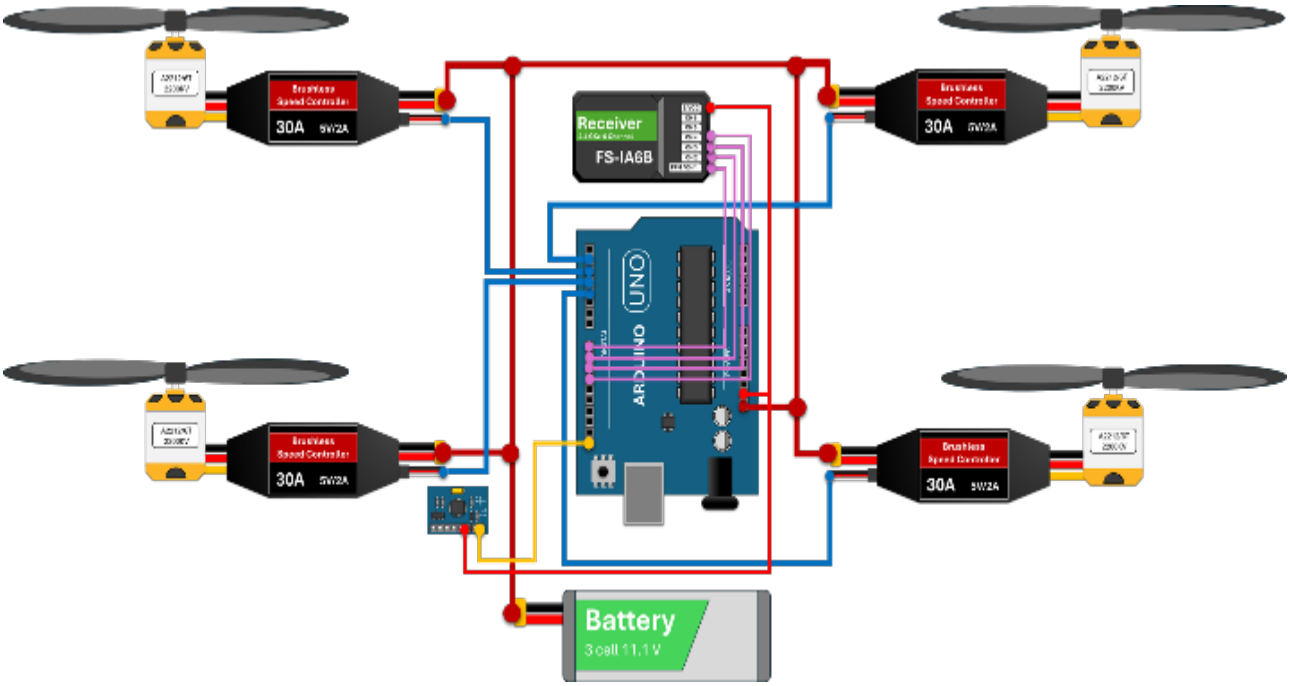

Figure 4 Circuit Diagram of UAV.

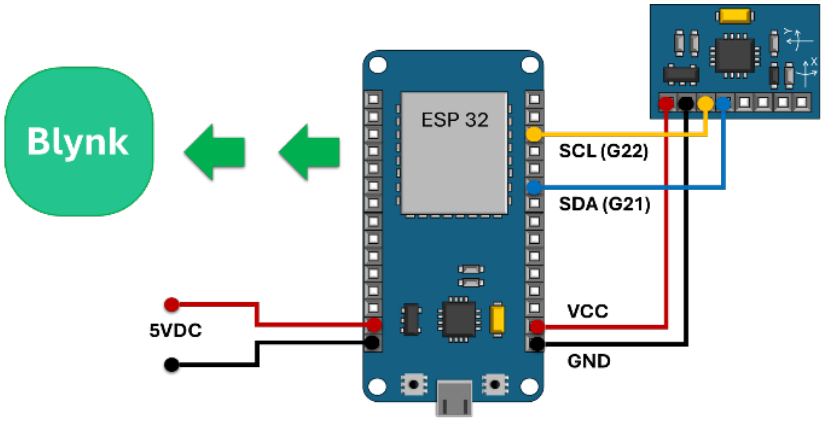

Figure 5 Circuit diagram of ESP32 for data collection.

DOI: 10.60101/jarst.2024.258251

C. Experimental methodology

All tests will be performed in a controlled environment to ensure the most accurate measurements possible and keep testing as bias-free as possible. That includes tightly controlled temperature and humidity (free from outside breeze influence). The measures provide a commonality and consistency of conditions between all flight tests in the experiment.

Figure 6 Drone mounting base for flight testing.

The flight test set-up is shown in Fig. 6, and the levels are installed within a controlled, closed environment where environmental parameters are strictly controlled. The testing rig holds the drone at a constant altitude level, ensuring stable flight. To ensure the stability of the base, a leveled water scale was used to level up the surface and make it completely flat. This integral subsequent detail removes potential discrepancies, providing a constant and standardized surface from which every test article can launch.

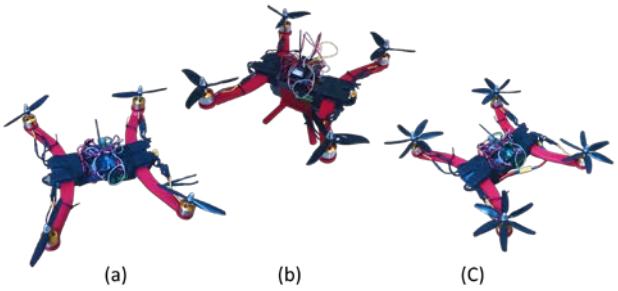

Figure 7 Drone propeller configurations: (a) 2-blade, (b) 3-blade, and (c) 6-blade.

This study compares props with two blade weights of 3 grams, three blade weights of 5 grams, and six blade weights of 6 grams to assess the drone's stability (Figure 7). Each propeller has a diameter of roughly 4 inches, and since they are all lightweight, we may disregard their weight. These three propeller types were chosen because they are simple to purchase and assemble drone equipment. A single drone, shown in Figure 8, Including devices circuits and brushless motors was used for all the tests, and it had a weight of around 1.2 kilograms, a length of 37.4 cm, a width of 29.6 cm, and a height of 12.8 cm.

Figure 8 The drone is mounted onto the test stand.

In this work, the drone is attached in a free-joint mount at its center point, which restricts it to only being able to fly 20 cm high but with the ability to be tilted. The motors are started at maximum speed, and the time until they reach maximum is recorded for 2 minutes 30 seconds. Telemetry for tilt data is collected from Y and X axes to determine flight stability. During the testing, every type of propeller is exposed to equal conditions, in which it is certain that only one thing changes for the same situation during each flight stability test-the number of propeller blades.

RESULTS AND DISCUSSION

A. Effect of blade numbers on flight stability

This study utilized published data and test results from three different propellers to investigate the influence of the number of blades on flight stability. During each test, the drone flew at peak power for 2 minutes 30 seconds but eliminated the first and last 15 seconds for instability incurred in take-off and landing (landing was brutal). Analysis of a 2-min stable flight period In the assessment, deviations from the zero reference were measured within a threshold tilt range of ±30 degrees to consider for stability calculations. Tilts over this range indicated that either control was lost or stability had been diminished and were quantified in the X- and Y-directions, as illustrated in Figure 8.

Figure 8 X and Y axes of Drone.

In measuring data fluctuations, drone flight is affected by factors that alter its tilt from a stable

DOI: 10.60101/jarst.2024.258251

JOURNAL OF APPLIED RESEARCH ON SCIENCE AND TECHNOLOGY

axis. When testing different propellers, a high standard deviation (SD) indicates significant flight angle changes and instability, while a low SD suggests consistent and stable flight. The findings are detailed below.

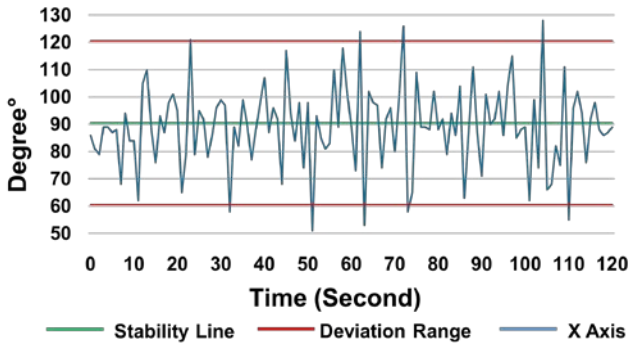

(a)

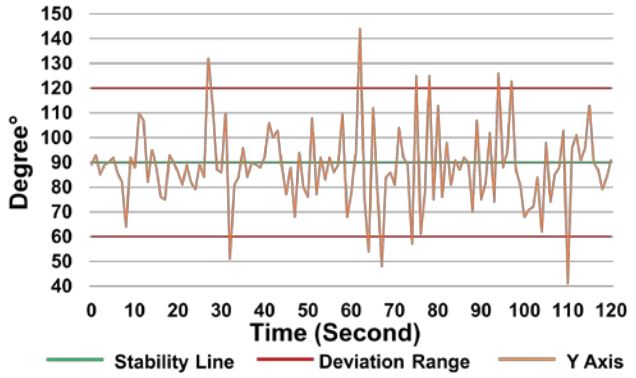

(b)

Figure 9 Drone stability tests results propeller 2-blade: (a) X Axis, (b) Y Axis.

Figure 9 provides a detailed analysis of the drone's flight stability equipped with two propellers. The graphs illustrate the drone's angular deviation from its stable hovering position, with the stability line (green line) as a reference. The results reveal that when using propellers 2-blade, the drone exhibited angular deviations exceeding the allowable limit of ±30 degrees (red line) along the X-axis on 9 occasions. Furthermore, in the Y-axis, deviations beyond ±30 degrees occurred 11 times. The calculation for evaluating flight performance shows that the SD for the 2-blade drone on the X-axis is 15.08, and on the Y-axis, it is 16.3.

Figure 10 presents the flight stability results for the drone fitted with 3-blade propellers. The data reveals that the drone surpassed the allowed angular deviation of ±30 degrees (red line) along the X-axis on 4 occasions. Similarly, 5 instances of deviation beyond 30 degrees were observed along the Y-axis. The calculation for evaluating flight performance shows that the SD for the 3-blade drone on the X-axis is 10.85, and on the Y-axis, it is 11.85.

Flight stability results for drones with 6-blade propellers are shown in Figure 11. The data thus shows that the drone exceeded the permitted roll angle ($-30 \leq \theta \leq 30$) (red line) along the X-axis in 7 cases. Also, a complete deviation was made over ±30 degrees nine times for the Y-axis. The calculation of the flight performance values shows that for the X-axis, a 6-blade drone has an SD of 12.71 and for the Y-axis it is 15.57.

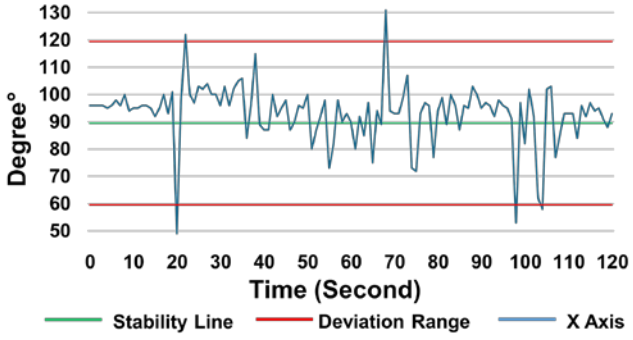

(a)

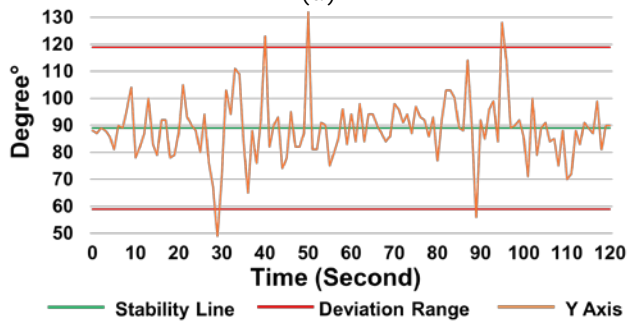

(b)

Figure 10 Drone stability tests results propeller 3-blade: (a) X Axis, (b) Y Axis.

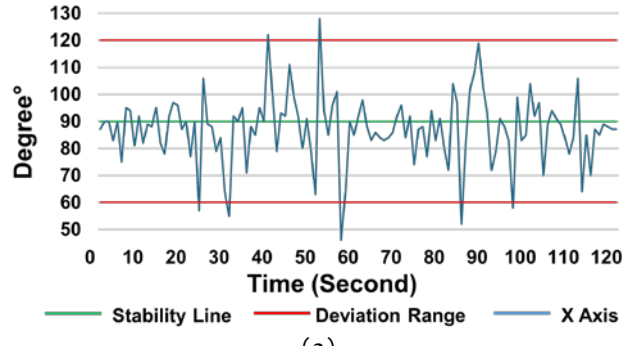

(a)

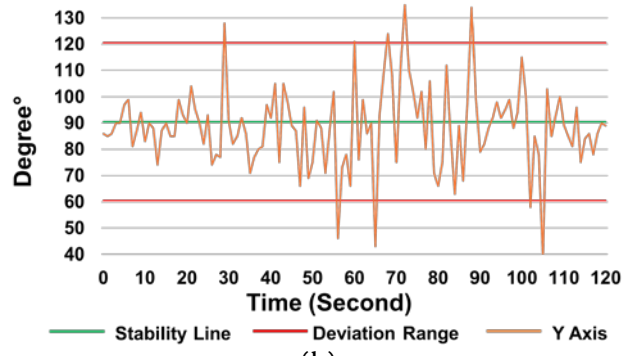

(b)

Figure 11 Drone stability tests results propeller 6-blade: (a) X Axis, (b) Y Axis.

B. Comparison of stability for three types of propellers

This study compared 2-blade, 3-blade, and 6-blade drone propellers in their flight stability.

DOI: 10.60101/jarst.2024.258251

Stability was measured according to angular deviations (X and Y axes) and standard deviations (SD) of flight variances. The results show markedly different flight stabilities among propeller types, as shown in the following sections.

2-Blade Propellers: Drones with 2-bladed propellers registered the most significant angular deviations during testing. More precisely, 9 times X > ±30 deg and also Y > ±30 deg 11 times. Figure 9 shows many points that deviated from the stability line (green line) while remaining within ±30 degrees. The constant shifts of the axis indicate a lot of movement slop when you're flying these 2-blade propeller planes. The calculated SD values for the X and Y axes were 15.08 and 16.3, indicating many disturbance signals causing the flight performance to drop below that of other propellers by as much as 58% (in one scenario).

3-Blade Propellers: Drones with a 3-blade propeller showed the lowest angular deviations. Only 4 deviated significantly more than ±30 degrees along the X-axis and 5 along the Y. The graph in Figure 10 also has less departure from the stability line (green line), which means the balance is significantly better. This resulted in X-axis and Y-axis SD values that were more than a third of those for 2 blades: 10.85 and 11.85, respectively, meaning a generally much stabler flight with less deviation between any two flights.

6-Blade Propellers: The 6-bladed propeller drones exhibited fewer angular deviations versus the 2-blade ones but more than how the 3-blade ones acted. The X-axis saw 7 anomalies of at least ±30 degrees, and the Y-axis saw 9. As seen in Figure 11(a), the green line indicates the stability line, and during deviations away from this point, although normalized to ± 30 degrees was achieved a few times, the flight tended to stabilize towards that. Although it can be seen from Figure 11(b) that deviations from the stability line along Y are more common, they are still over ±30 degrees. For the X and Y axes, one could respectively only expect a standard deviation (SD) as low as 12.71 and 15.57 in comparison with 3 blades, which would mean this stability is superior to using a 2-blade propeller but not ideal yet.

The results showed that 3-blade propellers had the greatest stability, deviated less, and had lower SD values than other types. The flight deviations and oscillations were not severe; thus, they allowed effective and stable control during the recovery phase. In comparison, 2-blade propellers exhibited the most significant instability (the highest SD values) and wandered into ranges beyond ±30 degrees. 6-blade propellers showed more minor variations than 2-blade propellers, although still more significant than 3-blade propellers.

CONCLUSIONS

This study represent how propeller configurations affect UAVs during flight. The research shows that the number of propellers plays a crucial role in drone flight performance, with more propellers having a greater impact. The 3-blade propeller has lower standard deviation (SD) values, indicating greater stability and improved accuracy in drone flights. The 2-blade propeller show high instability and significant SD values (the variable most responsible for the instability in general); such as variability linked to unstable flight conditions. Although the 6-blade propeller has lower take-off deflection than the 2-blade propeller, its flight stability is still less than the 3-blade propeller. The results show the 3-blade propeller had the best stability, followed by the 6-blade propeller, which produced a better result than 2-blade propeller configurations. The results are useful in designing a high-stability UAV for applications like aerial photography or infrastructure inspection, improving control and accuracy. However, this study has several limitations, such as the weight constraints of the prototype drone and the specific motor and battery configurations, which may influence results. Future research should investigate the impact of propeller layouts on energy efficiency and performance under varying payloads and motor speeds, thereby broadening the applicability of this research to diverse industrial and agricultural UAV designs.

ACKNOWLEDGEMENT

I would like to thank Mr. Gittiwat Thananta for his guidance on electrical systems and drone design, Mr. Kusonsang Duangpakdee for his expertise in experimental design.

REFERENCES

1. Azar AT, Koubaa A, Ali Mohamed N, Ibrahim HA, Ibrahim ZF, Kazim M, et al. Drone deep reinforcement learning: A review. Electronics. 2021;10(9):999.
2. Nwaogu JM, Yang Y, Chan AP, Chi HL. Application of drones in the architecture, engineering, and construction (AEC) industry. Automat Constr. 2023; 150:104827.
3. Moshref-Javadi M, Winkenbach M. Applications and research avenues for drone-based models in logistics: A classification and review. Expert Syst Appl. 2021;177:114854.
4. Maghazei O, Lewis MA, Netland TH. Emerging technologies and the use case: A multi-year study of drone adoption. J Oper Manag. 2022;68(6-7): 560-91.
5. Aabid A, Parveez B, Parveen N, Khan SA, Zayan JM, Shabbir O. Reviews on design and development of unmanned aerial vehicle (drone) for different

applications. J Mech Eng Res Dev. 2022;45(2): 53-69.

6. Mesquita GP, Rodríguez-Teijeiro JD, de Oliveira RR, Mulero-Pázmány M. Steps to build a DIY low-cost fixed-wing drone for biodiversity conservation. PLoS One. 2021;16(8):e0255559.
7. Leal VG, Silva-Neto HA, da Silva SG, Coltro WKT, Petruci JFDS. AirQuality Lab-on-a-Drone: A low-cost 3D-printed analytical IoT platform for vertical monitoring of gaseous H2S. Anal Chem. 2023;95 (38):14350-6.
8. Popișter F, Goia HȘ, Ciudin P, Dragomir D. Experimental study of a 3D printing strategy for polymer-based parts for drone equipment using bladeless technology. Polymers (Basel). 2024;16(4): 533.
9. Belen A, Tetık E, Başak H. 3D printed stacked antenna for WLAN drone communication. Sigma J Eng Nat Sci. 2023;41(3):656-64.
10. Çaşka S, Gök K, Aydın M, Özdemir I. Finite element method based structural analysis of quadcopter UAV chassis produced with 3D printer. J Sci Technol Dumlupınar Univ. 2020;(044):24-32.
11. Sofán-Germán SJ, Racero-Galaraga DA, Rhenals-Julio JD, Rentería-Peláez JL, Jiménez-López J. Evaluation of the use of polylactic acid in 3D printing for the construction of an unmanned aerial vehicle in the department of Cordoba. Ingeniería Competitividad. 2024;26(1). Available from: https://doi.org/10.25100/iyc.v26i1.13265.
12. Kondaveeti HK, Kumaravelu NK, Vanambathina SD, Mathe SE, Vappangi S. A systematic literature review on prototyping with Arduino: Applications, challenges, advantages, and limitations. Comput Sci Rev. 2021;40:100364.
13. Fauzi MFM, RAHIM MZ. The development of tethered drone station. Res Prog Mech Manuf Eng. 2022;3(1):605-13.
14. Gocheva M, Kuneva V, Gochev G. The Internet of Things in agriculture-the advantages and opportunities. Agric Sci/Agrarni Nauki. 2021;13 (30 Suppl):53-63.
15. Ismailov AS, Jo'Rayev ZB. Study of Arduino microcontroller board. Sci Educ. 2022;3(3):172-9.
16. Lakshmanan D, Saravanan P, Vadivelu P, Nivitha D, Yaswanth MS. Performance analysis of medium altitude low-cost autonomous quadcopter. IOP Conference Series: Materials Science and Engineering. 2020:764(1):012037.
17. Marqués P. Advanced UAV aerodynamics, flight stability and control: an introduction. In: Advanced UAV aerodynamics, flight stability and control: novel concepts, theory and applications. 2017. p. 1-30.
18. Chen Y, Eraslan H. Learning while setting precedents. Rand J Econ. 2020;51(4):1222-52.
19. Kim D, Lee Y, Oh S, Park Y, Choi J, Park D. Aerodynamic analysis and static stability analysis of manned/unmanned distributed propulsion aircrafts using actuator methods. J Wind Eng Ind Aerodyn. 2021;214:104648.
20. Zheng P, Tan X, Kocer BB, Yang E, Kovac M. TiltDrone: A fully-actuated tilting quadrotor platform. IEEE Robotics and Automation Letters. 2020;5(4):6845-52.

DOI: 10.60101/jarst.2024.258251

Received: October 8, 2024 | Revised: December 16, 2024 | Accepted: December 18, 2024

JOURNAL OF APPLIED RESEARCH ON SCIENCE AND TECHNOLOGY
JARST
INSTITUTE OF RESEARCH AND DEVELOPMENT
RAJAMANGALA UNIVERSITY OF TECHNOLOGY THANYABURI
ISSN ONLINE: 2773-9473
https://ph01.tci-thaijo.org/index.php/rmutt-journal

Increasing the value of jackfruit cobs as agricultural waste materials for syrup production by enzymatic hydrolysis using pectinase and cellulose

Kulthida Longern[1], Sopida Wisansakkul[2], Sunan Pansakron[3], Suchanart Thippayajan[1], Natthakan Pannarat[1], Piangthan Chaisingkan[1] and Orawan Oupathumpanont[1*]

[1]Department of Food and Nutrition, Faculty of Home Economics Technology, Rajamangala University of Technology Thanyaburi, Pathum Thani 12110, THAILAND
[2]Department of Home Economics, Faculty of Home Economics Technology, Rajamangala University of Technology Thanyaburi, Pathum Thani 12110, THAILAND
[3]Department of Agricultural Engineering, Faculty of Engineering, Rajamangala University of Technology Thanyaburi, Pathum Thani 12110, THAILAND
[*]Correspondence author: orawan_o@rmutt.ac.th

ABSTRACT

This research aimed to investigate the optimal working conditions for pectinase and cellulase, evaluate the quality of jackfruit cob syrup, and assess its physical and chemical properties and consumer acceptance. The study began with exploring the optimal conditions for syrup production from jackfruit cobs. The factors studied were the amount of pectinase in 3 levels: 0.04, 0.06, and 0.08%; the amount of cellulase in 2 levels: 0.1 and 0.2%; and the incubated temperature in 3 levels: 40, 45, and 50 °C; the incubated time in 3 levels: 30, 90, and 150 minutes. All 54 conditions were obtained in Factorial experiments in Completely Randomized Design (CRD). The physical and chemical properties were analyzed, and the optimal conditions were determined through hierarchical clustering, along with evaluating the physical and chemical properties and consumer acceptance. It was found that the optimum conditions for extraction of jackfruit cob juice include 0.08% pectinase, 0.2% cellulase, incubated temperature at 40 °C, and a curing time of 90 minutes, respectively. The properties of jackfruit cob syrup were as follows: brightness (L*) of 22.77 ±0.04, (a*) of -0.74 ±0.06, and (b*) of 9.16 ±0.43. The light transmittance was 1.99 ±0.01, viscosity was 14.00 ±0.05 centipoise, and pH was 4.75 ±0.10, indicating prebiotic properties. The overall liking score was 7.96. After being informed about the nutritional benefits of jackfruit cob syrup, 85.00% of consumers indicated a willingness to purchase the product. It will add value to the waste jackfruit cob in agriculture to 86 baht per kilogram. Therefore, jackfruit cob syrup is a value-added product that enhances the utilization of agricultural by-products, reduces agricultural waste, and meets consumer demand for healthy food options.

Keywords: Value added, Syrup, Jackfruit cob, Agricultural waste, Prebiotics

INTRODUCTION

Jackfruit is an important economic fruit in South and Southeast Asia. According to jackfruit planting statistics in 2020, there were 2,646,918 rai of jackfruit planting areas in Asia with a yield of 388,471.42 tons per year. Its scientific name is *Artocarpus heterophyllus*, belonging to the Moraceae family. Most consumers prefer to eat fresh jackfruit meat. It is processed at an industrial level, such as ice cream, jackfruit in syrup, canned jackfruit, dried jackfruit, crispy jackfruit, jackfruit jam, etc. As for jackfruit seeds, the utilization is still minimal. Jackfruit seeds are primarily boiled for consumption as a snack or processed into jackfruit seed flour. Steamed jackfruit bark and cob are utilized in animal feed and bio-fertilizer production. However, a significant amount of waste still remains from jackfruit consumption. Jackfruit cob then becomes waste, causing an impact on the environment, being a breeding ground for insect disease carriers, and polluting the environment, causing health problems, economic loss, and so on [1]. Jackfruit cob has a unique aroma. It has a sweetness level of 22 degrees Brix. This fruit contains important nutritional values, including carbohydrates in the form of oligosaccharides and polysaccharides. These carbohydrates function as prebiotics, supporting gut health by preventing and alleviating symptoms of gastrointestinal infections. They also strengthen the immune system, support digestion, and enhance the absorption of nutrients into the body. Additionally, jackfruit cob aids in fat metabolism and helps reduce LDL cholesterol levels. It is also rich in calcium, phosphorus, iron, vitamin B1, and vitamin B2 [2]. At present, the concept

DOI: 10.60101/jarst.2024.258413

JOURNAL OF APPLIED RESEARCH ON SCIENCE AND TECHNOLOGY

of adding value to waste after processing agricultural products is a way to increase income for farmers and various entrepreneurs in the agribusiness system [3]. It is also a guideline for developing and promoting environmentally friendly agriculture by promoting the use of agricultural waste to be processed into other products in order to add value to agricultural products.

Fruit syrup is a product processed from fruit. It is a food preservation method that uses high-concentration sugar mixed with fruit juice. The syrup is liquid with high viscosity. The color of the syrup may look cloudy or clear, and it may smell of fruit. Syrup is used in food products, beverages, desserts, milk, and ice cream, as a sweetener, flavoring agent, and decorating food products to attract consumers [4]. Therefore, syrup is a primary source of drinks, milk, food, and snacks. Currently, syrup demand in Asia is distributed as follows: 52% for the food industry, 19% for the chemical and pharmaceutical industry, 2% for import packaging and distribution, and 27% for other purposes. The import in the food industry is 52 percent, which is worth about 2,106 million US dollars or about 66,469 million baht, which is the result of the world's population increasing to 7.7 billion people in 2019 from 6.1 billion people in 2000 and the demand for syrup from other industries (food and beverages) increases.[5] Food syrup is a sweetener that is safer for health than sugar, which is high in antioxidants and helps slow down aging. It also reduces the risk of serious diseases such as diabetes, heart disease, cancer, and atherosclerosis, as well as various brain-related diseases. It also helps digestion, reduces gas in the stomach, flatulence, and constipation, and helps to strengthen the body's immunity [6].

Therefore, this research aims to explore the syrup production process to enhance the value of agricultural products, reduce agricultural waste, and meet consumer demand for healthy food options.

MATERIALS AND METHODS

1. Raw material preparation

Ripe jackfruit cobs with a yellow color and fragrant aroma are used to prepare jackfruit cob juice. The cobs are first separated from the jackfruit skins, and any bruised cobs are removed. Then the good ones will be washed thoroughly with clean water. The jackfruit cobs are inhibited for the browning reaction with boiling steam at atmospheric pressure for 10 minutes and then quickly cooled. The jackfruit cobs are centrifuged with the pulper and finisher for fruit juice extraction and separation at a speed of 200 rpm and the spin time is 5 minutes. The quality is analyzed, including pH value using a pH meter, the percentage of light transmittance of 650 nm., the content of dissolved solids using a refractometer, and the percentage of yield (% Yield).

2. Study of optimum working conditions of pectinase and cellulase

The optimal conditions for pectinase and cellulase were studied. There were 4 factors studied: the amount of pectinase at 3 levels: 0.04, 0.06, and 0.08 [7,8]; the amount of cellulase at 2 levels: 0.1% and 0.2% [9]; the incubated temperature at 40, 45, and 50 degree Celsius [7,10,11] ; and the incubated time at 3 levels: 30, 90, and 150 minutes [12,10]. The experiment was planned using factorial in CRD. A total of 54 production conditions were obtained. The prepared jackfruit cobs were digested with pectinase and cellulase according to the specified conditions, and then the enzyme reaction was stopped by immersing them in boiling water for 10 minutes and cooling rapidly. The extracted jackfruit cob juice was processed in a centrifuge separator at 2,000 rpm for 20 minutes. The crystal was separated and analyzed for quality as follows:

2.1 The physical properties include the yield percentage (% Yield), which is determined by precipitating jackfruit cob juice using pectinase and cellulase. The yield is calculated according to Equation 1.

$$\text{Percentage of yield (\% Yield)} = \frac{\text{Weight of extracted jackfruit cob juice}}{\text{Weight of initial jackfruit cob}} \times 100 \qquad (1)$$

2.2 Find color value using Hunter Lab and light transmittance using UV/VIS Spectrophotometer of 650 nm.

2.3 Chemical properties include pH value measured using a pH Meter and soluble solids measured using a Hand Refractometer. Afterward, suitable experimental subjects were selected by considering physical properties such as brightness and light transmittance using Hierarchical Clustering and the maximum light transmittance for producing jackfruit cob syrup.

3. Study on the quality of jackfruit cob syrup

Concentrate the jackfruit cob juice from the group with the highest brightness value and light transmittance using vacuum evaporation 1 atm at 60 °C until it reaches 65 degrees Brix. Then, analyze its quality as follows:

3.1 Physical properties include %yield, color value measured by Hunter Lab, light transmittance measured by UV/VIS Spectrophotometer, and viscosity measured by Brookfield Digital Viscometer.

3.2 Chemical properties include pH value measured by using a pH meter.

3.3 Consumer preferences were studied by planning a randomized complete block design (RCBD)

DOI: 10.60101/jarst.2024.258413

JOURNAL OF APPLIED RESEARCH ON SCIENCE AND TECHNOLOGY

with a 9-point Hedonic Scale method for appearance, color, clarity, jackfruit smell, flavor, and overall preference. The sample comprised 100 consumers aged 20 years and over in Rajamangala University of Technology Thanyaburi, Pathum Thani Province.

4. Study on physical and chemical qualities and consumer acceptance of jackfruit cob syrup

4.1 The physical properties include color values measured using a Hunter Lab colorimeter, light transmittance measured with a UV/VIS spectrophotometer, and viscosity measured using a Brookfield Viscometer (Model DV1) from AMETEK.

4.2 Chemical qualities include pH value measured by using a pH Meter.

4.3 For prebiotic properties, prepare 1 ml of jackfruit syrup and add 9 ml of 0.85% sodium chloride (NaCl) solution. Shake to obtain a dilution level of 10^{-1}. Dilute the sample from 10^{-2} - 10^{-6} or according to appropriateness by pipetting 1 mL of prepared sample (10^{-1}) into 9 mL of 0.85% NaCl solution, shaking well. Pipette 0.1 mL of each dilution onto Lactobacillus MRS agar. Spread the samples over two Petri dishes with a glass rod. The Petri dishes are incubated at 35 degrees Celsius for 24 hours. If no colonies are observed, incubation is extended for an additional 24 hours. Colonies are counted on dishes with a colony range of 25 to 250.

4.4 A study of consumer acceptance towards jackfruit cob syrup was done by using a 9-Point Hedonic Scale (a score of 1 means dislike the most and 9 means like the most). In terms of appearance, color, clarity, viscosity, jackfruit smell, sweet taste, jackfruit flavor, and overall preference by testing with 100 consumers aged 20 years and over in the area of Rajamangala University of Technology Thanyaburi, Pathum Thani Province.

RESULTS AND DISCUSSION

1. Raw material preparation

According to raw material preparation, it was found that the jackfruit cob that was used to separate the pulp jackfruit cob juice looked turbid with some pulp and fiber, the light transmittance percentage (Transmittance 650) was 0.1, pH was 3.60, percentage of yield (% yield) was 21.3, and had sweetness of 20 degrees Brix. The sweetness of jackfruit flesh is 20 - 23 degrees Brix [7].

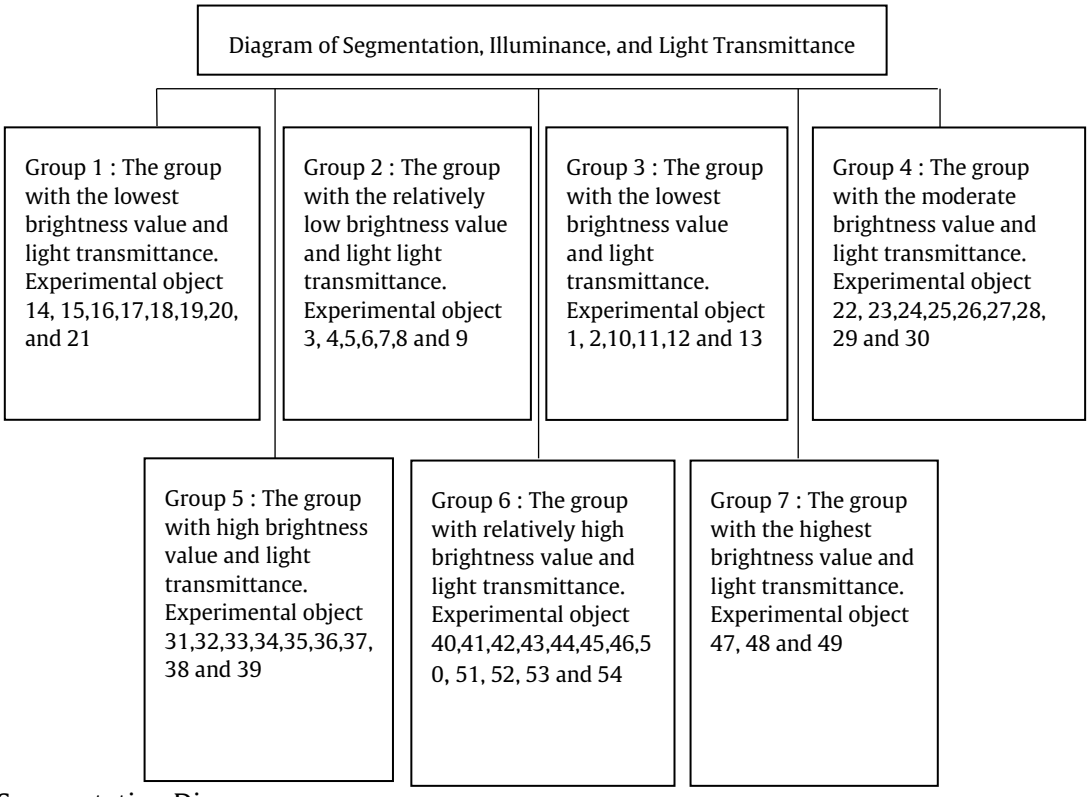

Figure 1 Segmentation Diagram.

2. Study of optimum working conditions for pectinase and cellulase

Study of optimum working conditions for pectinase and cellulase on quality of jackfruit cob juice. After the jackfruit cob juice is treated with pectinase and cellulase under 54 different conditions, the enzyme reaction is halted by immersing the mixture in boiling water for 10 minutes, followed by rapid cooling. After that, the jackfruit cob juice was extracted in the pulper and finisher for fruit juice extraction and separation (2,000 rpm) for 20 minutes, separated, and analyzed for quality. It was found that the percentage of yield

DOI: 10.60101/jarst.2024.258413

JOURNAL OF APPLIED RESEARCH ON SCIENCE AND TECHNOLOGY

(% yield) was between 39.00 - 41.00. The luminosity (L*) was between 32.65 - 33.80. The light transmittance was between 1.12 -1.15. The pH was between 3.60-3.75. The soluble solid was between 19-21 degrees Brix. The appropriate experimental group was then analyzed and selected based on the study of physical properties, including brightness and light transmittance. The obtained data were analyzed and grouped according to their abilities to select the optimum condition for producing syrup from jackfruit cob using Hierarchical Clustering, in which targets in the same group are similar in 2 factors or variables, including brightness and light transmittance for use in the next step of the study as shown in Figure 1.

According to Figure 1, the segmentation diagram using Hierarchical Clustering, it was found that the brightness values and the light transmittance values can be divided into 7 groups. The group that the researcher was interested in was group 7, with the highest brightness value and light transmittance in 3 conditions: 47,48 and 49, which have brightness values of 32.63, 32.62, and 33.81, respectively, and the light transmittance values are 1.13, 1.13, and 1.13, respectively. Brightness and light transmittance are caused by pectinase breaking down pectin compounds. Pectic acid causes plant cells to break down, leading to pectin degradation in the fruit. This process allows colloidal protein molecules and pectin to form large complexes that precipitate, thereby increasing the clarity of the fruit juice. Additionally, cellulase digests cellulose or the fruit's cell wall, breaking it down until sugars dissolve in water and are absorbed into the cell interior as a carbon source, which enhances juice extraction. As a result, jackfruit cob juice exhibits favorable physical properties [12]. Using 0.08% pectinase and 0.2% cellulase breaks down pectin in the cell wall and middle lamella, releasing more water and decreasing viscosity. This is consistent with the research of [13], which found that the concentration of pectinase and curing time can increase the yield of strawberry juice was statistically significant ($p \leq 0.05$). This aligns with the findings of [7], which reported that increasing the ratio of pectinase to ground jackfruit pulp during the production of jackfruit syrup led to a higher syrup yield. Statistical analysis revealed that when the pectinase ratio exceeded 0.06% (v/w), a significant increase in the volume of jackfruit syrup was observed ($p \leq 0.05$). Consequently, a pectinase concentration of 0.08% (v/w) was selected for treatments 47, 48, and 49 [14] . Additionally, the combined use of pectinase and cellulase facilitates the breakdown of fruit cell walls, enhancing juice extraction and improving the physical properties of the fruit juice. The study found that the curing temperature is higher when the amount of pectinase and cellulase increases and the duration is extended. Thus, there is a positive effect on the physical properties of the syrup, which pectinase serves to decompose pectin in fruit pulp, resulting in higher juice clarity and extraction [15], and cellulase-degrading enzymes that catalyze the degradation of beta 1,4 bonds, glycosidic within the molecular structure of the smallest unit of cellulose to be decomposed entirely to obtain glucose and extract clearer fruit juice [7], so brightness and light transmittance or clarity is higher. Thus, Group 7 was selected because of the highest brightness value and light transmittance values in 3 conditions.

3. Production of syrup from jackfruit cob

The conditions in group 7 were selected to produce jackfruit cob syrup by using vacuum evaporation at a temperature of 60 degrees Celsius until the sweetness is 65 degrees Brix, and analyzing the physical properties, including color value, light transmittance, viscosity, and chemical qualities (pH). The results are shown in Table 1.

Table1 Physical quality and Chemical of syrup from jackfruit cob.

Quality	Condition 47	Condition 48	Condition 49
Physical quality			
Color value (L*)	22.77a ±0.04	20.27c ±0.05	20.59b ±0.04
a*	-0.74b ±0.06	-0.96c ±0.06	-0.07a ±0.06
b*	9.16b ±0.43	7.46c ±0.43	9.90a ±0.43
Transmission (%T650)	1.99a ±0.01	1.90b ±0.01	1.87c ±0.02
Viscousity (cP)	14.00c ±0.05	16.00b ±0.01	17.50a ±0.15
Transmission (%T650)	22.77a ±0.04	20.27c ±0.05	20.59b ±0.04
Chemical quality			
Acid - base (pH)	4.75a ±0.10	4.48b ±0.12	4.29c ±0.11

Remark: Different letters in vertical is difference at 95% ($p \leq 0.05$)
^{ns} No statistically significant differences ($p \geq 0.05$)
^{a,b,c} Average in vertical which have alphabets control statistically significant ($p \leq 0.05$)
± Standard deviation.
Condition 47: Pectinase 0.08 Cellulose 0.2 temperature used for the curing 40 °C about 90 minutes.
Condition 48: Pectinase 0.08 Cellulose 0.2 temperature used for the curing 40 °C about 150 minutes.
Condition 49: Pectinase 0.08 Cellulose 0.2 temperature used for the curing 45 °C about 30 minutes.

DOI: 10.60101/jarst.2024.258413

JOURNAL OF APPLIED RESEARCH ON SCIENCE AND TECHNOLOGY

According to Table 1, the color brightness (L*) of jackfruit cob syrup was analyzed, and it was found that condition 47, which used 0.08% pectinase and 0.2% cellulase, treated at 40°C for 90 minutes, produced the best results. The color brightness (L*) was significantly the highest ($p \leq 0.05$). The brightness (L*) of jackfruit cob syrup was lower than that of jackfruit juice treated with pectinase and cellulase. This reduction in brightness is attributed to the evaporation temperature, which promotes the Maillard reaction between carbohydrates and amino acids. This reaction is a key chemical process responsible for the distinctive taste, aroma, and color observed in many processed foods. By changing the color of food, the carbonyl group of the sugar reacts with the amino group of the amino acid to form glycosylamine (N-substituted Glycosylamine) and water. Unstable glycosylamine then rearranges through Amadori Rearrangement and forms into Amadori compounds, which such compounds can react in many ways. This leads to the formation of compounds that give the melanoidins, which make the syrup browner [16] This is consistent with [12] research, which found that high temperature with longer curing time results in more browning of the syrup and lower brightness due to high temperature and longer time which cause a color change. This forms a brown compound, a Maillard reaction and is in the red to green (a*) region. The negative value indicated that the jackfruit cob syrup was greener than reddish. Therefore, it gives a yellowish appearance to jackfruit cob syrup. The pigment called Flavonol is found in yellow fruits and vegetables [14].

According to the percentage of light transmittance of syrup from jackfruit cob, it was found that condition 47 used 0.08% of pectinase and 0.2% of cellulase, cured at 40 degrees Celsius for 90 minutes significantly ($p \leq 0.05$). The percentage of light transmittance of syrup from jackfruit cob was higher than that of jackfruit juice precipitated with pectinase and cellulase because the curing time affects the clarity or light transmittance. The curing temperature and time affected the extracted dissolved solids content and clarity or light transmittance [13].

According to the viscosity (cP) of jackfruit cob syrup in Table 1, it was found that condition 47 used 0.08% pectinase and 0.2% cellulase, cured at 40 degrees Celsius for 90 minutes, significantly lowest viscosity ($p \leq 0.05$) due to pectinase curing time, and cellulase liquefaction that is almost complete, i.e., the pectinase that decomposes the pectin in the fruit into smaller molecules dissolves into the liquid part. It works when plant cells are torn or affected [8], and cellulase acts to catalyze the degradation of beta 1,4 bonds Glycosidic acid within the molecular structure of cellulose is the smallest unit [8], thus resulting in a low viscosity of jackfruit cob syrup.

According to the pH values of the jackfruit cob syrup shown in Table 1, it was found that under condition 47, where 0.08% pectinase and 0.2% cellulase were incubated at 40°C for 90 minutes, the highest pH value was 4.75 ($p \leq 0.05$), which is classified as a low pH value. The pH values ranged from 4.73 to 4.80, categorizing the syrup as a low-acid food. However, during production, the process involves heat treatment to destroy or inhibit the growth of spoilage-causing and pathogenic microorganisms, ensuring preservation and an extended shelf life [17].

4. Study of consumer preference towards syrup from jackfruit cob

Consumer preferences were evaluated using a 9-point hedonic scale with a sample of 100 consumers. The assessment covered appearance, color, clarity, jackfruit aroma, flavor, and overall preference. The results are presented in Table 2.

According to Table 2, it was found that the syrup from jackfruit cob from all 3 conditions had significantly different scores of consumer preference ($p<0.05$) in terms of appearance, color, clarity, jackfruit smell, jackfruit flavor, and overall preference. The jackfruit syrup from condition 47 got the highest score in terms of appearance, color, clarity, jackfruit smell, flavor, and overall preference because the syrup from the jackfruit cob is clear. The clarity or brightness of the syrup product is affected by the Maillard reaction. It depends on temperature, time, and pH value. In general, high temperatures and long periods increase the Maillard reaction.

Table 2 Physical quality and Chemical of syrup from jackfruit cob.

Sensory products (Character)	Condition 47	Condition 48	Condition 49
Apperance	7.23a ±1.18	6.72b ±1.06	6.48b ±1.34
Color	7.32a ±1.14	6.81b ±1.06	6.84b ±1.35
Transparency	7.24a ±1.01	6.82b ±1.07	6.89b ±1.29
Jackfruit smell	7.16a ±1.53	6.65b ±1.42	6.47b ±1.70
Jackfruit flavor	7.31a ±1.38	6.68b ±1.35	6.62b ±1.40
Overall preference	7.43a ±1.01	6.78b ±1.01	6.65b ±1.23

Remark: Condition 47: Pectinase 0.08 Cellulose 0.2 temperature used for the curing 40 °C about 90 minutes.
Condition 48: Pectinase 0.08 Cellulose 0.2 temperature used for the curing 40 °C about 150 minutes.
Condition 49: Pectinase 0.08 Cellulose 0.2 temperature used for the curing 45 °C about 30 minutes.

DOI: 10.60101/jarst.2024.258413

5. Study on the physical qualities of jackfruit syrup products

The study on the physical properties of jackfruit syrup products includes % yield, color value, light transmittance, and viscosity, while the chemical properties include pH and prebiotic characteristics. The experimental results are presented in Table 3.

Table 3 Physical quality Chemical and Prebiotic of jackfruit cob syrup.

Quantity	Quantity
Physical quality	
%yield	12.00
Brightness (L*)	22.77
Transmission (%T650)	1.99
Viscousity (cP)	14.00
Chemical quality	
Acid - Base (pH)	4.75
Prebiotic microorganism quality (CFU/g)	
Jackfruit syrup	$3.8x10^6$

According to Table 3, the physical qualities were analyzed and found to include a %yield of 12.00, color lightness (L*) of 22.77, light transmittance of 1.99, and viscosity (cP) of 14.00 when using 0.08% pectinase and 0.2% cellulase, treated at 40°C for 90 minutes. The results showed that the curing temperature significantly affected brightness, temperature, and curing time, influencing the extracted dissolved solids and the clarity or light transmittance. [14]. There is a pigment called flavonol found in yellow fruits and vegetables. The chemical qualities, including pH value, was 4.75, which has a weak acidity value. It was found that a pH range of 4.73 to 4.80 does not classify the product as a high-risk food for microbial growth, which could cause spoilage or support pathogenic microorganisms. This pH range contributes to food preservation and extends shelf life [10].

According to the prebiotic properties analysis of jackfruit cob syrup products by studying the syrup from jackfruit cobs used as food for microorganisms, Lactobacillus sp., which is a probiotic microorganism [19]. According to Table 4, it was found that syrup from jackfruit cobs contained the amount of Lactobacillus sp., which equals 3.8×10^6 colonies per gram. It is considered to have prebiotic properties. Generally, the optimal amount of probiotic bacteria in a product is at least 10^6-10^7 colonies per gram. This showed that it was not a prebiotic [18] that could affect the microbial balance within the gastrointestinal tract and inhibit the growth of pathogenic microorganisms (Pathogens) in the gastrointestinal tract that cause food diarrhea. Prebiotics are not digested or absorbed in the gastrointestinal tract. It is a nutrient that stimulates the growth of specific probiotics and can change the ratio of microorganisms to make good health [19]. Therefore, syrup from jackfruit cobs is classified as a prebiotic food.

6. Study of consumer acceptance of syrup from jackfruit cob

A study of consumer preferences towards the product used 9-point Hedonic Scale for appearance, color, clarity, viscosity, jackfruit smell, sweet taste, jackfruit flavor, and overall preference was done by testing with 100 consumers. It was found that the consumers rated their preference in terms of appearance, color, clarity, viscosity, jackfruit smell, sweet taste, jackfruit flavor, and overall preference. The consumer acceptance level was moderate, with a mean score of 7.79 ±0.26. Approximately 85% of consumers expressed a willingness to purchase jackfruit cob syrup due to its distinctive characteristic - the unique flavor of jackfruit. Additionally, its nutritional value was a key factor influencing purchase decisions, as modern consumers are increasingly focused on health and well-being, including physical, emotional, and mental health. Moreover, the production of jackfruit cob syrup supports the agricultural sector by adding value to agricultural by-products [20].

7. Study of production cost of jackfruit cob syrup

According to the study of the cost of producing jackfruit cob syrup by calculating the cost of producing jackfruit cob syrup consisting of direct raw materials, the overhead cost is 35% of the raw material price. It was found that 1 liter of jackfruit cob syrup costs 170.17 baht. If a profit of 50% of the cost price is added, the selling price per liter of jackfruit cob is 255.26 baht, which is cheaper compared to commercial products. Which is cheaper than commercial products, with 1 liter priced at 650-690 baht. Since the syrup from the jackfruit cob use raw materials that are waste, the cost of production is low, adding value to the product. In addition, jackfruit cob syrup retains its unique aroma, sweetness, and nutritional value, including protein, carbohydrates, calcium, phosphorus, iron, vitamin B1, and vitamin B2 [2]. It is considered an alternative that creates economic value that will benefit the agricultural industry more.

CONCLUSIONS

According to the study of the optimum conditions for the production of syrup from jackfruit cob, it was found that extraction requires 0.08% of pectinase, 0.2% of cellulase, curing temperature of 40 degrees Celsius, and curing time of 90 minutes. Physical qualities include the lightness of the product. The mean was 22.77 ±0.04 percent of the light transmittance of the product. The average value was 1.99 ±0.01. The viscosity of the product had an average value of 14.00 ±0.05 centipoise. The chemical properties included a pH value of 4.75 ±0.10. Consumers rated their overall preference

DOI: 10.60101/jarst.2024.258413

with an average score of 7.96 ±0.62. The respondents received information about the benefits of the syrup products from jackfruit cobs, they would definitely buy jackfruit syrup, accounting for 85.00 percent, with the most buying reason due to novelty, accounting for 29.00 percent, and the cost of producing 1 liter of jackfruit cob syrup was 170.17 baht.

ACKNOWLEDGEMENT

Thank you, Faculty of Home Economics Technology, Faculty of Science and Technology, and Faculty of Engineering, Rajamangala University of Technology Thanyaburi, as well as Talaad Thai Market for supporting.

REFERENCES

1. Charawae A. Development of edible film from Kluai Nam Wa Masa (ABB group) [Master's thesis]. Bangkok: Kasetsart University; 2007. Available from: https://doi.nrct.go.th/ListDoi/listDetail?Resolve_DOI=10.14457/KU.the.2007.122.
2. Mongphimai K. Development of food wrapping sheets from jackfruit fiber [Master's thesis]. Pathum Thani: Rajamangala University of Technology Thanyaburi; 2012.
3. Wongarun W. Added value of household waste jackfruit seeds. WMS J Manag. 2018;7(2):43-53. Available from: https://so06.tci-thaijo.org/index.php/wms/article/view/135681.
4. Chaiyo M. Qualitative comparison of banana syrup from refined sugar and non-refined sugar [Master's thesis]. Nakhon Nayok: Srinakharinwirot University; 2011.
5. ICT Center, Office of the Permanent Secretary, Ministry of Commerce, in collaboration with the Customs Department. Statistics report [Internet]. n.d. Available from: http://www.customs.go.th/list_strc_link.php?ini_content=statistics_report&iang=th&left_menu=nmenu_esevice_007.
6. Phukasmart U. Sugar and the importance of sweeteners. Food J. 2013;43(1):33-9.
7. Thaiphanit S. Enzymatic processing and spray drying of jackfruit (Artocarpus heterophyllus Lamk.) syrup powder. J Food Technol. 2012;7(1):19-23. Available from: https://li01.tci-thaijo.org/index.php/JFTSU/article/view/38361.
8. Warawit W. Probiotic and prebiotics. J Clin. 2008;27(2):19-23. Available from:https://www.doctor.or.th/clinic/detail/6931.
9. Damkham C, Chomnawung M. Do you know prebiotics yet. J Food. 2005;5(2):96-101. Available from: https://kukrdb.lib.ku.ac.th/journal/FOOD/search_detail/result/29469.
10. Kwairakan C. Production of concentrated syrup from Leb Mu banana [Musa (AA group)] by using pectines [Master's thesis]. Bangkok: Chandrakasem Rajabhat University; 2012.
11. Prapinagsorn W, Pengnet N, Munrot D, Sanichwan N. Production of syrup from cashew apples. KKU Sci J. 2011;40(3):913-23. Available from:https://ph01.tci-thaijo.org/index.php/KKUSciJ/article/view/253291.
12. Wachirasakchai M. Development of sugar product from Muntingia calabura L. for adding value to agricultural products [Master's thesis]. Pathum Thani: Rajamangala University of Technology Thanyaburi; 2016.
13. Saenjaiban N. Selection of strawberry cultivars and suitable pectinase utilization conditions for the extraction of strawberry juice [Research report]. Chiang Mai: Chiang Mai University; 2007. Available from: https://doi.nrct.go.th/ListDoi/listDetail?Resolve_DOI=10.14457/CMU.res.2007.15.
14. Panyasawan C. Development of concentrated syrup from golden bananas by using enzymes [Master's thesis]. Bangkok: Kasetsart University; 2004.
15. Sutchane J, Hutangkul C, Kamkomkat P, Kumseewai P. Screening of cellular production from thermotolerant fungi using sugarcane bagasse hydrolysate as a substrate of ethanol by Saccharomyces cerevisiae [Master's thesis]. Maha Sarakham: Rajabhat Maha Sarakham University; 2013.
16. Katajit P. Chemical description of black. 1st ed. Bangkok: IPST Publisher; 2018. Available from: https://www.scimath.org/article-chemistry/item/8474-2018-07-18-04-06-45.
17. Pheantaveerat A, Anprung P. Effect of pectinases, cellulases and amylases on production of banana juice. J Food (Thailand). 1993;23(3):188-96. Available from: https://kukrdb.lib.ku.ac.th/journal/FOOD/search_detail/result/234442.
18. Kwairakan C. Production of concentrated syrup from Leb Mu banana [Musa (AA group)] by using pectines [Master's thesis]. Bangkok: Chandrakasem Rajabhat University; 2012.
19. Suksringam B. General microbiology. 3rd ed. Bangkok: Odeon Store Publisher; 1991.
20. Wongputtisin P. Primary prebiotic properties of ethanolic sugar extract from bean seeds. J Food Technol. 2017;13(2):11-23. Available from: https://li01.tci-thaijo.org/index.php/JFTSU/article/view/135273.

DOI: 10.60101/jarst.2024.258413

Received: October 21, 2024 | Revised: January 17, 2025 | Accepted: January 20, 2025

JOURNAL OF APPLIED RESEARCH ON SCIENCE AND TECHNOLOGY
JARST
INSTITUTE OF RESEARCH AND DEVELOPMENT
RAJAMANGALA UNIVERSITY OF TECHNOLOGY THANYABURI
ISSN ONLINE: 2773-9473
https://ph01.tci-thaijo.org/index.php/rmutt-journal

Exploring the design and construction techniques of post-tensioned slabs

Thanadet Sriprasong[1*], Wongsa Wararuksajja[1] and Phakkhaphum Lethaisong[2]

[1]Department of Civil Engineering, Faculty of Engineering, Rajamangala University of Technology Thanyaburi, Pathumthani 12110, THAILAND

[2]Scientific Instrument and Technological Transfer Center, Faculty of Applied Science, King'Mongkut University Technology North Bangkok, Bangkok 10800, THAILAND

[*]Corresponding author: thanadet.s@en.rmutt.ac.th

ABSTRACT

This research aims to: 1. Study the post-tension concrete floor type. 2. Study the case study of the building construction process using post-tension concrete floors by studying the plans and construction steps of post-tension concrete floors from studying the manuals and documents for the construction of prestressed concrete floors, applying the knowledge gained from working and learning on-site to understand the characteristics, types, and plans of prestressed concrete floors and the construction steps of prestressed concrete floors. The results of this research provide information on the plans and steps in the construction of post-tension concrete floors, construction supervision, management to meet the specified time frame, various construction problems and solutions, and the development of knowledge and skills in construction supervision for future use. In conclusion, understanding the work process, construction process control methods, and inspection of various post-tension concrete floor constructions can increase work efficiency and reduce labor costs, time, and damage costs, such as contracting parties for breaches of contract. It was found that the advantages of the post-tension floor system are more floors at the same building height and less wind load at the same number of floors because it can improve long-term performance compared to traditional reinforced concrete and beam-slab systems. In addition, factors that affect the useful labor utilization ratio consist of 4 factors: complexity of building design, work items or work steps that make work difficult; use of appropriate tools and machinery to facilitate work and reduce labor waiting time; use of various innovations or substitute materials to help reduce time in work steps; arranging a team of workers that is appropriate for the size and type of work. These factors directly affect the ratio of useful workers. Results from this research Can be used to improve construction processes and inspection, Including selecting concrete materials to increase efficiency.

Keywords: Construction, Control, Plan, Post-tension, Process

INTRODUCTION

Post-tensioned slabs are popular in construction in countries with low-seismic zones, especially Thailand, because they are more economical than construction with traditional structures. There is no need for structural beams to support the floor. The structural floor has a small thickness, which makes it lightweight. The overall weight of the building is reduced, reducing the foundation's size and the number of piles. Fast and easy construction. Increased building space due to increased column-to-column span. The height between buildings' floors is reduced. (Get more floors at the same height) Light weight can reduce dead load by up to 20 - 30%, which results in less weight being transferred to the foundation. Reduce the size of the foundation and the number of pillars [1].

Prestressed concrete technology was first used in Thailand in 1940 to prestress beams. Concrete supports the floor of Preeda Thamrong Bridge, 64 meters long. This technology has been developed throughout the past. Initially, construction was done by foreign companies. Evolution of the development of prestressed concrete technology in the country in the period 40 years ago, by studying prestressed and tensile steel structures [2]. Currently, the construction of high-rise buildings and condominiums has used prestressed concrete floors or post-tension floors in large quantities because this construction takes a short and hassle-free time [3]. Properly studying the plans ensures that the tensioning process is executed correctly, which is critical for the floor's ability to bear loads safely. Missteps in the tensioning process can lead to cracks, excessive deflection, or even catastrophic failure [4]. Understanding the construction steps minimizes the risk of such issues. The placement of tendons must be precise, as incorrect placement can compromise the structural performance of the floor [5]. So, studying the plans ensures that the

DOI: 10.60101/jarst.2024.258701

JOURNAL OF APPLIED RESEARCH ON SCIENCE AND TECHNOLOGY

layout of the tendons follows the engineering design accurately.

The timing of when to apply the tension is critical. Applying it too early or too late can weaken the concrete. Understanding the construction schedule ensures that tensioning occurs at the optimal time. Post-tensioned concrete floors often use less concrete and steel than traditional reinforced concrete, saving costs [5]. Proper study of the plans allows for the maximum utilization of these savings by ensuring that materials are used efficiently. By understanding the precise construction steps, contractors can streamline the construction process, reducing overall project time and costs [6].

Non-compliance with standards can result in legal issues or costly repairs. Studying the plans helps avoid these potential problems. Properly constructed post-tensioned floors are highly durable and can handle large spans with minimal cracking and deflection over time [7].

Overall, a deep understanding of the plans and construction steps is vital for ensuring that post-tensioned concrete floors are safe, efficient, and durable, meeting all design and regulatory requirements.

This study seeks to understand post-tension slabs' detailed design and construction process. Following the correct construction steps enhances the long-term performance of the structure. Understanding the construction process helps plan future maintenance, ensuring that the post-tensioned system continues to perform well throughout the building's life. It will help improve construction efficiency, reduce costs, and minimize construction errors.

MATERIALS AND METHODS

1. Materials used in the construction

1.1 Finished floor slab

It is a flat-bottomed prestressed concrete with a cross-section like a board. Whether it is a mold or part of the structure, performing both duties helps bear weight. Generally, the cross-section is 35 cm. wide, 5 cm. thick, and arranged next to each other. The bottom side of the floor is smooth without plastering. Concrete pouring on top (Structural Topping) will work as a composite (Composite) with the finished floor.

1.2 Solid prestressed concrete floor slabs

Prestressed concrete floor slabs have a smooth surface, eliminating the need to plaster or install a ceiling. The long span can be used in various lengths. It's convenient and economical. This is because temporary bracing is not required in construction. Thus, saving both time and labor. (except thickness 6 cm.) They are designed to have different cross-sectional sizes and lengths. To bear the weight of the load. To replace the area for casting in place used for constructing residential buildings and condominiums. Office buildings and industrial factories.

1.3 Solid prestressed concrete floor slabs (Plank)

It is a small prefabricated concrete slab, usually 6 cm thick and 30 or 35 cm wide, used for general small buildings such as residential buildings and condominiums.

1.4 Micropile

It is a small, driven pile with a length of 1.5 meters. It has high density, strength, and durability.

1.5 Driven pile

This type of pile There are concrete piles, steel piles, and wooden piles. Most commonly use concrete piles. Because it is stronger than wooden poles and cheaper than steel poles. Concrete piles can be divided into two types: reinforced concrete and reinforced concrete.

1.5 Cement

1.5.1 Ordinary Portland cement (Type1) is suitable for general concrete work, which complies with TIS 15 cement.

1.5.2 Use the type that gives fast compressive strength (Type 3) following TIS 15. This type of cement will provide high compressive strength in the initial stages. Because it is finer than ordinary Portland cement, it is suitable for making concrete that needs to be used quickly. It can reduce curing time.

1.6 Coarse Aggregate

The stone standard used in producing prestressed precast concrete slabs generally uses 3/8-inch stone, suitable for solid concrete slabs.

1.7 Fine Aggregate

The sand standard that produces prestressed precast concrete slabs should have an FM value. Within the range 2.50-3.50.

1.8 High tensile steel wire (PC Wire)

Steel wire standards are used in the production of prestressed precast concrete slabs. It has a 4 and 5 millimeters diameter and must comply with TIS 95.

2. Tools and machinery used to install tensile floor slabs

2.1 Production platform (Bed)

The production platform for prestressed precast concrete slabs is a form used to cast concrete slab products. It is a steel rail along the length. The length of the production stand may vary according to the area of each factory. It is usually approximately 50-60 meters long to suit the time required for production.

A production platform for solid precast concrete slabs (Plank) is a form used to cast concrete slab products. It looks like a steel rail along its length. by the length and form of the general production platform It will be 0.30-0.35 meters wide and 5 centimeters thick. The length depends on the condition of each factory.

2.2 Wire Stressing Machine

A wire-pulling machine pulls high-tensile steel wire to produce precast concrete slabs. Prestressing can be used with both hollow and solid floors. There are 2 types: used to pull high-tensile steel wire and high-tensile stranded steel wire, Depending on the wire

DOI: 10.60101/jarst.2024.258701

JOURNAL OF APPLIED RESEARCH ON SCIENCE AND TECHNOLOGY

drawing cylinder. However, the solid type is used with general high tensile steel wire for prestressed precast concrete slabs and may be used in some prestressed products such as small piles, etc.

2.3 Wire wedge, wire splicing, and high tensile stranded steel wire cylinders

Used for fixing wire at the head-end of the wire mounting panel. Wire wedges used to hold high tensile steel wires are 2-3 pieces with teeth for holding the wire in a wedge wire cylinder.

2.4 Length divider set

Used for dividing the length of floor slabs to be produced. The length must be divided before concrete is poured into the form. There are 2 types: hole type, used by inserting wire into the specified holes according to the quantity produced. The wire height can be set using a comb type. Used to divide by steps between each wire. Nevertheless, we cannot set the wire height distance.

2.5 Concrete Mixing

Pan Type This mixer consists of an important part: a circular pan and a stirring blade attached to the shaft. Furthermore, it will rotate around an axis perpendicular to the Pan Mixer's axis. Some types of Pans will rotate, and some types of mixing blades will rotate. Moreover, some rotate both in opposite directions. The concrete is mixed very well. The Pan Mixer is effective for hard and highly bonded concrete, such as cement-heavy concrete. Therefore, it will be used for prestressed concrete work.

2.6 Concrete vibrating equipment

Used for firmly shaking concrete. with vibration Makes the concrete evenly dense. The surface of the workpiece is smooth. Generally, a vibrator is used. Or you can use a concrete pendant.

3. Engineering standards or regulations that are followed during the design and installation

3.1 Post-Tension Concrete Floor

Post-tension concrete floors are widely used because they are economical and can be constructed quickly [8]. This can be seen in office buildings, parking lots, hotels, shopping malls, etc., which often have long column spans. After bonding forces, the characteristics of post-tensioned concrete floor systems allow them to be designed as flat floors without beams, with long column spans, and to bear more weight than general structural floors.

3.2 Advantages of Post-Tension Concrete Floor Systems [8]

Post-tension concrete floor systems can work quickly. The construction speed is about 7-14 days per floor because it can support the weight of the structure immediately after pulling the prestressing wire and saves on labor costs, scaffolding costs, and formwork costs and reduces construction time because the building can be designed to have a longer column span than the general structure, allowing for a wider variety of usable space designs.

Post-tension concrete floor systems can be designed to have a lower structural thickness than reinforced concrete floors, which can reduce the height between building floors. This allows buildings using post-tension concrete floors to have more floors than general reinforced concrete buildings of the same building height. Because it is a prestressed concrete floor, it has the property of resisting cracking, resulting in a floor that is more watertight than general reinforced concrete floors, reducing the problem of water seepage and rusting of reinforcing steel. In addition, post-tension concrete floors can be designed to have a covering distance sufficient to resist fire according to the standards and requirements of fire-resistant materials according to Ministerial Regulation No. 40 B.E. 2540. The advantages of post-tension concrete floors in various aspects include architectural, structural, and cost-effectiveness.

3.3 Ground Characterization

Most post-tension concrete floors can be designed as flat slabs because they are easy to work with and save material costs, labor costs, and construction time. These are the advantages of post-tension concrete floors compared to general reinforced concrete floors. However, the specification of post-tension concrete floors must also consider other factors. In some cases, post-tension concrete floors require drop panels or band beams to achieve maximum savings, such as in cases where the building has a long column-to-column span, small columns, or 4 large openings. Initially, the characteristics of the post-tension concrete floor can be considered from the length (span), such as flat slab, flat slab with a column span of 6-9 m., drop panel, flat slab with a column span of 9-12 m., and band beam, a floor with a wide beam with a column span of more than 12 m.

3.4 Determination of the distance between the outer span columns and the cantilevered floor

To design post-tension concrete floors with the highest economic value, determining the distance between the edge columns and the free-floating slab that is appropriate and consistent with the spacing between the columns of the inner span will allow to reduce the amount of prestressing wire and the thickness of the post-tension concrete floors. The appropriate distance between the edge columns and the free-floating slab may be considered from the spacing between the columns of the inner span.

3.5 Determination of floor thickness

The thickness of the slab affects the amount of prestressing wire and the amount of reinforcing steel, as well as the deflection and vibration of the post-tension concrete slab. Specifying a slab thickness that is too thin may result in the slab having much prestressing wire, resulting in high and uneconomical construction costs. It may also cause the slab to be unable to withstand

DOI: 10.60101/jarst.2024.258701

JOURNAL OF APPLIED RESEARCH ON SCIENCE AND TECHNOLOGY

shear, deflection, and vibration. Consider the example table of design thickness of the post-tension concrete slab, shown in Table 1.

Table 1 Determination of floor thickness. (Source: Siam Cement Company Limited).

Section Type	Loading (LL) kg/m²	Span/depth ration 6m. <=L <=13m.	
1. Flat plate	250	40	
	500	36	
	1,000	30	
2. Flat slab with drop panel	250	44	
	500	40	
	1,000	34	
3. Flat slab with banded beam		SLAB	BEAM
	250	45	25
	500	40	22
	1,000	35	18

3.6 Lowering the ground level

Post-tension concrete floors can have different floor levels (lower floor levels) by either lowering the floor with a flat bottom or lowering the floor with a lower bottom. However, the suitable and economical floor lowering distance for post-tension concrete floors is less than 5 cm.

3.7 Determination of openings in post-tensioned concrete floors

The most suitable opening location on post-tensioned concrete floors should be in the middle of the span. The most avoidable location is the column head or support area because the column head area will have a dense line of prestressed wires. Most importantly, prestressed concrete floors are mainly designed as flat plates. This type of floor requires the concrete around the column to be important in resisting punching shear. Having openings around the column within 10 times the floor thickness (10h) will greatly reduce the punching shear capacity. According to ACI requirements, openings that are no more than 10 times the floor thickness (10h) away from the column will reduce the concrete line that acts as a punching shear force (Critical section), reducing punching shear capacity. If the punching shear capacity is insufficient, it may be necessary to add shear stirrup, increase the floor thickness, and add column capital or beam to help with the force.

3.8 Post-Tension Concrete Floor Installation Procedure

The steps for installing prestressed concrete floors (post-tension) include: 1) setting up supports and floor formwork, 2) placing lower reinforcing bars, 3) inserting PC Strand wire into the corrugated sheath, 4) attaching tendon anchors to side forms 5) placing upper reinforcing bars 6) pouring concrete 7) prestressing the concrete 8) sealing the Anchorage sockets with mortar, and 9) injecting mortar.

3.9 Aggregate and mixed sizes

The elastic modulus of cement-based materials is complex due to the non-homogeneous structure of the material. To predict the behavior of concrete under load, it is necessary to understand the effects of aggregate type, aggregate size, and aggregate volume [9]. The modulus of elasticity is directly proportional to the stiffness of each component in the concrete and the joints [10]. Most static elasticity modulus from normal axial compression only reaches a stress level of approximately 40-50% of the concrete's ultimate compressive strength, which is the level at which the stress does not occur. Small cracks at the interface between the cement and aggregates [11]. Research has shown that compaction to improve the mix ratio is a very effective way to reduce the cement content in the mix [12]. Cement production hurts the environment and improving the compaction of the aggregates can reduce the cement content and increase the elastic modulus. It helps to improve the strength by improving the hydration process in concrete [13]. And the strength of concrete is greatly influenced by the size distribution of aggregates, where the key factor in aggregate compaction is to allow small aggregates to fill the spaces between large aggregate particles by using the right mix size and proportion [14].

RESULTS AND DISCUSSION

Case study of the structural floor of an 8-storey building, a prestressed concrete floor structure. The construction of the prestressed concrete floor can be summarized in Figure 1-8:

1. Steel structure floor plan

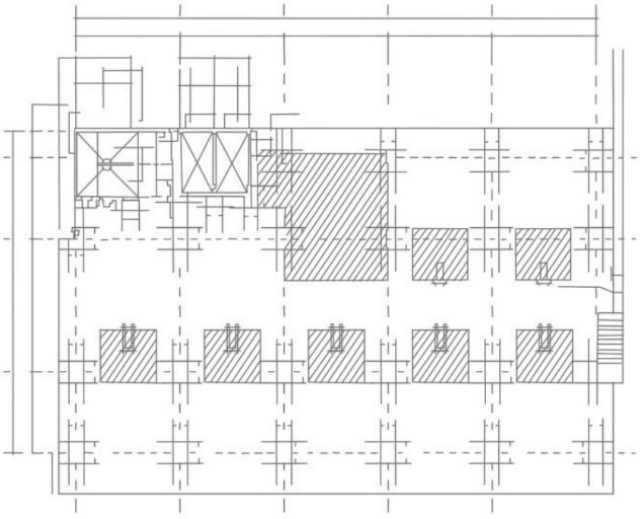

Figure 1 Steel structure floor plan [15].

DOI: 10.60101/jarst.2024.258701

JOURNAL OF APPLIED RESEARCH ON SCIENCE AND TECHNOLOGY

2. Expanded shear reinforcement type

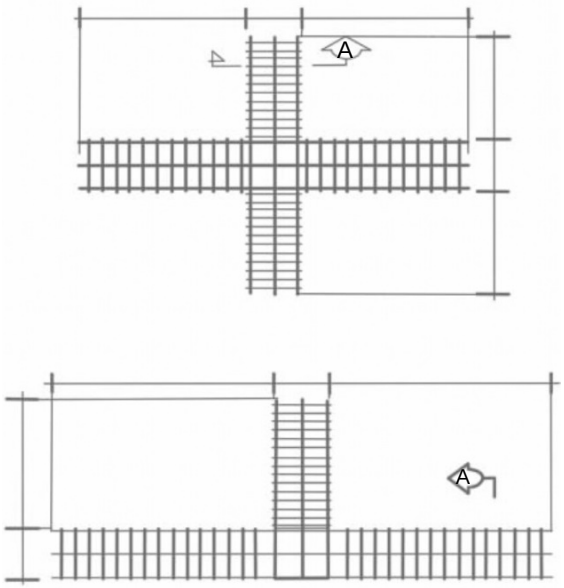

Figure 2 Example Figure [15].

3. Beam A is inside the floor.

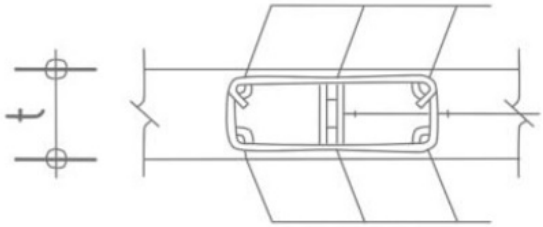

Figure 3 Beam A is inside the floor [15].

4. Shop Drawing (Prestressed Wire)

Shop Drawing (Prestressed Wire Line) shows the number of types of prestressed wire lines and the number of lines for use in laying out the wire ropes and checking before pouring concrete.

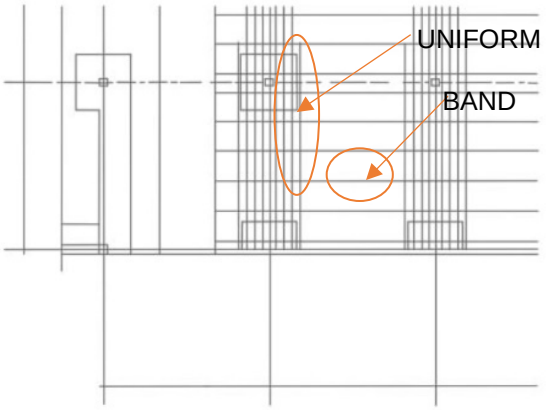

Figure 4 Shop Drawing (Prestressed Wire) [15].

5. Shop Drawing (Prestressed Wire Profile)

Shop Drawing (Prestressed Wire Profile) is a wire rope extension drawing for placing Bar Chairs because each section of the wire rope will not be placed the same in terms of the distance and height of the Bar Chair.

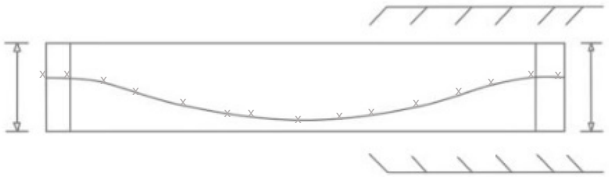

Figure 5 Shop Drawing (Prestressed Wire Profile) [15].

6. More floors at the same building height

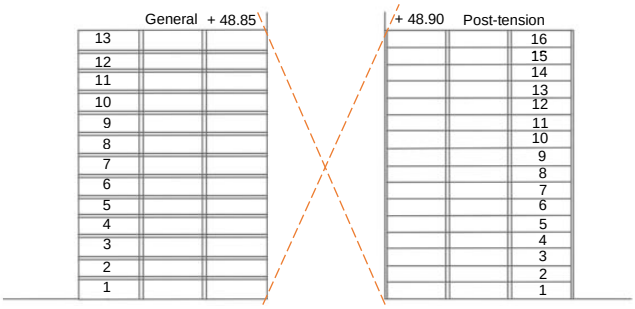

Figure 6 More floors at the same building height [15].

7. Wind Load less than the same number of floors

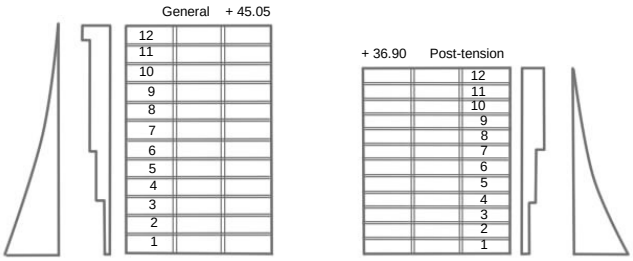

Figure 7 Wind less Load than the same number of floors [15].

8. The construction steps [15]

The construction steps of reinforced concrete floors are following the step according to figure 8.

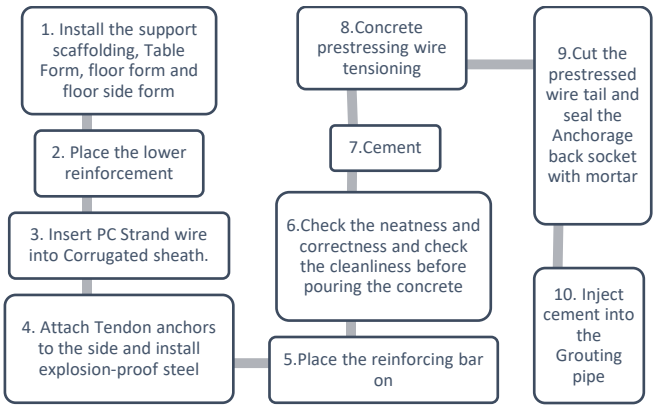

Figure 8 The construction steps of reinforced concrete floors [15].

DOI: 10.60101/jarst.2024.258701

9. Factors affecting productivity in construction work of floor work

There are 4 main factors in prestressed concrete: [15]

1. Complexity in building design, work materials, or work procedures that cause difficulty in working.

2. Use appropriate machinery to facilitate work and reduce waiting time for workers in concrete pouring work.

3. Using innovations or alternative materials to help reduce the time in the work process and reduce the difficulty of the work, such as installing steel and reinforcing steel.

4. Arranging the right team of workers for the size and type of work.

CONCLUSIONS

Understanding the work process, construction process control methods and inspection of various post-tension concrete floor constructions can increase work efficiency and reduce labor costs, time, and damage costs, such as contracting parties for breaches of contract.

Table 2 Comparison of various features of Post-Tension Slabs, Reinforced Concrete Slabs, and Beam-Slab Systems.

Feature	Post-Tension Slabs	Reinforced Concrete Slabs	Beam-Slab Systems
Strength	High, better crack control, and load distribution	Lower tensile strength, prone to cracking	High, but requires large beams
Cost	Potentially lower overall due to material savings	Generally higher due to more material needed	Higher due to additional beams and reinforcement
Slab Thickness	Thinner slabs, more space-efficient	Thicker slabs for strength	Thicker slabs with added beam depth
Construction Time	Faster due to reduced slab thickness and complexity	Slower due to thicker slabs and more reinforcement	Slower due to beam complexity
Long Span Capability	Ideal for long spans with fewer supports	Limited span capabilities without beams	Suitable for long spans but with additional material requirements
Durability and Maintenance	Low maintenance, fewer cracks, higher durability	Prone to cracking and maintenance issues	Prone to cracking, additional complexity for repairs
Flexibility and Space	More flexible use of space, open areas	Reduced ceiling height due to thickness	Reduced space flexibility due to beams

This study found that the advantages of the post-tension floor system are more floors at the same building height and less wind load at the same number of floors. Post-tension concrete slabs are a superior choice in many situations, offering cost and time savings, reduced material usage, and improved long-term performance compared to traditional reinforced concrete and beam-slab systems. PT slabs are particularly well-suited for long spans, flexible space usage, and structures that prioritize minimizing slab thickness. While PT systems require higher initial costs due to specialized equipment and materials, their efficiency in construction time, reduced labor costs, and lower long-term maintenance make them a favorable option for many building projects. This is in line with the research of Thanapat Ekphong and Kawin Tantisevi (2021), who studied the construction productivity of prestressed concrete floors in high-rise buildings. This research shows that a lump sum cost based on the weight of wire ropes is 26-37 bath-sq.m. of slabs, while a labor cost based on the number of man-days is 10-12 bath-sq.m. Hence, the difference in labor costs calculated by these two approaches is likely a profit margin for subcontractors. Moreover, the research of Narongchai Paksa and Thotsapon Pinkaew (2020) studied the development of high elastic modulus concrete for ultra-rigid structures. The results are compared with normal concrete specimens using limestone as coarse aggregate. It is found that the proposed concrete using EAF slag can significantly enhance the elastic modulus and is more cost-effective than conventional high-strength concrete.

In addition, factors that affect the useful labor utilization ratio consist of 4 factors: complexity of building design, work items or work steps that make work difficult; use of appropriate tools and machinery to facilitate work and reduce labor waiting time; use of various innovations or substitute materials to help reduce time in work steps; arranging a team of workers that is appropriate for the size and type of work. These factors directly affect the ratio of useful workers. However, if there are indirect factors that may cause an impact on the work, causing the ratio of useful workers to decrease, the researcher believes that this research can be further developed to study such impacts and to be beneficial to projects with similar characteristics in the future.

DOI: 10.60101/jarst.2024.258701

Recommendations for use and precautions of post-tension concrete floors include checking the safe load specified in the post-tension concrete floor structure before actual use. Any holes that are dug after construction is complete must be consulted with a design engineer. Renovations and changes to the building's space usage must be consulted with a design engineer. The scaffolding must not be dismantled before the prestressed wire pulling is complete. Also, the integration of new technologies into the post-tensioned concrete slab construction process has the potential to significantly improve efficiency, quality, sustainability, and safety. By embracing innovations in AI, robotics, 3D printing, AR, and advanced materials, the construction industry can develop more innovative, more resilient structures. Further research into the application of these technologies and the development of new materials and construction methods will drive the evolution of post-tensioning techniques, ensuring that they remain a cost-effective, sustainable, and adaptable solution for modern building projects.

ACKNOWLEDGEMENT

The authors would like to thank all those who contributed information and were consultants in completing this report and provided care and understanding of real working life. The authors would like to express their deepest gratitude.

REFERENCES

1. Home - We Love Steel Construction [Internet]. We Love Steel Construction - SSI Steel Construction; 2023 [cited 2024 Apr 15]. Available from: https://welovesteelconstruction.ssi-steel.com
2. Moothong N. Technology of post-tensioned prestressed concrete in Thailand, case studies of bridges and buildings. Nonthaburi: Ministry of Science and Technology.
3. Ekaphong T. Study of construction productivity of prestressed concrete floors in high-rise buildings [dissertation]. Bangkok: Department of Civil Engineering, King Mongkut's University of Technology North Bangkok.
4. Cracking of concrete [Internet]. Prince of Songkla University, Department of Civil Engineering. Available from: http://www.phigroup.co.uk/tags/concrete-panel/concretepanel.
5. Simapichet I. Comparison Study Post Tension Concrete Slab Vs Conventional Concrete Slab, Project 5-Floor Apartment in Samutsakorn Province [dissertation]. Bangkok: Department of Civil, Environmental and Sustainability Engineering, Siam University; 2018.
6. Pantharat N. Design of prestressed concrete [dissertation]. Bangkok: Faculty of Engineering, Sripathum University; 1998.
7. Kanchanalai T. Design of prestressed concrete. Bangkok: Kasetsart University Library.
8. SNP POST TENSION CO., LTD. Design of post-tension floor to withstand lateral force [Internet]. Available from: http://www.snp-precast.snp-post.com
9. Al-Baijat HM. The Use of Basalt Aggregates in Concrete Mixes in Jordan. Jordan Journal of Civil Engineering. 2008;2(1):63-70.
10. Alexander MG, Mindess S. Aggregates in Concrete. London: Taylor & Francis Cop; 2005.
11. ASTM Standard C469/C469M-14. Standard Test Method for Static Modulus of Elasticity and Poisson's Ratio of Concrete in Compression. In: Annual Book of ASTM Standards. vol. 09.49. West Conshohocken: ASTM International; 2014.
12. de Grazia MT, Sanchez LFM, Romano RCO, Pileggi RG. Investigation of the use of continuous particle packing models (PPMs) on the fresh and hardened properties of low-cement concrete (LCC) systems. Constr Build Mater. 2019;195:524-36.
13. Klein NS, Lenz LA, Mazer W. Influence of the granular skeleton packing density on the static elastic modulus of conventional concretes. Constr Build Mater. 2020;242:118086.
14. Haque MB, Tuhin, IA, Farid MSS. Effect of aggregate size distribution on concrete compressive strength. SUST journal of science and technology. 2012;19(5):35-9.
15. The prestressed concrete floor design line. Construction documents and reports of the elderly accommodation project, The Senizens. Bangkok: BCC Construction Co., Ltd. and C-Post Co., Ltd.

DOI: 10.60101/jarst.2024.258701

Received: October 15, 2024 | Revised: January 20, 2025 | Accepted: January 22, 2025

JOURNAL OF APPLIED RESEARCH ON SCIENCE AND TECHNOLOGY
JARST
INSTITUTE OF RESEARCH AND DEVELOPMENT
RAJAMANGALA UNIVERSITY OF TECHNOLOGY THANYABURI
ISSN ONLINE: 2773-9473
https://ph01.tci-thaijo.org/index.php/rmutt-journal

Behavioral analysis of two-dimensional difference equations in the third quadrant

Kanmanee Kitsasom, Laksika Promma, Aonnicha Butdee, Pongpun Julatha, Uraiwan Jittburus and Wirot Tikjha*

Faculty of Science and Technology, Pibulsongkram Rajabhat University, Phitsanulok 65000, THAILAND
*Corresponding author: wirottik@psru.ac.th

ABSTRACT

Piecewise linear systems of difference equations have gained significant attention for their ability to model complex behavior in population dynamics, economics, and electronics fields. Despite their simple structure, these systems can exhibit diverse behaviors, including convergence to equilibrium points, periodic solutions, and chaotic outcomes under specific conditions. This paper investigates the long-term behavior of a specific piecewise linear system of difference equations. The primary goal is understanding how initial conditions and parameter values influence the system's behavior. The research focuses on identifying and analyzing equilibrium points, periodic solutions (cycles), and the conditions under which these behaviors occur. Building on previous work by Grove et al., we study a family of two-dimensional difference equations containing absolute value terms. The analysis focuses on initial conditions in the third quadrant, divided into three distinct regions: A, B, and C. The behaviors within each region are explored to characterize the system's outcomes. Region A: The system converges to an equilibrium point. The number of iterations required for convergence varies depending on the sub-region. Region B: The system converges to an equilibrium point in exactly two iterations. Region C: The system exhibits more complex behaviors, with potential outcomes including convergence to a 4-cycle or an equilibrium point. Behavior in this region suggests that initial conditions may lead to one of two prime period-4 cycles. Regions A and B consistently lead to equilibrium points, while Region C displays more varied outcomes, including periodic cycles. These findings emphasize the complexity of piecewise linear systems and stress the need for further research to fully understand the behaviors in Region C.

Keywords: Piecewise linear system, Equilibrium point, Difference equations

INTRODUCTION

The study of piecewise linear systems of difference equations has garnered attention for their ability to model complex dynamics in various fields such as population dynamics [1], economics [2] and electronics [3]. Despite their simplicity, these systems exhibit a wide range of behaviors, including convergence to equilibrium points, periodic solutions, and sometimes chaotic behavior [4, 5, 6]. Researchers aim to understand the long-term behavior of these systems and how initial conditions and parameters influence their behaviors. One of the key research drivers is the open problem posed by Grove et al. [7], which introduced a family of systems defined by the general form

$$\begin{cases} x_{n+1} = |x_n| + ay_n + b \\ y_{n+1} = x_n + c|y_n| + d \end{cases} \quad (1)$$

with parameters a, b, c and d belonging to $\{-1, 0, 1\}$ and initial condition $(x_0, y_0) \in \mathbb{R}^2$.

Various studies have analyzed how different parameter values affect the system's long-term behaviors. For instance, in article [8] demonstrated that certain parameter sets could result in either a unique equilibrium or periodic behavior with a prime period of 5.

Two primary types of attractors are commonly identified: equilibrium points and periodic solutions (cycles). Equilibrium points represent stable states where the system remains unchanged after iterations. These points are of particular interest because, under certain conditions, the system always converges to this stable state, regardless of initial conditions. Researchers explore whether solutions converge to a single equilibrium or multiple equilibrium points depending on the system's parameters. Periodic solutions, or cycles, are repeating patterns where the system's state follows a cycle with a fixed prime period.

Parameters and initial conditions influence the existence and stability of these periodic solutions. Researchers have identified conditions where the system exhibits periodic behavior with various prime periods. The article [9] found that in system (1), with a = b = d = -1 and c = 1, when the initial condition is an element of the closed second or fourth quadrant, the solution to the system is either a prime period-3 solution or one of two prime period-4 solutions.

DOI: 10.60101/jarst.2024.258602

JOURNAL OF APPLIED RESEARCH ON SCIENCE AND TECHNOLOGY

One key contribution to this research is the work in [10], which studies a special case of system (1) by setting $b = c = -1$ and $d = 1$ but generalizes the parameter b into the following system:

$$\begin{cases} x_{n+1} = |x_n| - y_n - b \\ y_{n+1} = x_n - |y_n| + 1 \end{cases}, \quad (2)$$

where $b \geq 4$ and found that for $b = 4$, solutions converge to equilibrium, while for $b \geq 6$, the system exhibits periodic behavior with a prime period of 5 [11]. Their findings illustrate the importance of parameter thresholds in determining whether the system converges to an equilibrium or follows periodic behavior. In article [12], the study the system (2) by setting b = 3:

$$\begin{cases} x_{n+1} = |x_n| - y_n - 3 \\ y_{n+1} = x_n - |y_n| + 1 \end{cases}, \quad (3)$$

finding that the solutions can converge to a periodic cycle with a prime period of 4. Their investigation focuses on a specific region in the first quadrant. In [13] and [14], the behaviors of System (3) in the second quadrant were investigated, and 4-cycles and equilibrium points were identified. Building on this, we now examine System (3), considering initial conditions located in a specific region of the third quadrant.

MATERIALS AND METHODS

We divide the third quadrant into subregions and investigate each one by substituting specific initial conditions into System (3) and performing direct calculations. Moreover, in some regions, we identified patterns in the solutions, which we used to formulate inductive statements to explain the behavior of the solutions.

We applied the same methods to investigate the behavior of solutions as described in articles [12-14]. The following definitions [15], will be applied in this paper. A two-dimensional first-order system of difference equations takes the form: $x_{n+1} = f(x_n, y_n)$ and $y_{n+1} = g(x_n, y_n)$ where f and g are continuous functions mapping R^2 to R and $n \geq 0$. A solution to this system is a sequence $\{(x_n, y_n)\}_{n=0}^{\infty}$ that satisfies the system for all $n \geq 0$. If an initial condition $(x_0, y_0) \in R^2$ is given, then the subsequent solutions are determined as: $(x_1, y_1) = \big(f(x_0, y_0), g(x_0, y_0)\big), (x_2, y_2) = \big(f(x_1, y_1), g(x_1, y_1)\big), \cdots$.

A solution that remains constant for all $n \geq 0$ is referred to as an equilibrium solution. If $(x_n, y_n) = (\bar{x}, \bar{y})$ for all $n \geq 0$, it represents an equilibrium solution, and $(\bar{x}, \bar{y})$ is known as an equilibrium point of the system.

A solution $\{(x_n, y_n)\}_{n=0}^{\infty}$ is called an eventual equilibrium point if there exists an integer $N > 0$ such that for all $n \geq$ N, $(x_n, y_n) = (\bar{x}, \bar{y})$.

A solution is called eventually periodic with a period p, or an eventually period p-cycle, if there exists an integer $N > 0$ such that the solution is periodic with period p, meaning $(x_{n+p}, y_{n+p}) = (x_n, y_n)$ for all $n \geq$ N.

The set of periodic point is prime period p (or p-cycle) if p the smallest positive integer such that the set member is periodic with period p. We define a 4-cycle as the set $\{((a,b),(c,d),(e,f),(g,h))\}$, consisting of four consecutive points $(a,b), (c,d), (e,f), (g,h)$ in the xy-plane.

A solution is considered eventually periodic with period p (eventually a 4-cycle) if the orbit, through forward iterations, passes through one of the cycle's points. We define the region of the initial condition in the third quadrant as the set $Q_3 = \{(x,y) \in R^2 | x < 0 \; and \; y < 0\}$.

RESULTS AND DISCUSSION

We will examine the behaviors of System (3) when the initial condition is located in the set $A = \{(x,y) \in Q_3 | -x - y - 3 < 0 \text{ and } x + y + 1 \geq 0\}$, $B = \{(x,y) \in Q_3 | -x - y - 3 < 0 \text{ and } x + y + 1 < 0\}$ and $C = \{(x,y) \in Q_3 | -x - y - 3 \geq 0 \text{ and } x + y + 1 < 0\}$. We assert that System (3) has an equilibrium point at $(-1,-1)$, determined by solving equations $\bar{x} = -\bar{x} - \bar{y} - 3$ and $\bar{y} = \bar{x} + \bar{y} + 1$. Additionally, we identified two prime period-4 solutions (or 4-cycles): $P_{4.1} = \{((-5,-1),(3,-5),(5,-1),(3,5))\}$ and $P_{4.2} = \{((1,-1),(-1,1),(-3,-1),(1,-3))\}$ for System (3). We will start our investigation by calculating the first iteration for $(x_0, y_0) \in A$, which corresponds to the green region in Figure 1. In Figure 1, the third quadrant is separated into three sub-regions by the lines $f(x)$ and $g(x)$. The red point is the equilibrium point of the system (3). The green region represents the points in the set A. The pink region represents the points in set B. The remaining white region in the third quadrant represents the points in set C.

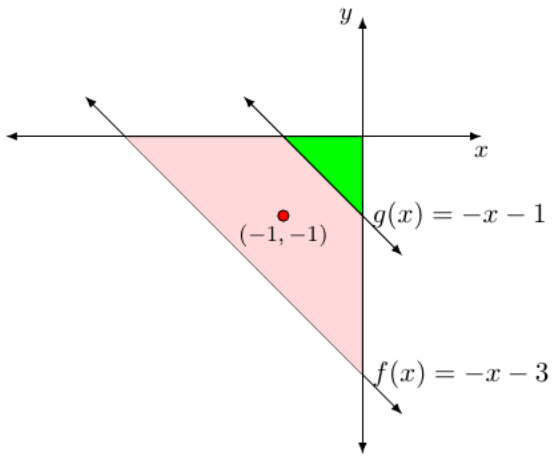

Figure 1 The third quadrant is separated into three sub-regions by the lines $f(x)$ and $g(x)$.

Thus, we obtain the following solutions:

$$\begin{cases} x_1 = |x_0| - y_0 - 3 = -x_0 - y_0 - 3 < 0 \\ y_1 = x_0 - |y_0| + 1 = x_0 + y_0 + 1 \geq 0 \end{cases} \quad (4)$$

DOI: 10.60101/jarst.2024.258602

JOURNAL OF APPLIED RESEARCH ON SCIENCE AND TECHNOLOGY

Because the initial condition $(x_0, y_0) \in A$, x_1 is negative and y_1 is non-negative.

$$\begin{cases} x_2 = |x_1| - y_1 - 3 = -1 \\ y_2 = x_1 - |y_1| + 1 = -2x_0 - 2y_0 - 3 < 0 \end{cases} \quad (5)$$

Since y_1 is non-negative, $y_2 = -2y_1 - 1 < 0$.

$$\begin{cases} x_3 = |x_2| - y_2 - 3 = 2x_0 + 2y_0 + 1 \\ y_3 = x_2 - |y_2| + 1 = -2x_0 - 2y_0 - 3 < 0 \end{cases} \quad (6)$$

If $x_3 = 2x_0 + 2y_0 + 1 \leq 0$ then the next iteration $\begin{cases} x_4 = |x_3| - y_3 - 3 = -1 \\ y_4 = x_3 - |y_3| + 1 = -1 \end{cases}$.

It means that $(x_4, y_4) = (-1, -1)$. We have the following lemma.

Lemma 1. *Let* $(x_0, y_0) \in A$ *be an initial condition where* $2x_0 + 2y_0 + 1 \leq 0$. *Then the fourth iteration of the solution of the system* (3) *is an equilibrium point* $(-1, -1)$.

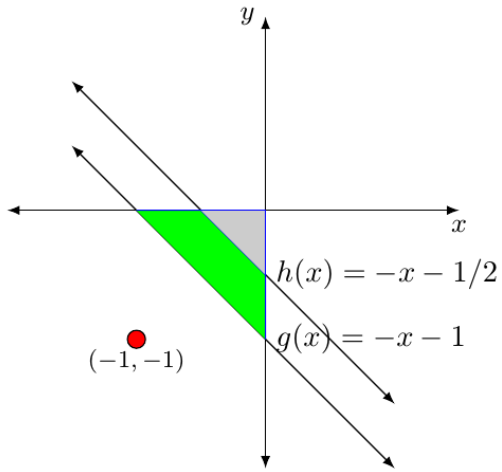

Figure 2 The region A is separated into two subregions.

We now suppose $(x_0, y_0) \in A$ to be an initial condition where $2x_0 + 2y_0 + 1 > 0$, which corresponds to the gray region in Figure 2. In Figure 2, The green region represents the points that satisfy the condition in Lemma 1, while the gray region is the remaining part of set A. We have the closed form of the solution in (4) – (6), except for $x_3 = 2x_0 + 2y_0 + 1 > 0$. Then

$$\begin{cases} x_4 = |x_3| - y_3 - 3 = 4x_0 + 4y_0 + 1 \\ y_4 = x_3 - |y_3| + 1 = -1 \end{cases}, \quad (7)$$

If $x_4 = 4x_0 + 4y_0 + 1 \leq 0$ then the next iteration

$$\begin{cases} x_5 = |x_4| - y_4 - 3 = -4x_0 - 4y_0 - 3 < 0 \\ y_5 = x_4 - |y_4| + 1 = 4x_0 + 4y_0 + 1 \leq 0 \end{cases},$$
$$\begin{cases} x_6 = |x_5| - y_5 - 3 = -1 \\ y_6 = x_5 - |y_5| + 1 = -1 \end{cases}.$$

This means that $(x_6, y_6) = (-1, -1)$. We have the following lemma.

Lemma 2. *Let* $(x_0, y_0) \in A$ *be an initial condition where* $4x_0 + 4y_0 + 1 \leq 0$. *Then the sixth iteration of the solution of the system* (3) *is an equilibrium point* $(-1, -1)$.

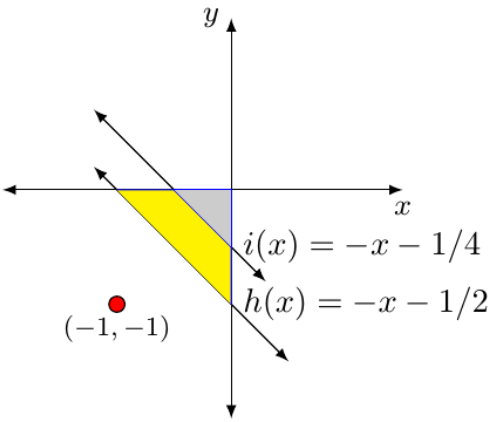

Figure 3 The gray region in Figure 2 is separated into two subregions.

We further suppose $(x_0, y_0) \in A$ to be an initial condition where $4x_0 + 4y_0 + 1 > 0$, which corresponds to the gray region in Figure 3. In Figure 3, The yellow region represents the points that satisfy the condition in Lemma 2, while the gray region is the remaining part of the set A.We will show that the solution will become an equilibrium point, proving by induction the following lemma.

Lemma 3. *Let* $(x_0, y_0) \in A$ *be an initial condition where* $4x_0 + 4y_0 + 1 > 0$. *Then, the solution of the system* (3) *is eventually the equilibrium point.*

Proof. We have the closed form of the solution in (4) – (7), except for $x_4 = 4x_0 + 4y_0 + 1 > 0$. Let $A_n = \{(x, y) \in Q_3 | 2^{2n}x + 2^{2n}y + 1 > 0\}$ and $P(n)$ be the following statement "for $(x_0, y_0) \in A_n$,

$$\begin{cases} x_{4n+1} = 2^{2n}x_0 + 2^{2n}y_0 - 1 < 0 \\ y_{4n+1} = 2^{2n}x_0 + 2^{2n}y_0 + 1 > 0 \end{cases},$$

$$\begin{cases} x_{4n+2} = -2^{2n+1}x_0 - 2^{2n+1}y_0 - 3 < 0 \\ y_{4n+2} = -1 \end{cases},$$

$$\begin{cases} x_{4n+3} = 2^{2n+1}x_0 + 2^{2n+1}y_0 + 1 \\ y_{4n+3} = -2^{2n+1}x_0 - 2^{2n+1}y_0 - 3 < 0 \end{cases}.$$

If $(x_0, y_0) \in B_n = \{(x, y) \in A_n | 2^{2n+1}x + 2^{2n+1}y + 1 \leq 0\}$

then $x_{4n+3} = 2^{2n+1}x_0 + 2^{2n+1}y_0 + 1 \leq 0$. Thus
$\begin{cases} x_{4n+4} = -1 \\ y_{4n+4} = -1 \end{cases}$.
If $(x_0, y_0) \in A_n - B_n =$
$\{(x, y) \in A_n | 2^{2n+1}x + 2^{2n+1}y + 1 > 0\}$
then $x_{4n+3} = 2^{2n+1}x_0 + 2^{2n+1}y_0 + 1 > 0$. So
$\begin{cases} x_{4n+4} = 2^{2n+2}x_0 + 2^{2n+2}y_0 + 1 \\ y_{4n+4} = -1 \end{cases}$,
If $(x_0, y_0) \in (A_n - B_n) - A_{n+1} =$

$$\{(x, y) \in A_n - B_n | 2^{2n+2}x + 2^{2n+2}y + 1 \leq 0\},$$

then $x_{4n+4} = 2^{2n+2}x_0 + 2^{2n+2}y_0 + 1 \leq 0$. So

$$\begin{cases} x_{4n+5} = -2^{2n+2}x_0 - 2^{2n+2}y_0 - 3 < 0 \\ y_{4n+5} = 2^{2n+2}x_0 + 2^{2n+2}y_0 + 1 \leq 0 \end{cases},$$

$$\begin{cases} x_{4n+6} = -1 \\ y_{4n+6} = -1 \end{cases}.$$

DOI: 10.60101/jarst.2024.258602

JOURNAL OF APPLIED RESEARCH ON SCIENCE AND TECHNOLOGY

If $(x_0, y_0) \in A_{n+1} =$

$$\{(x, y) \in Q_3 | 2^{2n+2}x + 2^{2n+2}y + 1 > 0\}$$

then $x_{4n+4} = 2^{2n+2}x_0 + 2^{2n+2}y_0 + 1 > 0.''$

We first show that $P(1)$ is true. Since $x_4 = 2^2x_0 + 2^2y_0 + 1 > 0$ and $y_4 = -1$ for $n = 1$ with $(x_0, y_0) \in A_1 = \{(x, y) \in Q_3 | 2^2x + 2^2y + 1 > 0\}$, we have

$$\begin{cases} x_{4(1)+1} = x_5 = 2^2x_0 + 2^2y_0 - 1 < 0 \\ y_{4(1)+1} = y_5 = 2^2x_0 + 2^2y_0 + 1 > 0 \end{cases}.$$

Since $(x_0, y_0) \in Q_3$, we have $x_0 < 0$ and $y_0 < 0$, thus $x_5 = 2^2x_0 + 2^2y_0 - 1 < 0$. Additionally, since $(x_0, y_0) \in A_1$, we have $y_5 = 2^2x_0 + 2^2y_0 + 1 > 0$. Then

$$\begin{cases} x_{4(1)+2} = x_6 = -2^3x_0 - 2^3y_0 - 3 < 0 \\ y_{4(1)+2} = y_6 = -1 \end{cases}.$$

Since $x_6 = -2y_5 - 1$, we have $x_6 < 0$.

$$\begin{cases} x_{4(1)+3} = x_7 = 2^3x_0 + 2^3y_0 + 1 \\ y_{4(1)+3} = y_7 = -2^3x_0 - 2^3y_0 - 3 < 0 \end{cases}.$$

Since $y_7 = x_6$, we have $y_7 < 0$.

If $(x_0, y_0) \in B_1 = \{(x, y) \in A_1 | 2^3x + 2^3y + 1 \leq 0\}$

then $x_7 = 2^3x_0 + 2^3y_0 + 1 \leq 0$.

Then $\begin{cases} x_{4(1)+4} = x_8 = -1 \\ y_{4(1)+4} = y_8 = -1 \end{cases}.$

If $(x_0, y_0) \in A_1 - B_1 =$
$\{(x, y) \in A_1 | 2^3x + 2^3y + 1 > 0\}$

then $x_7 = 2^3x_0 + 2^3y_0 + 1 > 0.$

$$\begin{cases} x_{4(1)+4} = x_8 = 2^4x_0 + 2^4y_0 + 1 \\ y_{4(1)+4} = y_8 = -1 \end{cases}.$$

If $(x_0, y_0) \in (A_1 - B_1) - A_2 =$
$\{(x, y) \in A_1 - B_1 | 2^4x + 2^4y + 1 \leq 0\}$

then $x_8 = 2^4x_0 + 2^4y_0 + 1 \leq 0.$

$$\begin{cases} x_{4(1)+5} = x_9 = -2^4x_0 - 2^4y_0 - 3 < 0 \\ y_{4(1)+5} = y_9 = 2^4x_0 + 2^4y_0 + 1 < 0 \end{cases},$$

$$\begin{cases} x_{4(1)+6} = x_{10} = -1 \\ y_{4(1)+6} = y_{10} = -1 \end{cases}.$$

If $(x_0, y_0) \in A_2 = \{(x, y) \in Q_3 | 2^4x + 2^4y + 1 > 0\}$ then $x_8 = 2^4x_0 + 2^4y_0 + 1 > 0$. Hence, $P(1)$ is true.

The base case of the induction, A_1 is the triangular region of the initial condition (x_0, y_0) that is bounded by the graph of the function $(x) = -x - 1/4$, the x-axis, and the y-axis, which corresponds to the blue dotted region in Figure 4. In Figure 4, the region of the initial condition A_1 for the base case of induction is indicated by the dotted blue line. The green region represents set B_1. The orange and white regions represent $A_1 - B_1$, and the white region represents A_2. B_1 is the region inside A_1 below the graph of $j(x) = -x - 1/8$, which is the green region in Figure 4. $A_1 - B_1$ is the triangular region above $j(x)$ and A_2 is the triangular region above $k(x)$ in Figure 4.

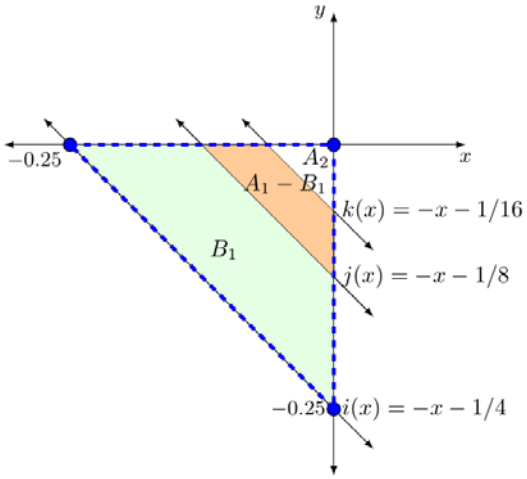

Figure 4 The region of the initial condition A_1 for the base case of induction.

Now we suppose further that $P(k)$ is true for a positive integer. We have

$x_{4k+4} = 2^{2k+2}x_0 + 2^{2k+2}y_0 + 1 > 0$ and $y_{4k+4} = -1$

for $(x_0, y_0) \in A_{k+1} =$

$$\{(x_0, y_0) \in Q_3 | 2^{2k+2}x_0 + 2^{2k+2}y_0 + 1 > 0\}.$$

Then

$$\begin{cases} x_{4(k+1)+1} = x_{4k+5} = 2^{2(k+1)}x_0 + 2^{2(k+1)}y_0 - 1 < 0 \\ y_{4(k+1)+1} = y_{4k+5} = 2^{2(k+1)}x_0 + 2^{2(k+1)}y_0 + 1 > 0 \end{cases}.$$

Since $(x_0, y_0) \in Q_3$, we have $x_0, y_0 < 0$, and thus

$x_{4(k+1)+1} = 2^{2(k+1)}x_0 + 2^{2(k+1)}y_0 - 1 < 0.$

Additionally, since $(x_0, y_0) \in A_{k+1}$, we have

$y_{4(k+1)+1} = 2^{2(k+1)}x_0 + 2^{2(k+1)}y_0 + 1 > 0$. Thus

$$\begin{cases} x_{4(k+1)+2} = x_{4k+6} = -2^{2(k+1)+1}x_0 - 2^{2(k+1)+1}y_0 - 3 < 0 \\ y_{4(k+1)+2} = y_{4k+6} = -1 \end{cases}.$$

Since $x_{4(k+1)+2} = -2y_{4(k+1)+1} - 1,$

we have $x_{4(k+1)+2} < 0.$

$$\begin{cases} x_{4(k+1)+3} = x_{4k+7} = 2^{2(k+1)+1}x_0 + 2^{2(k+1)+1}y_0 + 1 \\ y_{4(k+1)+3} = y_{4k+7} = -2^{2(k+1)+1}x_0 - 2^{2(k+1)+1}y_0 - 3 < 0 \end{cases}.$$

Since $y_{4(k+1)+3} = x_{4(k+1)+2}$, we have $y_{4(k+1)+3} < 0.$

If $(x_0, y_0) \in B_{k+1} =$
$\{(x, y) \in A_{k+1} | 2^{2k+3}x + 2^{2k+3}y + 1 \leq 0\}$

then $x_{4(k+1)+3} = 2^{2(k+1)+1}x_0 + 2^{2(k+1)+1}y_0 + 1 \leq 0.$

Thus $\begin{cases} x_{4(k+1)+4} = -1 \\ y_{4(k+1)+4} = -1 \end{cases}.$

If $(x_0, y_0) \in A_{k+1} - B_{k+1} =$

$$\{(x, y) \in A_{k+1} | 2^{2k+3}x + 2^{2k+3}y + 1 > 0\}$$

then $x_{4(k+1)+3} = 2^{2k+3}x_0 + 2^{2k+3}y_0 + 1 > 0.$ Thus

JOURNAL OF APPLIED RESEARCH ON SCIENCE AND TECHNOLOGY

$$\begin{cases} x_{4(k+1)+4} = x_{4k+8} = 2^{2(k+1)+2}x_0 + 2^{2(k+1)+2}y_0 + 1 \\ y_{4(k+1)+4} = y_{4k+8} = -1 \end{cases}.$$

If $(x_0, y_0) \in (A_{k+1} - B_{k+1}) - A_{k+2} =$

$\{(x, y) \in (x, y) \in A_{k+1} - B_{k+1} | 2^{2k+4}x + 2^{2k+4}y + 1 \leq 0\}$

Then $x_{4(k+1)+4} = x_{4k+8} = 2^{2k+4}x_0 + 2^{2k+4}y_0 + 1 \leq 0.$ Thus

$$\begin{cases} x_{4(k+1)+5} = x_{4k+9} = -2^{2(k+1)+2}x_0 - 2^{2(k+1)+2}y_0 - 3 < 0 \\ y_{4(k+1)+5} = y_{4k+9} = 2^{2(k+1)+2}x_0 + 2^{2(k+1)+2}y_0 + 1 \leq 0 \end{cases}.$$

Since $x_{4(k+1)+5} = -2x_{4(k+1)+3} - 1,$

we have $x_{4(k+1)+5} < 0$ and $y_{4(k+1)+5} = x_{4(k+1)+4} \leq 0.$

Thus $\begin{cases} x_{4(k+1)+6} = -1 \\ y_{4(k+1)+6} = -1 \end{cases}.$

If $(x_0, y_0) \in A_{k+2} =$
$\{(x, y) \in Q_3 | 2^{2k+4}x + 2^{2k+4}y + 1 > 0\}$ then

$x_{4k+8} = 2^{2k+4}x_0 + 2^{2k+4}y_0 + 1 > 0.$

Hence $P(k+1)$ is true. By mathematical induction, we conclude that $P(n)$ is true for every positive integer $n \geq 1$. If n increases, the regions of A_n and B_n will become progressively smaller. By mathematical induction, $P(n)$ shows that if the initial condition is within region A_1, the solution will eventually converge to an equilibrium point. □

By the above lemmas, we immediately have the following theorem.

Theorem *Let (x_0, y_0) be an initial condition in the set. Then the solution of the system (3) is eventually the equilibrium point.*

The second region, the set B, which corresponds to the pink region in Figure 1. We obtain the following solutions:

$$\begin{cases} x_1 = |x_0| - y_0 - 3 = -x_0 - y_0 - 3 < 0 \\ y_1 = x_0 - |y_0| + 1 = x_0 + y_0 + 1 < 0 \end{cases},$$

$$\begin{cases} x_2 = |x_1| - y_1 - 3 = -1 \\ y_2 = x_1 - |y_1| + 1 = -1 \end{cases}.$$

We have the following proposition.

Proposition *Let $(x_0, y_0) \in B$ be an initial condition where $2x_0 + 2y_0 + 1 \leq 0$. Then the second iteration of the solution of the system (3) is an equilibrium point $(-1, -1)$.*

The remaining region, which is below the line of the function $f(x) = -x - 3$, is in the set C of the third quadrant in Figure 1. We have (x_1, y_1) belonging to the fourth quadrant. The behaviors of the solution are more complicated than those of the other two sub-regions and are interesting to study, which we leave for future work. This result agrees with the findings in article [12]; there are regions where the solution eventually becomes an equilibrium point.

From the Theorem and Proposition, the solution will eventually converge to an equilibrium point when we begin with an initial condition in set A or B. These results expand the understanding of the behavior of system (3), building on [12], which examined initial conditions only in the first quadrant, and further findings of [13] and [14], which focused specifically on initial conditions in the second quadrant. However, according to our results, no initial condition will converge to a 4-cycle. We conjecture that the solution of system (3) with an initial condition in set C will eventually converge to a 4-cycle $P_{4.1}$ or $P_{4.2}$.

CONCLUSIONS

In conclusion, system (3) analysis reveals that its long-term behavior is highly sensitive to the initial conditions, particularly within different sub-regions of the third quadrant. For initial conditions in the set A, the system converges to the equilibrium point (-1, -1) after either four or six iterations, depending on the specific region of A. Similarly, for initial conditions in set B, the solution also converges to the equilibrium point in just two iterations. However, the behavior of the system for initial conditions in set C is notably more complex, with the possibility of convergence to a 4-cycle rather than an equilibrium point. This complexity presents fascinating opportunities for future research. Although our current findings suggest that no initial conditions in sets A or B lead to a 4-cycle, we conjecture that the system's behavior in set C may eventually result in convergence to one of the identified 4-cycles, $P_{4.1}$ or $P_{4.2}$, as highlighted in previous studies. Further investigation into this sub-region is necessary to fully understand the behaviors of system (3).

ACKNOWLEDGEMENT

The authors are supported by the National Research Council of Thailand and Pibulsongkram Rajabhat University.

REFERENCES

1. Cushing JM, Park J, Farrell A, Chitnis N. Treatment outcome in an SI model with evolutionary resistance: a Darwinian model for the evolution of resistance. J Biol Dyn. 2023;17(1).
2. Sushko I, Gardini L, Matsuyama K. 1D piecewise smooth map: Exploring a model of investment dynamics under financial frictions with three types of investment projects. Ukr Math J. 2024; 75(12):1900-17.
3. Zhusubaliyev Zh T, Mosekilde E. Torus birth bifurcation in a DC/DC converter. IEEE Trans Circuits Syst. 2006;53:1839-50.
4. Gardini L, Tikjha W. The Lorenz model in discrete time. J Differ Equ Appl. 2022;28(10):1308-33.
5. Gardini L, Radi D, Schmitt N, Sushko I, Westerhoff F. On boom-bust stock market dynamics, animal

DOI: 10.60101/jarst.2024.258602

spirits, and the destabilizing nature of temporarily attracting virtual fixed points. Macroecon Dyn. 2024;1-31.

6. Gardini L, Radi D, Schmitt N, Sushko I, Westerhoff F. A 2D piecewise-linear discontinuous map arising in stock market modeling: Two overlapping period-adding bifurcation structures. Chaos Solit. 2023; 176:114143.
7. Grove EA, Lapierre E, Tikjha W. On the global behavior of $x_{n+1} = |x_n| - y_n - 1$ and $y_{n+1} = x_n + |y_n|$. CUBO. 2012;14:125-66.
8. Tikjha W, Lenbury Y, Lapierre E. On the global character of the system of piecewise linear difference equations $x_{n+1} = |x_n| - y_n - 1$ and $y_{n+1} = x_n - |y_n|$. Adv Differ Equ. 2010;2010:573281.
9. Tikjha W, Lapierre E. Periodic solutions of a system of piecewise linear difference equations. Kyungpook Math J. 2020;60:401-413.
10. Aiewcharoen B, Boonklurb R, Konglawan N. Global and local behavior of the system of piecewise linear difference equations $x_{n+1} = |x_n| - y_n - b$ and $y_{n+1} = x_n - |y_n| + 1$ where $b \geq 4$. Mathematics. 2021;9 (1390):1-27.
11. Laoharenoo A, Boonklurb R, Rewlirdsirikul W. Complete analysis of global behavior of certain systems of piecewise linear difference equations. Aust J Math Anal Appl. 2023;20(1):1-33.
12. Tikjha W, Piasu K. A necessary condition for eventually equilibrium or periodic to a system of difference equations. J Comput Anal Appl. 2020;28(2):254-61.
13. Krisuk S, Soprom K, Pantain J, Tikjha W. Equilibrium solution on a two-dimensional piecewise linear map. KKU Sci J. 2023;50(3):223-30.
14. Youtuam K, Thipar B, Thakthuang N, Tikjha W. Stable attractors on a certain two-dimensional piecewise linear map. J Comput Anal Appl. 2024; 32(1):222-35.
15. Grove EA, Ladas G. Periodicities in Nonlinear Difference Equations. New York: Chapman and Hall/CRC; 2005.

DOI: 10.60101/jarst.2024.258602

Received: December 27, 2024 | Revised: February 10, 2025 | Accepted: February 13, 2025

JOURNAL OF APPLIED RESEARCH ON SCIENCE AND TECHNOLOGY
JARST
INSTITUTE OF RESEARCH AND DEVELOPMENT
RAJAMANGALA UNIVERSITY OF TECHNOLOGY THANYABURI
ISSN ONLINE: 2773-9473
https://ph01.tci-thaijo.org/index.php/rmutt-journal

Development and optimization of a fresh lotus embryo piercing machine

Sunan Parnsakhorn, Palapol Dangthongdee, Pongsathorn Sarika, Jaturong Langkapin and Prueksa Sawardsuk*
Department of Agricultural Engineering, Faculty of Engineering, Rajamangala University of Technology Thanyaburi, Khlong Luang, Pathum Thani 12110, THAILAND
*Corresponding author: prueksa_s@rmutt.ac.th

ABSTRACT

Crispy lotus seeds were a healthful snack suitable for all ages and commonly available in modern commerce outlets. The production process requires removing the lotus embryo before crisping. Traditionally, manual labor separated the embryo from the lotus seeds. Operators use specialized equipment to separate the lotus embryo from the lotus seeds. This requires a lot of work time and may cause injury to the operator due to the equipment used. Many research works have created machines to help process lotus seed products, but their performance is lacking. This research focused on creating and developing a fresh lotus seed embryo removal machine to improve precision and reduce seed damage during extraction. The prototype machine included a frame construction, a seed feeding tray, a piercing unit, and a PLC control panel. Two types of needles are used to pierce the lotus embryo. The sharp needle produced the best results when tested with sharp and blunt needles at piercing speeds of 16.7, 25.0, and 33.3 mm/s. The findings revealed a 91.7% success rate in embryo removal, 13.9% seed splitting, 2.8% seed damage, a processing capacity of 0.7 kg/hr, and an energy usage of 0.4 kW-hr. Economic engineering research revealed that employing the lotus embryo removal machine for 1,440 hours per year resulted in an average cost of 83.3 THB per kilogram, a 26.4-month payback period, and a breakeven threshold of 1,233.3 hours per year (863.3 kg per year). The prototype performed at least twice as quickly as manual labor (0.3 kg/hr).

Keywords: Lotus, Lotus seeds, Lotus embryos, Piercing machine

INTRODUCTION

The lotus plant is highly versatile, with all parts, from roots to leaves, being edible [1, 2]. Fresh lotus seeds, in particular, have been processed into OTOP products and developed into food items for modern trade markets. Lotus seeds are highly nutritious and possess therapeutic properties [3-5]. The bitter embryo at the seed's center resembles a sprout with two arrow-shaped leaves, one short and one long, ranging from yellow-green to dark green, measuring 1-1.5 cm in length and approximately 2 mm in diameter. Traditionally discarded, lotus seed embryos were later recognized for their medicinal properties, including alleviating irritability, insomnia, and oral infections, reducing blood pressure, dilating coronary arteries in arterial stenosis, and relieving thirst after hematemesis [6-8]. Consequently, their use increased, particularly in capsules and lotus seed tea.

In Thailand, community-based businesses process lotus seeds by peeling them with a fruit knife, manually removing the shell and membrane, and extracting the embryo with a toothpick or skewer (Figure 1). The seeds and embryos are then separated for further processing. This step relied on manual labor, posing a risk of cuts and requiring considerable time and effort [9]. Researchers in Thailand have investigated the use of lotus seed de-shelling and piercing machines [10-12]. Still, their lack of accuracy and performance, along with their high seed damage rate, have prevented their adoption. While lotus seed de-shelling machines used abroad [13-15] are available, their high cost and incompatibility with the physical characteristics of Thai lotus seeds have prevented imports. Lotus seed piercing machines have not been used either domestically or internationally. Therefore, research was conducted to develop a new industrial-grade lotus seed piercing machine, providing a model for entrepreneurs to study and improve the machine's accuracy and suitability for Thai-grown lotus seeds.

MATERIALS AND METHODS

2.1 Examined the key details for the design.

a) Studied the physical characteristics of lotus seeds.

This study aimed to determine the physical characteristics of peeled fresh lotus seeds, providing data for designing seed-feeding trays and making

DOI: 10.60101/jarst.2025.260222

JOURNAL OF APPLIED RESEARCH ON SCIENCE AND TECHNOLOGY

necessary machine adjustments, including seed diameter and length (Figure 2). A random sample of 100 lotus seeds was measured with a Mitutoyo 530-118 vernier caliper (made in Japan). The seed diameters ranged from 9 to 14 mm, averaging 11.2 ± 1.1 mm, and lengths ranged from 14 to 19 mm, averaging 16.7 ± 0.9 mm. Compared to Langkapin et al. (2014) [10], the seeds in this study were smaller and rounder. The diameter and length were used to design the width and height of the seed-feeding compartments in the packaging tray.

Figure 1 Manual method of peeling and piercing lotus seeds.

(a)Diameter (b) Length

Figure 2 Physical characteristics of lotus seeds.

b) Studied the optimal system for lotus seed piercing.

A literature survey revealed that Langkapin et al. (2014) [10] developed a fresh lotus seed piercing machine with a cam-controlled mechanism and a conveyor system powered by a Geneva wheel. The system achieved a 70% piercing rate, 13.3% seed damage, and a processing capacity of 1.2 kg/hr. The fully mechanical design resulted in high seed damage and low accuracy. To improve precision and reduce seed damage, key concepts from this machine were incorporated into a new design featuring a Programmable Logic Controller (PLC).

2.2 Design and construction of the prototype machine

Using the design data, a fresh lotus seed piercing machine was developed using computer-aided design software [16] and mechanical and agricultural machinery design concepts [17]. The main components included the main frame structure, the seed feeding tray, the piercing unit, and the PLC control panel, as shown in Figures 3 and 4.

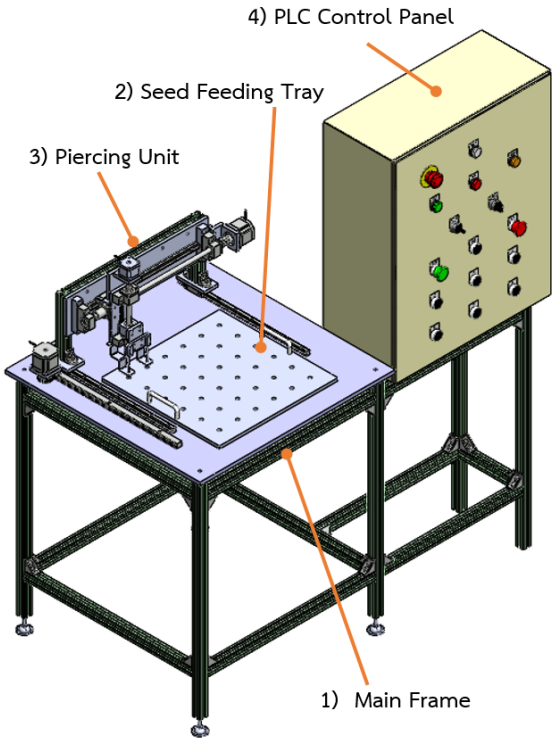

Figure 3 Prototype design using CAD software.

Figure 4 The prototype lotus seed piercing machine.

DOI: 10.60101/jarst.2025.260222

JOURNAL OF APPLIED RESEARCH ON SCIENCE AND TECHNOLOGY

The details of each component are as follows:

1. The main frame structure, made of 30 x 30 mm metal profiles, supports various components and is assembled with metal brackets, screws, and T-nuts. The frame measures 656 mm in width, 1,186 mm in length, and 800 mm in height. The seed tray and other components are positioned on top, with a 500 mm rack gear featuring 15 mm-wide teeth and 105 teeth and a 460 mm linear guide rail supporting the power system and drive components along the Y-axis. The PLC control panel is located on the right side of the frame.

2. The seed feeding tray, made of aluminum, holds peeled lotus seeds for piercing. It measures 425 mm in width, 425 mm in length, and 15 mm in height, with a handle for easy handling. The tray accommodates 36 seeds, arranged in 6 rows of 6 holes, spaced 65 mm apart. Each compartment is cylindrical, 14 mm in diameter, and 12 mm deep, with a bottom hole twice the size of the piercing needle, enabling it to pass through the tray.

3. Piercing unit: the piercing unit for the lotus seeds was mounted on a movable mechanism capable of movement along the X, Y, and Z axes. The coordinate system was defined using the right-hand rule. Design details are as follows:

The piercing unit's X and Y-axis moving device (Figure 5) features a Y-axis base that drives the piercing head along the X and Z axes. Using linear guides, the 10 mm thick aluminum base is fixed to the machine frame. A C-57STM03 stepping motor provides power, with a 15 mm wide, 25-tooth gear transmitting power to a rack gear on the Y-axis base, enabling 500 mm forward and backward movement of the piercing head. The X-axis movement is driven by another C-57STM03 motor, transferring power to a 500 mm ball screw, with a linear guide controlling its position for the left-right movement of the piercing head.

The Z-axis moving device, shown in Figure 6, enables vertical movement of the piercing head. It consists of a linear guide and a 180 mm ball screw mounted on a 12 mm thick aluminum base. A C-57STM03 stepping motor powers the system, allowing the piercing head to puncture two seeds simultaneously. The stainless-steel needle, 3 mm in diameter and 130 mm in length, is used for the puncturing process. As the piercing head rises, seeds are ejected from the needle by an aluminum push mechanism at the frame's bottom. The tests utilized two types of needles: blunt-ended and sharp-ended.

4. The PLC control panel, measuring 256 mm in width, 530 mm in length, and 750 mm in height, was mounted on the right side of the machine frame. It controlled the piercing machine's operation and featured an intuitive interface with status indicators and safety functions. The main control circuit used a Mitsubishi FX3U-32M PLC with 16 inputs and 16 outputs. The panel included relays, a switching power supply, circuit breakers, magnetic contactors, fuses, and terminal blocks. The front of the panel had a pilot bulb, push-button switches, various controls, and an emergency switch [18, 19].

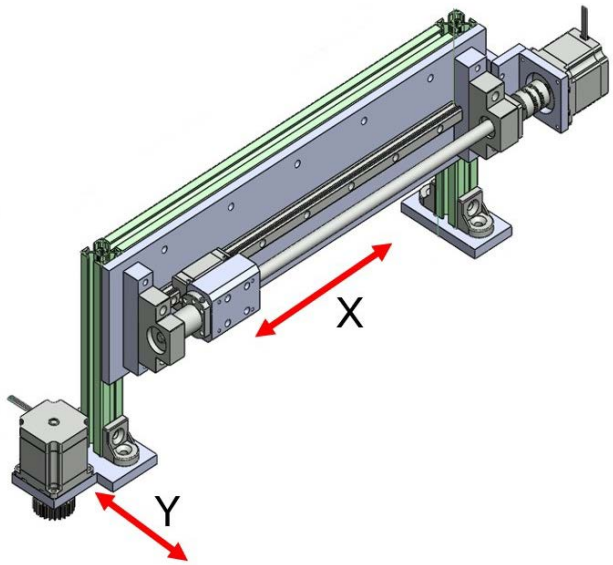

Figure 5 The X and Y axis moving device of the piercing unit.

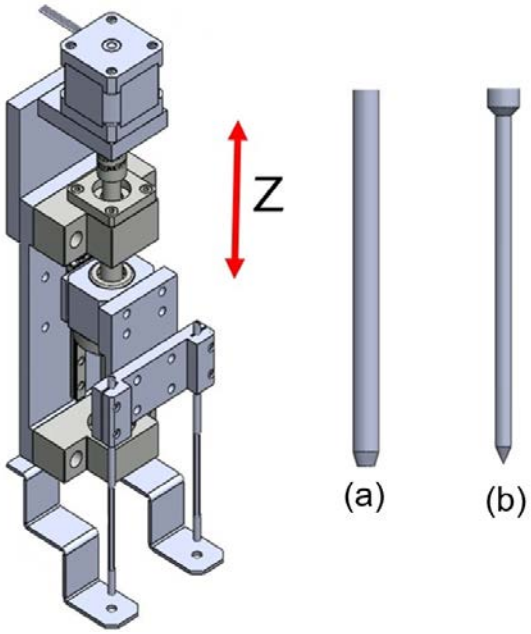

Figure 6 The Z-axis moving device and piercing needle: (a) blunt-tipped and (b) sharp-tipped.

The operation of the lotus seed-piercing machine commences with the operator placing the lotus seeds into the seeding tray and positioning the tray in the upper compartment of the machine. The white status light on the control panel is illuminated upon activating the circuit breaker and power switch. Pressing the Reset button once initiates the movement of the X, Z, and Y-axes through inductive proximity switches, enabling the detection and setting of the home position for all three axes. The switch is then set to "Auto" mode, and pressing the Start button activates

DOI: 10.60101/jarst.2025.260222

the green status light on the control panel. Subsequently, the piercing head moves to the designated position to pierce the seeds in the tray. Upon completion of the operation, the piercing head automatically returns to the home position, and the seed tray is removed to collect the pierced seeds.

2.3 Testing and performance evaluation of the prototype machine

After the prototype machine was modified to address defects, its performance was tested and evaluated, including the quality of lotus seed piercing. The study's performance indicators included piercing percentage, seed splitting percentage, seed damage percentage, operational capacity, and electrical energy consumption, calculated using the following equation:

The lotus seed piercing percentage was calculated using Equation (1).

$$c_t = \frac{W_1}{W} \times 100 \quad (1)$$

Where:
C_t = lotus seed piercing percentage (%)
W_1 = weight of pierced lotus seeds (kg)
W = total weight of lotus seeds (kg)

The percentage of lotus seeds split into two halves was calculated using Equation (2).

$$S_g = \frac{W_2}{W} \times 100 \quad (2)$$

Where:
S_g = percentage of lotus seeds split into two halves (%)
W_2 = weight of lotus seeds split into two halves (kg)

Damaged seeds were identified based on any visible cracks or defects from the original seed during testing. The percentage of seed damage was calculated using Equation (3).

$$D_g = \frac{W_3}{W} \times 100 \quad (3)$$

Where:
D_g = percentage of seed damage (%)
W_3= weight of damaged seeds (kg)

The operational efficiency was calculated using equation (4).

$$C_a = \frac{W_1}{T} \quad (4)$$

Where:
C_a = actual operational efficiency (kg/hr)
T = total operating time, Including the seed feeding time (hr).

Electrical energy consumption was calculated using equation (5).

$$P = \frac{IVt}{1{,}000} \quad (5)$$

Where:
P = the electrical energy consumption (kW-h)
I = the current (Amperes)
V = the voltage (Volts)
t = the time (Hours)

During the test, manually dehulled and size-sorted Padum variety lotus seeds were used, with diameters ranging from 9 to 14 mm (average 11.4 ± 1.2 mm) and lengths from 14 to 20 mm (average 17.1 ± 0.8 mm) based on a sample of 50 seeds. Initial tests identified an optimal pulse frequency for driving the stepper motors on all axes, ranging from 4,000 to 10,000 Hz, ensuring smooth operation. Test speeds for the stabbing head were selected based on motor-driven velocities of 16.7, 25.0, and 33.3 mm per second. Two types of needles, sharp-tipped and blunt-tipped, were used. Each test involved 30 seeds, with three replications per condition. For each trial, the total work time, weight of successfully punctured seeds, weight of seeds split into two halves, weight of damaged seeds, and voltage were recorded. Statistical analysis was conducted at a 95% confidence level using one-way ANOVA, followed by Duncan's New Multiple Range Test (DMRT) for multiple comparisons. A paired-samples t-test ($p < 0.05$) was used to assess significant differences between groups.

2.4 Economic analysis.

a) Analysis and evaluation of average costs.

The cost assessment for using the lotus seed punching machine assumed entrepreneurs purchased it to replace manual labor. It included both fixed and variable costs. Fixed costs comprised machine depreciation (calculated using the straight-line method over a 5-year lifespan) and the opportunity cost of capital (at a 10% interest rate). Fixed expenses that do not vary with processing volume, such as insurance, taxes, storage, and transportation, were excluded. Variable costs, determined by the amount of lotus seed processed, included labor, electricity, maintenance, and repair costs.

b) Payback Period Analysis.

This analysis estimated the time required for the investment in the lotus seed machine to be paid back, calculated by dividing the initial investment cost by the expected net benefits over 5 years.

c) Break-Even Point Analysis.

The break-even point was calculated by comparing the costs of using the prototype seed-peeling machine to those of manual labor [20].

RESULTS AND DISCUSSION

The lotus seeds obtained after testing the prototype machine's performance are shown in Figure 7(a). Figure 7(b) shows the peeled lotus seeds. Figure 7(c) depicts seeds with easily removable embryos, while Figure 7(d) shows seeds split into two halves and those damaged during testing. The test results of the prototype machine, based on the type of needle

DOI: 10.60101/jarst.2025.260222

and the average speed of the piercing head, are presented as follows.

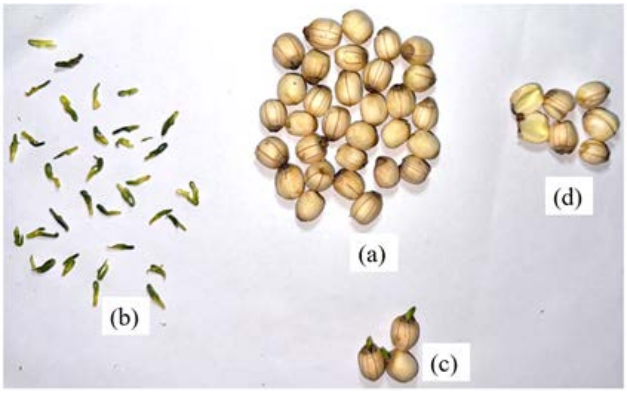

Figure 7 Performance test results of the lotus seed peeling machine: (a) lotus seeds after peeling, (b) peeled embryos, (c) partially peeled lotus seeds, and (d) lotus seeds split into two halves and damaged.

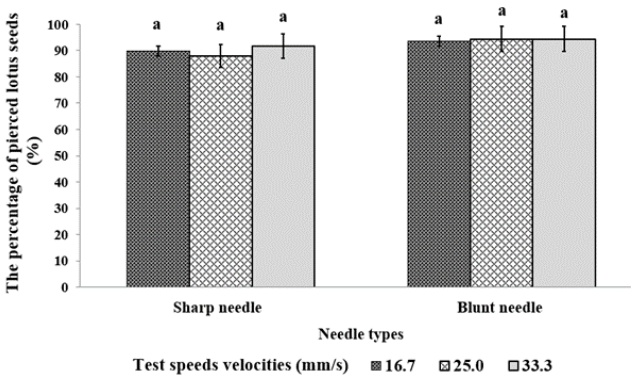

Figure 8 The percentage of lotus seed core removal at various needle types and average piercing speeds. (In each treatment, means followed by the same letter are not significantly different at $p \leq 0.05$ by Duncan's multiple range tests.)

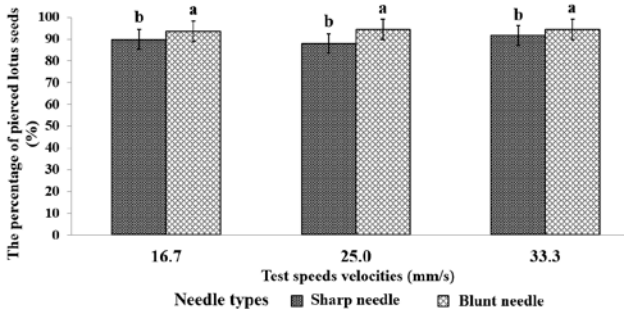

Figure 9 The percentage of lotus seed core removal at different piercing speeds and needle types. (In each treatment, means with the same letter are not significantly different at $p \leq 0.05$, as determined by pairwise t-tests.)

3.1 The percentage of pierced lotus seeds.

When tested with various needle types and average head speeds, the lotus seed piercing machine demonstrated a piercing rate of 88.0-94.4%. The statistical analysis showed no statistically significant differences in the piercing percentage at the 0.05 significance level between using sharp and blunt needles at various head speeds. As depicted in Figure 8, this finding suggests that either type of needle may be utilized at any head speed without affecting the piercing performance. According to the findings, the piercing percentage increased somewhat with more incredible head speeds and was comparable for both needles.

Figure 9 shows that the blunt needle performed better than the sharp needle at all tested speeds. The sharp needle achieved a piercing rate of 88.0-91.7%, while the blunt needle ranged from 93.5-94.4%, due to the blunt needle having a larger cross-sectional area in contact with the lotus embryo than the sharp needle. The optimal needle type and head speed should be selected based on additional research criteria, which will be discussed later.

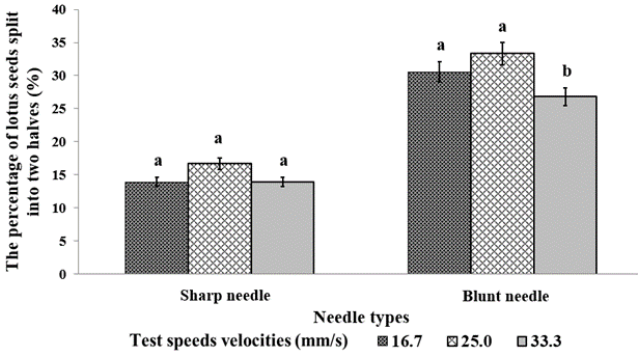

Figure 10 The percentage of lotus seeds split into two halves based on the type of needle and the piercing speed. (In each treatment, means followed by the same letter are not significantly different at $p \leq 0.05$ by Duncan's multiple range tests.)

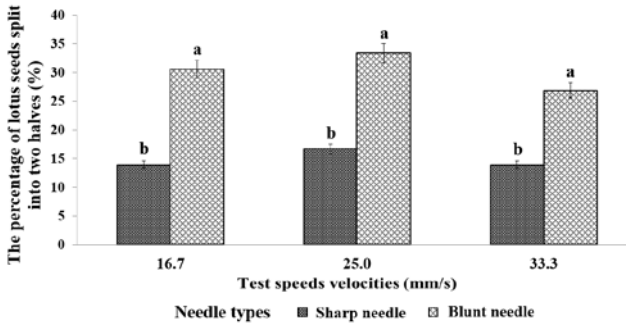

Figure 11 The percentage of lotus seeds split into two halves at different piercing speeds and needle types. (In each treatment, means with the same letter are not significantly different at $p \leq 0.05$, as determined by pairwise t-tests.)

3.2 The percentage of lotus seeds split into two halves.

Statistical analysis in Figure 10 showed no significant differences at the 0.05 level in the percentage of lotus seeds split into two halves when using the sharp needle across various head speeds. However, significant differences were found with the blunt

DOI: 10.60101/jarst.2025.260222

needle. The sharp needle split 13.9-16.7% of seeds, while the blunt needle split 26.9-30.6%. Figure 11 showed that the blunt needle consistently resulted in more seeds split across all speeds. As shown in Figure 12, both whole and split seeds can be processed into crispy lotus seeds, with no price difference reported.

(a) (b)

Figure 12 Shows dried lotus seeds: (a) split seeds [21] and (b) whole seeds [22].

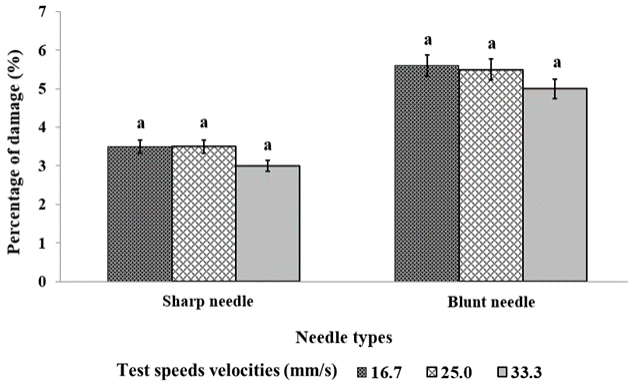

Figure 13 The percentage of damage at different types of needles and the piercing speed. (In each treatment, means followed by the same letter are not significantly different at $p \leq 0.05$ by Duncan's multiple range tests.)

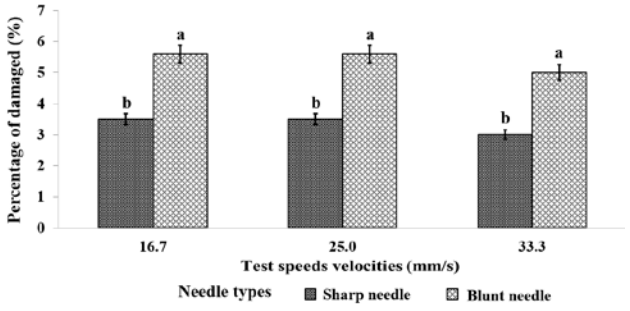

Figure 14 Damage percentage at different piercing speeds and needle types. (In each treatment, means with the same letter are not significantly different at $p \leq 0.05$, as determined by pairwise t-tests.)

3.3 Percentage of damage.

Figure 13 shows that both blunt and sharp needle head types yielded similar results. Damage percentage slightly decreased with increased puncture head speed, but statistical analysis found no significant differences at the 0.05 level. Damage percentage decreased with increasing puncture head speed. Figure 14 revealed that the blunt-tipped head caused more damage than the sharp-tipped head at all speeds. The blunt-tipped head had damage rates of 3.7-6.5%, while the sharp-tipped head ranged from 2.8-4.6%. The lowest damage percentage, 2.8%, occurred with the sharp-tipped head at a speed of 33.3 mm/s.

3.4 Machine performance.

Statistical analysis revealed significant differences in machine performance at a 0.05 significance level across tests with both puncture head types and speeds (Figure 15). Results shown in Figure 16 indicated no significant difference in piercing capability between the two head types at all average speeds. Performance improved with increased head speed, with operational capacities ranging from 0.4 to 0.7 kg/hr for both heads.

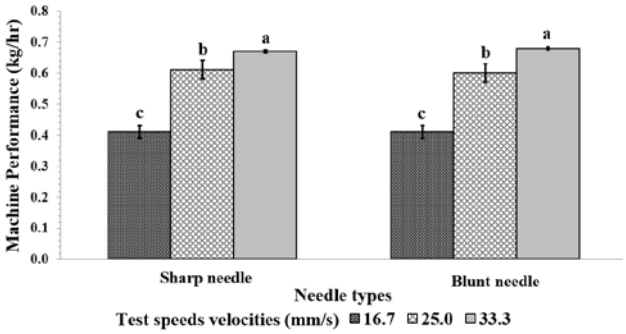

Figure 15 The work capacity of different types of needles and the piercing speed. (In each treatment, means followed by the same letter are not significantly different at $p \leq 0.05$ by Duncan's multiple range tests.)

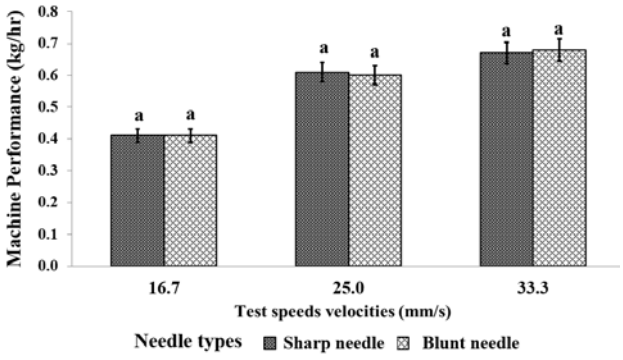

Figure 16 The work capacity at different piercing speeds and needle types. (In each treatment, means with the same letter are not significantly different at $p \leq 0.05$, as determined by pairwise t-tests.)

Based on operational capacity, piercing percentage, and seed damage, the sharp-tipped head at an average speed of 33.3 mm/s achieved the best performance, with a piercing efficiency of 91.7% and seed damage of only 2.8%. This configuration, with a

DOI: 10.60101/jarst.2025.260222

0.7 kg/hr capacity, was selected for further economic engineering analysis.

3.5 Power consumption.

Statistical analysis (Figure 17) showed significant differences in the machine's electrical energy consumption at a 0.05 significance level across probe types and speed groups. Energy usage increased with higher probe speeds, ranging from 0.2 to 0.4 kW-hr. At the optimal speed of 33.3 mm/s, the sharp probe, which demonstrated the highest work capacity, consumed 0.4 kW-hr. This value was used for subsequent economic engineering analysis.

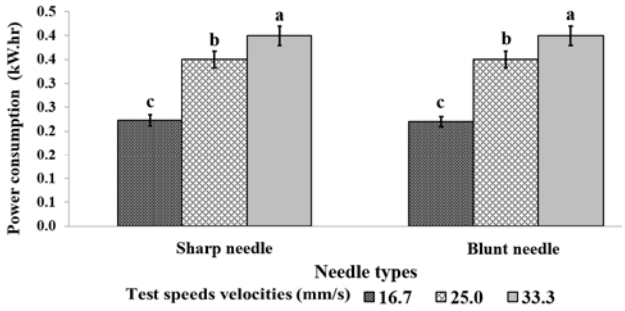

Figure 17 The electrical energy consumption at different types of needles and the piercing speed. (In each treatment, means followed by the same letter are not significantly different at $p \leq 0.05$ by Duncan's multiple range tests.)

3.6 Engineering economic analysis results.

The engineering economic analysis considered a single operator with a machine capacity of 0.7 kg/hr and energy consumption of 0.4 kW-hr, based on a prototype cost of 61,500 THB, a 5-year lifespan, and a 10% interest rate. The average price was 83.3 THB/kg, with a payback period of 26.4 months and a breakeven point at 1,233.3 hours/year (863.3 kg per year), assuming 1,440 hours of operation annually (8 hours/day for 6 months). These metrics were compared to manual labor by one worker.

CONCLUSIONS

Performance tests of the prototype lotus seed punching machine with a sharp-tipped head showed optimal operation at an average head speed of 33.3 mm/s, achieving a piercing rate of 91.7%, a production capacity of 0.7 kg/hr, a seed splitting rate of 13.9%, a seed damage rate of 2.8%, and an energy consumption of 0.4 kW-hr. Compared to Langkapin et al. (2014), the new machine had a 0.5 kg/hr lower work capacity, 10% less seed damage, and 21.7% greater accuracy. Despite this, it was more than twice as fast as manual labor. To enhance the processing speed significantly, the required production capacity can increase the number of tool headsets. The results met the study's objectives and offered operators a viable option for exploring an industry-level prototype.

ACKNOWLEDGEMENT

Financial support was provided by Rajamangala University of Technology Thanyaburi (RMUTT), Faculty of Engineering, Agricultural Engineering, Thanyaburi, Pathum Thani, Thailand.

REFERENCES

1. Guo H. Cultivation of lotus (Nelumbo nucifera Gaertn. ssp. nucifera) and its utilization in China. Genet Resour Crop Ev. 2009;56:323-30.
2. Lin Z, Zhang C, Cao D, Damaris RN, Yang P. The latest studies on lotus (Nelumbo nucifera)-an emerging horticultural model plant. Int J Mol Sci. 2019;20(15):3680.
3. Moro CF, Yonekura M, Kouzuma Y, Agrawal GK, Rakwal R. Lotus-a source of food and medicine: Current status and future perspectives in context of the seed proteomics. Int J Life Sci. 2013;7(1):1-5.
4. Zhang Y, Lu X, Zeng S, Huang X, Guo Z, Zheng Y, et al. Nutritional composition, physiological functions and processing of lotus (Nelumbo nucifera Gaertn.) seeds: A review. Phytochem Rev. 2015;14 (3):321-34.
5. Chen G, Zhu M, Guo M. Research advances in traditional and modern use of Nelumbo nucifera: Phytochemicals, health promoting activities and beyond. Crit Rev Food Sci Nutr. 2019;59(1):189-209.
6. Zhu MZ, Liu T, Zhang CY, Guo MQ. Flavonoids of lotus (Nelumbo nucifera) seed embryos and their antioxidant potential. J Food Sci. 2017;82: 1834-41.
7. Tungmunnithum D, Pinthong D, Hano C. Flavonoids from Nelumbo nucifera Gaertn., a Medicinal plant: Uses in traditional medicine, Phytochemistry and Pharmacological Activities. Medicines. 2018;5: 127.
8. Chen S, Li X, Wu J, Li J, Xiao M, Yang Y, et al. Plumula Nelumbinis: A review of traditional uses, phytochemistry, pharmacology, pharmacokinetics and safety. J Ethnopharmacol. 2021;266:113429.
9. Langkapin J, Parnsakhorn S, Kalsirisilp R, Samseemoung G, Ngmanil P, Juey T. Design and fabrication of a lotus seed membrane-peeling machine. J Eng RMUTT. 2019;1:127-37.
10. Langkapin J, Parnsakhorn S, Akarakulthon P. Design and development of a lotus seed embryo removing machine. Thai Soc Agric Eng J. 2014;20 (1):9-15.
11. Langkapin J, Parnsakhorn S, Kalsirisilp R, Prorod M, Khotpromsri N. Study and testing of a lotus seed peeling machine. J Eng RMUTT. 2018;1:35-42.

DOI: 10.60101/jarst.2025.260222

12. Langkapin J, Parnsakhorn S, Kalsirisilp R, Prorod M. Study and testing of a lotus seed peeling machine. SWU Eng J. 2021;16(1):82-92.

13. Zhu H, He J, Fang W, Ye D, Liang S. Design and test of small fresh lotus seed sheller. Trans Chin Soc Agric Eng. 2017;33(7):28-35.

14. Thưởng HT. Design and fabrication of cutting part for fresh lotus seed peeling machine. J Sci Technol. 2019;17(7):33-9.

15. Lin X, Zhu J, Huang P, Tian L, Chen B. Design and test of an automatic husking and peeling machine for fresh lotus seeds. Manuf Technol. 2022;22 (3):319-26.

16. James DB, Nathan B. Engineering Design and Graphics with SolidWorks® 2023. 1st ed. London: Pearson Education Inc.; 2023.

17. Richard GB, Keith NJ. Shigley's Mechanical engineering design. 10th ed. New York: McGraw-Hill Book Company; 2014.

18. Qiao D, Yang X, Jia J. The application of PLC to CNC machine tools development. In: Proceedings of the Second International Conference on Digital Manufacturing & Automation; Zhangjiajie, China; 2011. p. 1213-16.

19. Zhou Q. Application of PLC in the CNC machine tool control system. Adv Mater Manuf. 2012;182-183:902-5.

20. Hunt D. Farm Power Machinery Management. 10th ed. Ames, IA: Iowa State University Press; 2001.

21. Mae Jaroon Lotus Seeds Products. Split lotus Seeds [Internet]. 2023 [cited 2023 Jan 25]. Available from: https://www.facebook.com/Maejaroonlotusseed/photos_by?locale=th_TH.

22. Mai Lotus Seeds Products. Dried crispy lotus seed [Internet]. 2023 [cited 2023 Jan 25]. Available from: http://www.mailotusseeds.com/index.aspx?pid=eee02ef6-0f06-4998-8aa0-95d51388f5a1/.

DOI: 10.60101/jarst.2025.260222

Institute of Research and Development
Rajamangala University of Technology Thanyaburi

39 M.1 Klong 6, Thanyaburi, Pathumthani 12110, Thailand
Tel. (02) 549-4492 Fax. (02) 577-5038, (02) 549-4680

Website : https://ird.rmutt.ac.th